

AD _____

Award Number: DAMD17-02-1-0516

TITLE: Time-Resolved Spectral Optical Breast Tomography

PRINCIPAL INVESTIGATOR: Min Xu, Ph.D.

CONTRACTING ORGANIZATION: Research Foundation of the City
University of New York
New York, NY 10031

REPORT DATE: June 2005

TYPE OF REPORT: Annual Summary

PREPARED FOR: U.S. Army Medical Research and Materiel Command
Fort Detrick, Maryland 21702-5012

DISTRIBUTION STATEMENT: Approved for Public Release;
Distribution Unlimited

The views, opinions and/or findings contained in this report are those of the author(s) and should not be construed as an official Department of the Army position, policy or decision unless so designated by other documentation.

20051101 061

REPORT DOCUMENTATION PAGE

Form Approved
OMB No. 0704-0188

Public reporting burden for this collection of information is estimated to average 1 hour per response, including the time for reviewing instructions, searching existing data sources, gathering and maintaining the data needed, and completing and reviewing this collection of information. Send comments regarding this burden estimate or any other aspect of this collection of information, including suggestions for reducing this burden to Department of Defense, Washington Headquarters Services, Directorate for Information Operations and Reports (0704-0188), 1215 Jefferson Davis Highway, Suite 1204, Arlington, VA 22202-4302. Respondents should be aware that notwithstanding any other provision of law, no person shall be subject to any penalty for failing to comply with a collection of information if it does not display a currently valid OMB control number. PLEASE DO NOT RETURN YOUR FORM TO THE ABOVE ADDRESS.

1. REPORT DATE (DD-MM-YYYY) 01-06-2005		2. REPORT TYPE Annual Summary		3. DATES COVERED (From - To) 15 May 2002 - 15 May 2005	
4. TITLE AND SUBTITLE Time-Resolved Spectral Optical Breast Tomography				5a. CONTRACT NUMBER	
				5b. GRANT NUMBER DAMD17-02-1-0516	
				5c. PROGRAM ELEMENT NUMBER	
6. AUTHOR(S) Min Xu, Ph.D.				5d. PROJECT NUMBER	
				5e. TASK NUMBER	
				5f. WORK UNIT NUMBER	
7. PERFORMING ORGANIZATION NAME(S) AND ADDRESS(ES) Research Foundation of the City University of New York New York, NY 10031				8. PERFORMING ORGANIZATION REPORT NUMBER	
9. SPONSORING / MONITORING AGENCY NAME(S) AND ADDRESS(ES) U.S. Army Medical Research and Materiel Command Fort Detrick, Maryland 21702-5012				10. SPONSOR/MONITOR'S ACRONYM(S)	
				11. SPONSOR/MONITOR'S REPORT NUMBER(S)	
12. DISTRIBUTION / AVAILABILITY STATEMENT Approved for Public Release; Distribution Unlimited					
13. SUPPLEMENTARY NOTES					
14. ABSTRACT The research carried out during the three years' period involved: (a) extending the cumulant solution of radiative transfer to planar geometries and comparing with Monte Carlo simulations; (b) developing and enhancing the 3D tomographic image reconstruction algorithm by using the cumulant transport model and making use of a L-curve method guided by the signal-to-noise ratio; (c) deriving the nonlinear correction factor for optical imaging due to multiple passages of an absorption inhomogeneity by a photon and providing a measure of the efficacy of linear inversion schemes; (d) developing a novel image reconstruction algorithm "optical imaging using independent component analysis (OPTICA)"; and (e) testing and demonstrating the efficacy of OPTICA in imaging absorption, scattering, and/or fluorescence inhomogeneities in turbid media. The cumulant transport model was found to provide a more accurate model than the conventional diffusion model for image reconstruction in turbid media such as human breasts. The novel image reconstruction algorithm OPTICA has been shown effective in resolving low contrast small absorption, scattering, and/or fluorescence inhomogeneities in turbid media. The theoretical formalism and computer algorithm for 3D tomographic image reconstruction shows with experimental data the potential to provide fast 3D images of small tumors in breasts at early stage of development.					
15. SUBJECT TERMS Medical and biological imaging; Optical mammography; Time-resolve Imaging; Image reconstruction techniques; spectroscopic imaging					
16. SECURITY CLASSIFICATION OF:			17. LIMITATION OF ABSTRACT	18. NUMBER OF PAGES	19a. NAME OF RESPONSIBLE PERSON
a. REPORT U	b. ABSTRACT U	c. THIS PAGE U			19b. TELEPHONE NUMBER (include area code)
			UU	93	

Table of Contents

Cover.....	1
SF 298.....	2
Table of Content.....	3
Introduction.....	4
Body.....	4
Key Research Accomplishments.....	5
Reportable Outcomes.....	6
Conclusions.....	9
References.....	9
Appendices.....	11
Appendix 1: Analytical form of the particle distribution based on the cumulant solution of the elastic Boltzmann transport equation.....	
Appendix 2: Electric field Monte Carlo for polarized light propagation in turbid media..	
Appendix 3: Three-dimensional localization and optical imaging of objects in turbid media using independent component analysis.....	
Appendix 4: Optical imaging of turbid media using independent component analysis: Theory and simulation.....	
Appendix 5: Multiple passages of light through an absorption inhomogeneity in optical imaging of turbid media.....	
Appendix 6: <i>In Situ</i> determination of refractive index and size of Bacillus spores by light extinction.....	
Appendix 7: Fractal mechanisms of light scattering in biological tissue and cells.....	

Introduction

The “Time-resolved Spectral Optical Breast Tomography” research project aims to develop a near real-time three-dimensional (3D) spectral tomographic imaging algorithm with use of the cumulant approximation to radiative transfer to model light propagation in tissues. This project in the three years' period involves theoretical study of photon migration in turbid media, implementing an enhanced three-dimensional (3D) tomographic imaging algorithm, and performing image reconstruction for experimental data obtained from tissue phantoms and *ex vivo* tissues. The research generated 14 journal papers, 1 patent application, and 23 conference papers and presentations during this period.

Body

The tasks performed during the three years' period include theoretical study of photon migration in turbid media, implementing an enhanced 3D tomographic imaging algorithm, and performing image reconstructions for experimental data obtained from tissue phantoms and *ex vivo* tissues.

Theoretical study of photon migration in turbid media

We extended the photon transport model for light migration in turbid media based on a cumulant approximation to radiative transfer to a bounded medium with planar geometries[1] (Task 1.1). This extension makes the cumulant model more suitable in practical applications which always involve finite geometries. A “reshaped cumulant” solution[2, Appendix 1] is developed to improve upon the previous second order cumulant solution to radiative transfer[1] described by a Gaussian distribution in two aspects: 1) separating the ballistic component from the scattered component to ensure that the summation in expressions is convergent; and 2) enforcing the causality condition to ensure that no light travels faster than the speed of light. Time-resolved profiles obtained using the analytical form were compared with those obtained by the Monte Carlo simulation, for both transmission and backscattering. A significant improvement of the accuracy of the “reshaped cumulant” solution over the original cumulant solution is observed. The calculating time using our analytical form is much faster than that using the Monte Carlo approach, usually at least 10^4 times faster (Task 1.1).

We also developed a novel Monte Carlo algorithm (EMC) [3, Appendix 2] to simulate polarized light propagation in tissues and other turbid media (Task 1.1). This Monte Carlo method is based on tracing the multiply scattered electric field instead of the conventional Stokes vector. The unique feature of EMC makes it possible to simulate also coherent properties of multiply scattered light. The algorithm of EMC is straightforward and can be easily adapted to simulate the propagation of polarized light in optically active or gain medium.

Implementing an enhanced 3D tomographic imaging algorithm

We enhanced the 3D tomographic image reconstruction algorithms[4, 5] by using the new cumulant transport model (Task 1.2) and making use of spectral information when observations of multiple wavelengths are available (Task 1.3). We improved the 3D tomographic image reconstruction algorithm to use a L-curve method guided by the signal-to-noise ratio of the dataset to determine the regularization parameter (Task 1.4).

By scanning a point source on the grids of the input plane of a slab and measuring light intensities on a detector array on the exit plane of the slab, a set of four-dimensional (4D) data is formed. The spectral information adds an additional dimension of the data. The optimal approach to analyze this huge dataset is studied (Task 1.5). A novel optical imaging approach based on independent component analysis to analyze such massive dataset is proposed and implemented[6-9; Appendix 3, Appendix 4].

The image reconstruction algorithm is a new approach for optical imaging and localization of objects in turbid media that makes use of the independent component analysis (ICA) from information theory. Experimental arrangement realizes a multisource illumination of a turbid medium with embedded objects and a multidetector acquisition of transmitted light on the medium boundary. The resulting spatial diversity and multiple angular observations provide robust data for three-dimensional localization and characterization of inhomogeneities embedded in a turbid medium. ICA of the perturbations in the spatial intensity distribution on the medium boundary sorts out the embedded objects, and their locations are obtained from Green's function analysis based on any appropriate light propagation model.

We worked with the experimental group at the Institute of Ultrafast Lasers and Spectroscopy and to test and verify our image reconstruction algorithm (Task 1.5, Task 2.1, Task 2.2). We have successfully enhanced the algorithm to import data from the experimental group, to locate and characterize inhomogeneities within the turbid medium, and to generate the two dimensional (2D) cross sections of the inhomogeneities. The algorithm is tested and verified to work well for absorption, scattering, and/or fluorescence inhomogeneities embedded in phantoms using different wavelengths (Task 2.1, Task 2.2).

To access the efficacy of a linear inversion scheme in image reconstruction of human breasts, we also studied the nonlinear effect of the multiple passages of an absorption inhomogeneity of finite size deep inside a turbid medium on optical imaging using the cumulant solution to radiative transfer (Task 1). We derived the analytical nonlinear correction factor which agrees excellently with the predictions from the Monte Carlo simulations. We concluded that the effect of the nonlinear multiple passages of an absorption site on optical imaging only becomes appreciable when the size of the inhomogeneity reaches 10 times transport mean free path or larger for human tissues[10,11].

Image reconstructions for experimental data

We have successfully performed image reconstructions for experimental data obtained from tissue phantoms and *ex vivo* tissues with absorption, scattering, and/or fluorescence inhomogeneities embedded (Task 1.5, Task 2.1, Task 2.2, Task 2.3). To optimize the algorithm to achieve an *in vivo* mammography, we have studied the performance of the reconstruction algorithm on breast phantoms and *ex vivo* breast tissues (Task 1.5, Task 2.3). A total of about 10 cases for absorption, scattering, or fluorescence inhomogeneities embedded in phantoms were investigated. In each case, the inhomogeneities were correctly located and characterized. A two-dimensional (2D) cross section map of the inhomogeneities was then generated afterwards based on back-projection [6-9, Appendix 3, Appendix 4]. One notable case is for a breast phantom borrowed from University College London which has a thickness of 55mm (60 transport mean free path), comparable to a real breast. All the four inhomogeneities were correctly reconstructed [6, Appendix 3], including the one of the lowest contrast which has only 10% higher scattering than the background and was believed to be undetectable [12].

Our experimental results show that the image reconstruction algorithm is superior to conventional photon migration reconstruction algorithms in resolving low contrast and small inhomogeneities [6-9]. In addition, this approach is applicable to different medium geometries, can be used with any suitable photon propagation model, and is amenable to near-real-time imaging applications. This approach may be very useful in detecting small tumors in breasts at early stage of development.

Key Research Accomplishments

- Extended cumulant solution of radiative transfer to planar geometries making it more suitable for practical applications which involve finite boundaries.
- Developed a “reshaped cumulant” solution for photon migration in tissues and other turbid media, improving upon the previous cumulant solution to radiative transfer.

- Developed an Electric field Monte Carlo (EMC) algorithm for simulating polarized light propagation in turbid media whose unique feature includes simulating coherence phenomenon of multiply scattered light.
- Developed and enhanced the 3D tomographic image reconstruction algorithm by using the cumulant transport model.
- Developed the criterion of the optimal regulation parameter for inverse image reconstruction related to the noise presented in measurements and enhanced the 3D tomographic image reconstruction algorithm to use a L-curve method guided by the signal-to-noise ratio of the dataset to determine the regularization parameter.
- Derived the nonlinear correction factor of multiple passages of an absorption inhomogeneity by a photon for optical imaging and provided a measure of the efficacy of linear inversion schemes and extended the range of applicability of the linear inversion scheme for optical imaging.
- Developed a novel 3D image reconstruction algorithm “optical imaging using independent component analysis (OPTICA)”.
- Tested and demonstrated the efficacy of OPTICA in imaging absorption, scattering, and/or fluorescence inhomogeneities in turbid media, in particular, for low contrast small inhomogeneities.

Reportable Outcomes

Journal Papers:

1. M. Xu and R. R. Alfano. *Fractal mechanisms of light scattering in biological tissue and cells*. Opt. Lett., 2005. (accepted).
2. M. Xu, M. Alrubaiee, S. K. Gayen, and R. R. Alfano. *Three-dimensional localization and optical imaging of objects in turbid media using independent component analysis*. Appl. Opt., 44:18891897, 2005.
3. M. Xu, M. Alrubaiee, S. K. Gayen, and R. R. Alfano. *Optical imaging of turbid media using independent component analysis: Theory and simulation*. J. Biomed. Opt., 2005. (in press).
4. A. Katz, Alexandra Alimova, M. Xu, Paul Gottlieb, Elizabeth Rudolph, J. C. Steiner, and R. R. Alfano. *In Situ determination of refractive index and size of Bacillus spores by light extinction*. Opt. Lett., 30:589591, 2005.
5. W. Cai, M. Xu, and R. R. Alfano. *Analytical form of the particle distribution based on the cumulant solution of the elastic Boltzmann transport equation*. Phys. Rev. E, 71:041202, 2005. (10 pages).
6. M. Xu. *Electric field Monte Carlo for polarized light propagation in turbid media*. Opt. Exp., 12:65306539, 2004. <http://www.opticsexpress.org/abstract.cfm?URI=OPEX-12-26-653>.
7. M. Xu, W. Cai, and R. R. Alfano. *Multiple passages of light through an absorption inhomogeneity in optical imaging of turbid media*. Opt. Lett., 29:17571759, 2004.
8. M. Xu. *Light extinction and absorption by arbitrarily oriented finite circular cylinders using geometrical path statistics of rays*. App. Opt., 42:67106723, 2003.
9. M. Xu, M. Lax, and R. R. Alfano. *Light anomalous diffraction using geometrical path statistics of rays and gaussian ray approximation*. Opt. Lett., 28:179181, 2003.
10. M. Xu and R. R. Alfano. *More on patterns in Mie scattering*. Opt. Comm., 226(1-6):15, 2003.
11. A. Katz, A. Alimova, M. Xu, E. Rudolph, M. Shah, H. Savage, R. Rosen, S. A. McCormick, and R. R. Alfano. *Bacteria size determination by elastic light scattering*. IEEE JSTQE, 9:277287, 2003.

12. W. Cai, M. Xu, and R. R. Alfano. *Three dimensional radiative transfer tomography for turbid media*. IEEE JSTQE, 9:189198, 2003.
13. M. Xu, W. Cai, M. Lax, and R. R. Alfano. *Photon migration in turbid media using a cumulant approximation to radiative transfer*. Phys. Rev. E, 65:066609, 2002.
14. W. Cai, M. Xu, M. Lax, and R. R. Alfano. *Diffusion coefficient depends on time not on absorption*. Opt. Lett., 27(9):731733, 2002.

Patents

15. R. R. Alfano, M. Xu, M. Alrubaiee, and S. K. Gayen. Optical tomography using independent component analysis for detection and localization of targets in turbid media. US Patent Application. (submitted).

Proceeding Papers:

16. M. Xu, M. Alrubaiee, S. K. Gayen, and R. R. Alfano. *Optical tomography using independent component analysis to detect absorptive, scattering, or fluorescent inhomogeneities in turbid media*. In Optical Tomography and Spectroscopy of Tissue VII, volume 5693 of Proceedings of SPIE, Jan. 22-27, San Jose, California, USA, 2005. (in press).
17. M. Xu and R. R. Alfano. *Light depolarization in turbid media*. In Optical Tomography and Spectroscopy of Tissue VII, volume 5693 of Proceedings of SPIE, Jan. 22-27, San Jose, California, USA, 2005. (in press).
18. A. Katz, A. Alimova, M. Xu, E. Rudolph, P. Gottlieb, J. C. Steiner, and R. R. Alfano. *Refractive index changes during germination of bacillus subtilis spores*. In Advanced Biomedical and Clinical Diagnostic Systems III, volume 5692 of Proceedings of SPIE, Jan. 23-26, San Jose, California, USA, 2005. (in press).
19. W. Cai, M. Al-Rubaiee, S. K. Gayen, M. Xu, and R. R. Alfano. *Three-dimensional optical tomography of objects in turbid media using the round-trip matrix*. In Optical Tomography and Spectroscopy of Tissue VII, volume 5693 of Proceedings of SPIE, Jan. 22-27, San Jose, California, USA, 2005. (in press).
20. M. Alrubaiee, M. Xu, S. K. Gayen, and R. R. Alfano. *Fluorescence optical tomography using independent component analysis to detect small targets in turbid media*. In Optical Tomography and Spectroscopy of Tissue VII, volume 5693 of Proceedings of SPIE, Jan. 22-27, San Jose, California, USA, 2005. (in press).
21. M. Al-rubaiee, M. Xu, S. K. Gayen W. Cai and, and R. R. Alfano. *Time-resolved and quasi-continuous wave three-dimensional tomographic imaging*. In Femtosecond Laser Applications in Biology, volume 5463 of Proceedings of SPIE, pages 8285, Palais de la Musique et des Congrès de Strasbourg, Strasbourg, France, Apr 2004. SPIE.
22. M. Xu, W. Cai, and R. R. Alfano. *Nonlinear multiple passage effects on optical imaging of an absorption inhomogeneity in turbid media*. In Photon Migration and Diffuse-light Imaging, volume 5138 of Proceedings of SPIE, pages 221230, 2003.
23. Alvin Katz, Alexandra Alimova, Min Xu, Elizabeth Rudolph, Howard E. Savage, Mahendra Shah, Steven A. McCormick, Richard B. Rosen, and Robert R. Alfano. *Identification of bacteria by light scattering*. In Alexander V. Priezzhev and Gerard L. Cote, editors, Optical Diagnostics and Sensing in Biomedicine III, volume 4965 of Proc. SPIE, pages 7376, 2003.

Presentations:

24. Mohammad Alrubaiee, Min Xu, Swapan K. Gayen, and Robert R. Alfano. *Optical tomography using independent component analysis for breast cancer detection*. In Era of Hope: Department of Defense Breast Cancer Research Program Meeting, Pennsylvania Convention Center, Philadelphia, June 8-11 2005. DOD.
25. Min Xu, Mohammad Alrubaiee, Wei Cai, Swapan K. Gayen, and Robert R. Alfano. *Toward optical imaging of small tumors in breasts using cumulant forward model and independent*

- component analysis*. In Era of Hope: Department of Defense Breast Cancer Research Program Meeting, Pennsylvania Convention Center, Philadelphia, June 8-11 2005. DOD.
26. Min Xu, Mohammad Alrubaiee, Swapan K. Gayen, and Robert R. Alfano. *Fluorescence optical imaging in turbid media using independent component analysis*. In CLEO/QELS and PhAST, Baltimore Convention Center, Baltimore, Maryland, May 22-27 2005. OSA.
 27. Min Xu and Robert R. Alfano. *Light depolarization by Mie scatterers*. In CLEO/QELS and PhAST, Baltimore Convention Center, Baltimore, Maryland, May 22-27 2005. OSA.
 28. Alvin Katz, Alexandra Alimova, Min Xu, Paul Gottlieb, Elizabeth Rudolph, Jeff C. Steiner, and R. R. Alfano. *Changes in refractive index and size of Bacillus Subtilis during activation, measured by light transmission*. In CLEO/QELS and PhAST, Baltimore Convention Center, Baltimore, Maryland, May 22-27 2005. OSA.
 29. Wei Cai, Min Xu, and Robert R. Alfano. *Light distribution from the analytical solution of the radiative transfer equation*. In CLEO/QELS and PhAST, Baltimore Convention Center, Baltimore, Maryland, May 22-27 2005. OSA.
 30. M. Alrubaiee, M. Xu, S. K. Gayen, and R. R. Alfano. *Three-dimensional localization of several scattering targets in a turbid media using independent component analysis*. In CLEO/QELS and PhAST, Baltimore Convention Center, Baltimore, Maryland, May 22-27 2005. OSA.
 31. K. G. Phillips, M. Xu, S. K. Gayen, and R. R. Alfano. *Backscattering of circularly polarized light from a forward-peaked scattering medium: an electric field Monte Carlo study*. In Einsteins in the city: a student research conference at the city college of new york, The City College of New York, new york city, NY 10031, Apr. 11-12 2005.
 32. M. Xu, M. Al-rubaiee, S. K. Gayen, and R. R. Alfano. *Information theory approach to detect small inhomogeneities within tissue-like turbid media*. In 4th Inter-institute Workshop on Optical Diagnostic Imaging from Bench to Bedside at the National Institutes of Health, National Institutes of Health, Natcher Conference Center, Bethesda, MD 20892, Sept. 20-22 2004.
 33. M. Al-rubaiee, M. Xu, S. K. Gayen, and R. R. Alfano. *Three-dimensional localization and reconstruction of objects in a turbid medium using independent component analysis of optical transmission and fluorescence measurements*. In 4th Inter-institute Workshop on Optical Diagnostic Imaging from Bench to Bedside at the National Institutes of Health, National Institutes of Health, Natcher Conference Center, Bethesda, MD 20892, Sept. 20-22 2004.
 34. M. Xu, M. Al-Rubaiee, W. Cai, S. K. Gayen, and R. R. Alfano. *Simulated and experimental separation and characterization of absorptive inhomogeneities embedded in turbid media*. In Biomedical Topical Meetings on CD-ROM (OSA), page WF25, Fontainebleau Hilton Resort and Towers, Miami Beach, Florida, Apr 2004.
 35. A. Katz, A. Alimova, M. Xu, P. Gottlieb, and R. R. Alfano. *Rapid optical detection of bio-agents*. In International Conference on Advanced Technologies for Homeland Security, Univ. Conn. Storrs, CT., Sept 25-26 2003.
 36. M. Xu, W. Cai, and R. R. Alfano. *Three dimensional Hybrid-Dual-Fourier tomography in turbid media using multiple sources and multiple detectors*. In Third Inter-Institute Workshops on Diagnostic Optical Imaging and Spectroscopy: The Clinical Adventure, National Institute of Health, Bethesda, MD, Sep. 26-27 2002.
 37. W. Cai, S. K. Gayen, M. Xu, and R. R. Alfano. *Improving inverse reconstruction problem for three-dimensional optical image of breast*. In Era of Hope-Department of Defense Breast Cancer Research Program Meeting, volume III, pages P481, Orange County Convention Center, Orlando, Florida, Sept. 25-28 2002.
 38. M. Al-Rubaiee, S. K. Gayen, W. Cai, M. Xu, J. A. Koutcher, and R. R. Alfano. *Near-infrared photonic imaging of human breast tissues*. In Era of Hope-Department of Defense

Grant application:

Applied for breast cancer concept award "Multispectral Optical Imaging Using Independent Component Analysis for Breast Cancer Detection" for BC03-CA.

Conclusions

The work carried out during the three years' period leads to the following conclusions. *First*, the cumulant transport model provides a more accurate model than the conventional diffusion model for the description of light propagation in turbid media such as human breasts. *Second*, the "reshaped cumulant" solution improves over the previous cumulant solution, providing a even more accurate model for light propagation in turbid media. *Third*, the optimal regularization of image reconstruction depends on the noise presented in the measurements; proper modeling of the noise and appropriate regularization improves the quality of image reconstruction. *Fourth*, the correction for the nonlinear effect of the multiple passages of an absorption site by light was shown to be essential in optical imaging to characterize properly inhomogeneities strong in absorption. *Fifth*, a novel image reconstruction algorithm "optical imaging using independent component analysis (OPTICA)" has been developed, able to resolve low contrast small absorption, scattering, and/or fluorescence inhomogeneities in turbid media. *Sixth*, the theoretical formalism and computer algorithm for 3D tomographic image reconstruction shows with experimental data the potential to provide fast 3D images of small tumors in breasts at early stage of development.

References

1. Xu, M., et al., *Photon migration in turbid media using a cumulant approximation to radiative transfer*. Phys. Rev. E, 65:066609, 2002.
2. W. Cai, M. Xu, and R. R. Alfano. *Analytical form of the particle distribution based on the cumulant solution of the elastic Boltzmann transport equation*. Phys. Rev. E, 71:041202, 2005. (10 pages).
3. M. Xu. *Electric field Monte Carlo for polarized light propagation in turbid media*. Opt. Exp., 12:65306539, 2004. <http://www.opticsexpress.org/abstract.cfm?URI=OPEX-12-26-653>.
4. Xu, M., et al., *Time sliced three dimensional inverse image reconstruction of objects in highly scattering media*, in *Optical tomography and spectroscopy of tissue III*. 1999. p. 2-4.
5. Xu, M., M. Lax, and R.R. Alfano, *Time-resolved Fourier optical diffuse tomography*. J. Opt. Soc. Am. A, 2001. **18**(7): p. 1535-1542.
6. M. Xu, M. Alrubaiee, S. K. Gayen, and R. R. Alfano. *Three-dimensional localization and optical imaging of objects in turbid media using independent component analysis*. Appl. Opt., 44:18891897, 2005.
7. M. Xu, M. Alrubaiee, S. K. Gayen, and R. R. Alfano. *Optical imaging of turbid media using independent component analysis: Theory and simulation*. J. Biomed. Opt., 2005. (in press).
8. M. Xu, M. Alrubaiee, S. K. Gayen, and R. R. Alfano. *Optical tomography using independent component analysis to detect absorptive, scattering, or fluorescent inhomogeneities in turbid media*. In *Optical Tomography and Spectroscopy of Tissue VII*, volume 5693 of Proceedings of SPIE, Jan. 22-27, San Jose, California, USA, 2005. (in press).
9. M. Alrubaiee, M. Xu, S. K. Gayen, and R. R. Alfano. *Fluorescence optical tomography using independent component analysis to detect small targets in turbid media*. In *Optical Tomography and Spectroscopy of Tissue VII*, volume 5693 of Proceedings of SPIE, Jan. 22-27, San Jose, California, USA, 2005. (in press).

10. Xu, M., W. Cai, and R.R. Alfano, *Multiple passages of light through an absorption inhomogeneity in optical imaging of turbid media*. Opt. Lett., 2004.
11. Xu, M., W. Cai, and R.R. Alfano. *Nonlinear multiple passage effects on optical imaging of an absorption inhomogeneity in turbid media*. in *European Conference on Biomedical Optics: Photon migration and Diffuse-light imaging*. 2003.
12. D. Hall, J. C. Hebden and D. T. Delpy. *Imaging very-low-contrast objects in breastlike scattering media with a time-resolved method*. Appl. Opt., 36:7270-7276, 1997.

Analytical form of the particle distribution based on the cumulant solution of the elastic Boltzmann transport equation

W. Cai, M. Xu, and R. R. Alfano

Institute for Ultrafast Spectroscopy and Lasers, New York State Center of Advanced Technology for Ultrafast Photonic Materials and Applications, Department of Physics, The City College and Graduate Center of City University of New York, New York, New York 10031, USA

(Received 17 November 2004; revised manuscript received 2 February 2005; published 5 April 2005)

An analytical expression of the particle distribution based on an analytical cumulant solution of the time-dependent elastic Boltzmann transport equation (BTE) is presented. This expression improves upon the previous second order cumulant solution of the BTE described by a Gaussian distribution in two aspects: (1) separating the ballistic component from the scattered component to ensure that the summation in expressions is convergent; and (2) enforcing the causality condition to ensure that no particle travels faster than the free speed of the particles. Time-resolved profiles obtained using the analytical form are compared with those obtained by the Monte Carlo simulation, for both transmission and backscattering. The calculating time using our analytical form is much faster than that using the Monte Carlo approach.

DOI: 10.1103/PhysRevE.71.041202

PACS number(s): 42.25.Dd, 05.60.Cd, 05.20.-y, 42.25.Fx

I. INTRODUCTION

The time-dependent elastic Boltzmann transport equation (BTE) describes the particle (and light, acoustic wave, etc.) propagation with time in a scattering medium, where the particles suffer multiple scattering by randomly distributed scatterers. The BTE is also called the radiative transfer equation in light propagation [1–3]. The solutions of the elastic BTE are applied in broad areas, such as atmospheric science, medical imaging, and solid state physics.

An example is the approach to optical imaging of human tissue that is often called “diffusion tomography,” because the theoretical model is built based on the solution of the diffusion equation. The diffusion equation is the lowest order approximation of the radiative transfer equation, which has significant error when the distance between a voxel and a source is short. However, the contribution from these voxels near the source to the measured signals is much larger than that from voxels deep inside body. Hence, for accurate imaging the theoretical model should be based on solution of the radiative transfer equation. A similar procedure can be applied to images of cloud distribution obtained using a lidar arranged on a satellite, which requires knowledge of the multiple scattering effect of water drops distributed in the cloud on the time-resolved backscattering signals. In both examples, the size of the scatterers can be nearly equal to or larger than the wavelength of light, leading to a large anisotropic factor. The use of low-frequency sound to detect oil-bearing layers deep under the ocean floor is another example.

Currently, numerical approaches, including Monte Carlo simulations, are the main methods in solving the BTE [4–6]. Numerical solution of the BTE is a cumbersome task, since the particle distribution $I(\mathbf{r}, \mathbf{s}, t)$ is a function of position \mathbf{r} , angle \mathbf{s} , and time t , in a six-dimensional space of parameters. An analytical expression for $I(\mathbf{r}, \mathbf{s}, t)$ with quantitative accuracy can greatly reduce the computation burden in modeling particle and light propagation in scattering media, which is essential for imaging in turbid media, because the inverse

reconstruction process calls the forward model many times.

Recently, we have developed an analytical solution of the time-dependent elastic BTE in an infinite uniform medium with an arbitrary phase function [7,8]. The exact spatial cumulants of $I(\mathbf{r}, \mathbf{s}, t)$ up to an arbitrary high order at any angle and any time have been derived. A cutoff at second order of the cumulants $I(\mathbf{r}, \mathbf{s}, t)$ can be approximately expressed by a Gaussian distribution, which has the exact first cumulant (the position of the center of the distribution) and the exact second cumulant (the half-width of the spread of the distribution). The cumulant solution of BTE has been extended to the case of a polarized photon distribution, and to semi-infinite and slab geometries. Using a perturbation method, the distribution $I(\mathbf{r}, \mathbf{s}, t)$ in a weak heterogeneous medium can be calculated based on the cumulant solution of the BTE.

The analytical cumulant solution of the BTE obtained, although it has exact center and half-width, is not satisfactory in two respects. First, one cannot ensure that the summation over l in the expressions shown in Sec. II is convergent at very early times. Second, a remarkable fault of the Gaussian distribution at early times is that particles at the front edge of the distribution travel faster than the free speed of the particles in the medium, thus violating causality, especially for those particles moving along near forward directions. The Gaussian distribution is accurate at long times and in the backscattering case, since many collisions lead to a Gaussian distribution according to the central limit theorem.

In this paper, the analytical cumulant solution of the BTE has been improved compared to our previous work [7] in these two respects. For solving the first problem, we make a separation of the ballistic component from the total $I(\mathbf{r}, \mathbf{s}, t)$ and compute the cumulants for the scattered component $I^{(s)}(\mathbf{r}, \mathbf{s}, t)$. This treatment ensures convergent summation over l . Also this separation provides a clearer picture of particle propagation. In the time-resolved transmission profile the ballistic component is described by a sharp jump exactly at the ballistic time, separated from the later scattered component. For solving the second problem two approaches are

used. The first method is to calculate the distribution including the higher-order cumulants, based on our work in Ref. [8]. However, computation of high-order cumulants is a cumbersome task. In the second method the Gaussian distribution is replaced by a different-shaped form, which satisfies causality, and maintains the correct center position and the correct half-width of the distribution computed by our analytical approach. There are infinite choices of the shapes of the distribution satisfying these conditions; we choose a simple analytical form. At long times, the reshaped distribution tends to the Gaussian distribution. Our results show that the reshaped distribution matches that obtained using Monte Carlo simulation much better than the Gaussian distribution.

The paper is organized as follows. In Sec. II we briefly review the main results of the analytical cumulant solution of the BTE. Section III presents a separation of the ballistic component from the scattered component, which makes the summation over l convergent. Section IV improves the distribution at early times using two approaches, and presents the numerical result compared with the Monte Carlo simulation. Section V is devoted to discussion and conclusions.

II. THE ANALYTICAL CUMULANT SOLUTION OF THE BTE

The elastic Boltzmann kinetic equation of particles, with magnitude of velocity v , for the distribution function $I(\mathbf{r}, \mathbf{s}, t)$ as a function of time t , position \mathbf{r} , and direction \mathbf{s} , in an infinite uniform medium, from a point pulse light source, $\delta(\mathbf{r}-\mathbf{r}_0)\delta(\mathbf{s}-\mathbf{s}_0)\delta(t-t_0)$, is given by

$$\begin{aligned} & \partial I(\mathbf{r}, \mathbf{s}, t) / \partial t + v \mathbf{s} \cdot \nabla_{\mathbf{r}} I(\mathbf{r}, \mathbf{s}, t) + \mu_a I(\mathbf{r}, \mathbf{s}, t) \\ &= \mu_s \int P(\mathbf{s}, \mathbf{s}') I(\mathbf{r}, \mathbf{s}', t) d\mathbf{s}' - \mu_s I(\mathbf{r}, \mathbf{s}, t) \\ &+ \delta(\mathbf{r}-\mathbf{r}_0) \delta(\mathbf{s}-\mathbf{s}_0) \delta(t-t_0) \end{aligned} \quad (1)$$

where μ_s is the scattering rate, μ_a is the absorption rate, and $P(\mathbf{s}, \mathbf{s}')$ is the phase function, normalized to $\int P(\mathbf{s}, \mathbf{s}') d\mathbf{s}' = 1$. The phase function is assumed to depend only on the scattering angle in an isotropic medium. Under this assumption, an arbitrary phase function can be handled. We expand the phase function in Legendre polynomials with constant coefficients,

$$P(\mathbf{s}, \mathbf{s}') = \frac{1}{4\pi} \sum_l a_l P_l(\mathbf{s} \cdot \mathbf{s}'). \quad (2)$$

Recently, we have developed a different approach to obtain an analytical solution of the BTE in an infinite uniform medium, based on a cumulant expansion [7,8].

We briefly review the concept of the "cumulant" in a one-dimensional (1D) case. Consider a random variable x , with a probability distribution function $f(x)$. Instead of using $f(x)$ to describe the distribution, we define the n th moment of x ,

$$\langle x^n \rangle = \int x^n f(x) dx, \quad (3)$$

and correspondingly the n th cumulant $\langle x^n \rangle_c$ defined by

$$\exp \left(\sum_{n=1}^{\infty} \langle x^n \rangle_c (it)^n / n! \right) = \langle \exp(itx) \rangle = \sum_{n=0}^{\infty} \langle x^n \rangle (it)^n / n! \quad (4)$$

The first cumulant $\langle x \rangle_c$ is the mean position of x . The second cumulant $\langle x^2 \rangle_c$ represents the half-width of the distribution. The higher cumulants are related to the detailed shape of the distribution. For example, $\langle x^3 \rangle_c$ describes the skewness or asymmetry of the distribution, and $\langle x^4 \rangle_c$ describes the "kurtosis" of the distribution, that is, the extent to which it differs from the standard bell shape associated with the Gaussian distribution function. The cumulants hence describe the distribution in an intrinsic way by subtracting off the effects of all lower-order moments. In the 3D case, the first cumulant has three components, the second cumulant has six components, and so on.

We have derived an explicit algebraic expression for the spatial cumulants at any angle and any time, exact up to an arbitrarily high order n [8]. This means the distribution function $I(\mathbf{r}, \mathbf{s}, t)$ can be computed to any desired accuracy. At the second order, $n=2$, an analytic explicit expression for distribution function $I(\mathbf{r}, \mathbf{s}, t)$ is obtained [7,8]. This distribution is Gaussian in position, which is accurate at later times, but only provides the exact mean position and the exact half-width at early times.

The Gaussian distribution of the second-order cumulant solution is written as

$$\begin{aligned} I(\mathbf{r}, \mathbf{s}, t) &= \frac{F(\mathbf{s}, \mathbf{s}_0, t)}{(4\pi)^{3/2} (\det B)^{1/2}} \\ &\times \exp \left[-\frac{1}{4} (B^{-1})_{\alpha\beta} (r - r^c)_{\alpha} (r - r^c)_{\beta} \right], \end{aligned} \quad (5)$$

where $F(\mathbf{s}, \mathbf{s}_0, t)$ is the total angular distribution $F(\mathbf{s}, \mathbf{s}_0, t) = \int I(\mathbf{r}, \mathbf{s}, t) d\mathbf{r}$, which has the following exact expression:

$$\begin{aligned} F(\mathbf{s}, \mathbf{s}_0, t) &= \exp(-\mu_a t) \sum_l \frac{2l+1}{4\pi} \exp(-g_l t) P_l(\mathbf{s} \cdot \mathbf{s}_0) \\ &= \exp(-\mu_a t) \sum_l \frac{2l+1}{4\pi} \exp(-g_l t) \sum_m Y_{lm}(\mathbf{s}) Y_{lm}^*(\mathbf{s}_0), \end{aligned} \quad (6)$$

where

$$g_l = \mu_s [1 - a_l / (2l+1)]. \quad (7)$$

Two special values of g_l are $g_0=0$, which follows from the normalization of $P(\mathbf{s}, \mathbf{s}')$, and $g_1=v/l_{tr}$, where l_{tr} is the transport mean free path, defined by $l_{tr}=v/[\mu_s(1-\langle \cos \theta \rangle)]$, where $\langle \cos \theta \rangle$ is the average of $\mathbf{s} \cdot \mathbf{s}'$ with $P(\mathbf{s}, \mathbf{s}')$ as weight. In Eq. (6), $Y_{lm}(\mathbf{s})$ are spherical harmonics normalized to $4\pi/(2l+1)$.

The center of the packet (the first cumulant), denoted by \mathbf{r}^c , is located at

$$\mathbf{r}_z^c = G \sum_l A_l P_l(\cos \theta) [(l+1)f(g_l - g_{l+1}) + lf(g_l - g_{l-1})], \quad (8)$$

$$r_x^c = G \sum_l A_l P_l^{(1)}(\cos \theta) \cos \phi [f(g_l - g_{l-1}) - f(g_l - g_{l+1})], \quad (9)$$

where $G = v \exp(-\mu_d t) / F(\mathbf{s}, \mathbf{s}_0, t)$, $A_l = (1/4\pi) \exp(-g_l t)$, and for any variable x ,

$$f(x) = [\exp(xt) - 1]/x. \quad (10)$$

r_y^c is obtained by replacing $\cos \phi$ in Eq. (9) by $\sin \phi$. In Eqs. (8) and (9), $P_l^{(m)}(\cos \theta)$ is the associated Legendre function.

The square of the average spread half-width (the second cumulant) is given by

$$B_{\alpha\beta} = v G \Delta_{\alpha\beta} - r_\alpha^c r_\beta^c / 2, \quad (11)$$

where all the coefficients are functions of angle and time:

$$\Delta_{zz} = \sum_l A_l P_l(\cos \theta) \left[\frac{l(l-1)}{2l-1} E_l^{(1)} + \frac{(l+1)(l+2)}{2l+3} E_l^{(2)} + \frac{l^2}{2l-1} E_l^{(3)} + \frac{(l+1)^2}{2l+3} E_l^{(4)} \right], \quad (12)$$

$$\begin{aligned} \Delta_{xx,yy} = \sum_l \frac{1}{2} A_l P_l(\cos \theta) & \left[-\frac{l(l-1)}{2l-1} E_l^{(1)} - \frac{(l+1)(l+2)}{2l+3} E_l^{(2)} + \frac{l(l-1)}{2l-1} E_l^{(3)} + \frac{(l+1)(l+2)}{2l+3} E_l^{(4)} \right] \\ & \pm \sum_l \frac{1}{2} A_l P_l^{(2)}(\cos \theta) \cos(2\phi) \\ & \times \left[\frac{1}{2l-1} E_l^{(1)} + \frac{1}{2l+3} E_l^{(2)} - \frac{1}{2l-1} E_l^{(3)} - \frac{1}{2l+3} E_l^{(4)} \right], \end{aligned} \quad (13)$$

where (+) corresponds to Δ_{xx} and (-) corresponds to Δ_{yy} ,

$$\Delta_{xy} = \Delta_{yx} = \sum_l \frac{1}{2} A_l P_l^{(2)}(\cos \theta) \sin(2\phi) \left[\frac{1}{2l-1} E_l^{(1)} + \frac{1}{2l+3} E_l^{(2)} - \frac{1}{2l-1} E_l^{(3)} - \frac{1}{2l+3} E_l^{(4)} \right], \quad (14)$$

$$\Delta_{xz} = \Delta_{zx} = \sum_l \frac{1}{2} A_l P_l^{(1)}(\cos \theta) \cos \phi \left[\frac{2(l-1)}{2l-1} E_l^{(1)} - \frac{2(l+2)}{2l+3} E_l^{(2)} + \frac{1}{2l-1} E_l^{(3)} + \frac{1}{2l+3} E_l^{(4)} \right]. \quad (15)$$

Δ_{yz} is obtained by replacing $\cos \phi$ in Eq. (15) by $\sin \phi$. In Eqs. (12)–(15) $E_l^{(1-4)}$ are given by

$$E_l^{(1)} = [f(g_l - g_{l-2}) - f(g_l - g_{l-1})] / (g_{l-1} - g_{l-2}), \quad (16)$$

$$E_l^{(2)} = [f(g_l - g_{l+2}) - f(g_l - g_{l+1})] / (g_{l+1} - g_{l+2}), \quad (17)$$

$$E_l^{(3)} = [f(g_l - g_{l-1}) - t] / (g_l - g_{l-1}), \quad (18)$$

$$E_l^{(4)} = [f(g_l - g_{l+1}) - t] / (g_l - g_{l+1}). \quad (19)$$

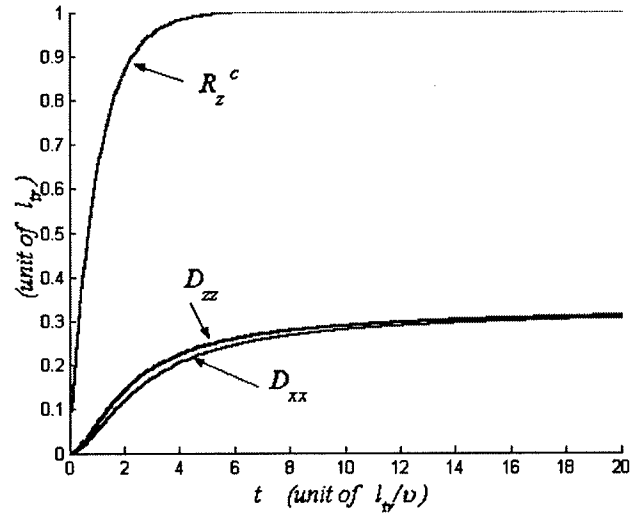


FIG. 1. The moving center R_z^c and the diffusion coefficients D_{zz} and D_{xx} of the particle density function as functions of time t .

The second order cumulant approximation for the particle density distribution $N(\mathbf{r}, t)$ has a Gaussian shape:

$$\begin{aligned} N(\mathbf{r}, t) = & \frac{1}{(4\pi D_{zz} v t)^{1/2}} \frac{1}{4\pi D_{xx} v t} \exp \left[-\frac{(z - R_z^c)^2}{4 D_{zz} v t} \right] \\ & \times \exp \left[-\frac{(x^2 + y^2)}{4 D_{xx} v t} \right] \exp(-\mu_d t), \end{aligned} \quad (20)$$

with a moving center located at

$$R_z^c = v[1 - \exp(-g_1 t)] / g_1, \quad (21)$$

and the corresponding time-dependent diffusion coefficients are given by

$$\begin{aligned} D_{zz} = \frac{v}{3t} & \left\{ \frac{t}{g_1} - \frac{3g_1 - g_2}{g_1^2(g_1 - g_2)} [1 - \exp(-g_1 t)] \right. \\ & \left. + \frac{2}{g_2(g_1 - g_2)} [1 - \exp(-g_2 t)] - \frac{3}{2g_1^2} [1 - \exp(-g_1 t)]^2 \right\}, \end{aligned} \quad (22)$$

$$\begin{aligned} D_{xx} = D_{yy} = \frac{v}{3t} & \left\{ \frac{t}{g_1} + \frac{g_2}{g_1^2(g_1 - g_2)} [1 - \exp(-g_1 t)] \right. \\ & \left. - \frac{1}{g_2(g_1 - g_2)} [1 - \exp(-g_2 t)] \right\}. \end{aligned} \quad (23)$$

Each distribution in Eqs. (5) and (20) describes a particle “cloud” anisotropically spreading from a moving center, with time-dependent diffusion coefficients. As shown in Fig. 1, at early time $t \rightarrow 0$, the mean position of the photons moves along the \mathbf{s}_0 direction with speed v , and the diffusion coefficient tends to zero. These results present a clear picture of nearly ballistic motion at $t \rightarrow 0$. With increase of time, the motion of the center slows down, and the diffusion coefficients increase from zero. This stage of particle migration is often called a “snakelike mode.” At late times, the total angular distribution function tends to become isotropic. The

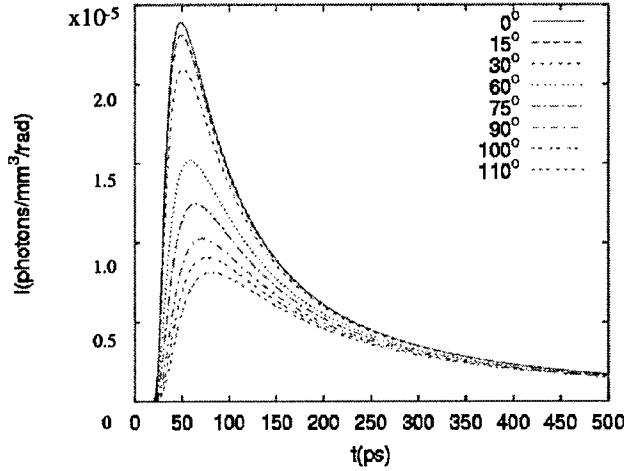


FIG. 2. Light distribution in an infinite uniform medium as a function of time at different received angles, using the second cumulant solution of the BTE (Gaussian distribution), where the detector is located at $z=10$ mm from the source in the incident direction. The parameters for this calculation are $l_{tr}=2$ mm, the absorption length $l_a=300$ mm, the phase function is computed using Mie theory for polystyrene spheres with diameter $d=1.11$ μ m in water, and the wavelength of the laser source $\lambda=625$ nm, which gives the g factor $g=0.926$.

particle density, at $t \gg l_{tr}/v$ and $r \gg l_{tr}$, tends toward the center-moved ($1l_{tr}$) diffusion solution with the diffusive coefficient $l_{tr}/3$. Therefore, our solution quantitatively describes how particles migrate from nearly ballistic motion, to snakelike motion, and then to diffusive motion.

Figure 2 shows the calculated distribution as a function of time at different receiving angles in an infinite uniform medium, computed by the second order cumulant solution, where the detector is located at $5l_{tr}$ from the source in the incident direction of the source. Figure 2 shows anisotropy of the distribution at a distance of $5l_{tr}$ from the source. This type of distribution has been demonstrated by time-resolved experiments [9].

The analytical solution obtained, although it has the exact center and half-width, is not satisfactory in two respects. First, at very early times, $\exp(-g_l t) \rightarrow 1$ for all l ; hence, one cannot ensure that summation over l is convergent. Second, particles at the front edge of the Gaussian distribution travel faster than the speed v , thus violating causality.

III. SEPARATING THE BALLISTIC COMPONENT FROM THE SCATTERED COMPONENT

In order to make the summation over l convergent, we separate the ballistic component from the total $I(\mathbf{r}, \mathbf{s}, t)$, and compute the cumulants for the scattered component $I^{(s)}(\mathbf{r}, \mathbf{s}, t)$.

The ballistic component is the solution of the homogeneous Boltzmann transport equation, which is the transport equation, Eq. (1), without the "scattering in" term [the first term in the right side of Eq. (1)]. The solution of the ballistic component is given by

$$I^{(b)}(\mathbf{r}, \mathbf{s}, t) = \exp[-(\mu_s + \mu_a)t] \delta(\mathbf{r} - v\mathbf{s}t) \delta(\mathbf{s} - \mathbf{s}_0). \quad (24)$$

The moments of the ballistic component can be easily calculated. When \mathbf{s}_0 is along z , we have

$$\int z^n I^{(b)}(\mathbf{r}, \mathbf{s}, t) d^3r = \exp[-(\mu_s + \mu_a)t] (vt)^n \delta(\mathbf{s} - \mathbf{s}_0), \quad (25)$$

and other moments related to $z^{n_1} x^{n_2} y^{n_3}$ ($n_2, n_3 \neq 0$) are zero.

The total distribution is the summation of the ballistic component and the scattered component:

$$I(\mathbf{r}, \mathbf{s}, t) = I^{(b)}(\mathbf{r}, \mathbf{s}, t) + I^{(s)}(\mathbf{r}, \mathbf{s}, t); \quad (26)$$

hence, the moments of the scattered component can be obtained by subtracting the corresponding ballistic moments from the moments of $I(\mathbf{r}, \mathbf{s}, t)$. For example, we have

$$\int z^n I^{(s)}(\mathbf{r}, \mathbf{s}, t) d^3r = \int z^n I(\mathbf{r}, \mathbf{s}, t) d^3r - \int z^n I^{(b)}(\mathbf{r}, \mathbf{s}, t) d^3r. \quad (27)$$

Notice that

$$\delta(\mathbf{s} - \mathbf{s}_0) = \sum_l [(2l+1)/4\pi] P_l(\mathbf{s} \cdot \mathbf{s}_0). \quad (28)$$

Substituting Eqs. (25) and (28) into Eq. (27), the corresponding cumulants for the scattered component $I^{(s)}(\mathbf{r}, \mathbf{s}, t)$ can be easily obtained; they replace Eqs. (6), (8), and (12) by

$$F^{(s)}(\mathbf{s}, \mathbf{s}_0, t) = \exp(-\mu_a t) \sum_l \frac{2l+1}{4\pi} [\exp(-g_l t) - \exp(-\mu_s t)] P_l(\mathbf{s} \cdot \mathbf{s}_0), \quad (29)$$

$$r_z^{(s)} = G \sum_l P_l(\cos \theta) \frac{1}{4\pi} \{ \exp(-g_l t) [(l+1)f(g_l - g_{l+1}) + lf(g_l - g_{l-1})] - (2l+1)t \exp(-\mu_s t) \}, \quad (30)$$

$$\Delta_{zz}^{(s)} = \sum_l P_l(\cos \theta) \frac{1}{4\pi} \left\{ \exp(-g_l t) \left[\frac{l(l-1)}{2l-1} E_l^{(1)} + \frac{(l+1)(l+2)}{2l+3} E_l^{(2)} + \frac{l^2}{2l-1} E_l^{(3)} + \frac{(l+1)^2}{2l+3} E_l^{(4)} \right] - \frac{l^2(2l+1)}{2} \exp(-\mu_s t) \right\}. \quad (31)$$

The expressions for the other components of the first and second cumulants are unchanged, provided all $F(\mathbf{s}, \mathbf{s}_0, t)$ in G in Sec. II are replaced by $F^{(s)}(\mathbf{s}, \mathbf{s}_0, t)$. Note that Eq. (28) actually is equal to zero at $\mathbf{s} \neq \mathbf{s}_0$, and there is no ballistic component in these directions.

The replacement of equations in Sec. II by Eqs. (29)–(31) greatly improves the calculation of cumulants at very early times. By the subtraction introduced above, the terms for large l approach zero, and summation over l becomes convergent at very early times. When $t \rightarrow 0$, $g_l = \mu_s [1 - a_l/(2l+1)]$ [see Eq. (7)] approaches μ_s for large l , $f(g_l - g_{l+1}) \approx t$

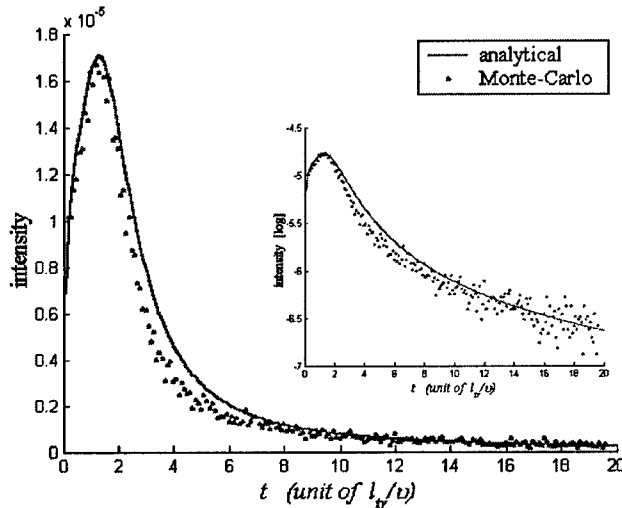


FIG. 3. Time-resolved profile of the backscattered (180°) photon intensity inside a disk with center at $r=0$, radius $R=l_{tr}$, thickness $dz=0.1l_{tr}$, and the received solid angle $d\cos\theta=0.001$, normalized to inject one photon. The Heyney-Greenstein phase function with $g=0.9$ is used, and $1/l_a=0$. The solid curve is for the second cumulant solution (Gaussian distribution), and dots are for the Monte Carlo simulation. The inset diagram shows the same result drawn using a logarithmic scale for intensity.

[see Eq. (10)], and $E_l^{(1-4)} \approx t^2/2$ [see Eqs. (16)–(19)], which results in cancellation in the summand for large l at very early times.

An example of successful use of this replacement is the calculation of backscattering. When $\theta=180^\circ$, $P_l(\cos\theta)=1$ or -1 , depending on whether l is even or odd. The computed r_z^c at very early times using Eq. (8) oscillates with a cutoff of l . But the computed $r_z^{c(s)}$ at very early times using Eq. (30) becomes stable. Calculation shows that $r_z^{c(s)}=0$ at any time when $\theta=180^\circ$.

Figure 3 shows the computed time profile of the backscattering intensity $I^{(s)}(\mathbf{r}, \mathbf{s}, t)$ at a detector centering at $\mathbf{r}=0$ and received at an angle $\theta=180^\circ$, which actually is the total backscattering intensity $I(\mathbf{r}, \mathbf{s}, t)$ because $\mathbf{s} \neq \mathbf{s}_0$, compared with the Monte Carlo simulation. The absolute value of the intensity, as well as the shape of the time-resolved profile, computed using our analytical cumulant solution of the BTE match well with those of the Monte Carlo simulation. The inset diagram is the same result drawn using a logarithmic scale for intensity. Note that this result of backscattering, based on the solution of the BTE, is for a detector located near the source, different from other backscattering results based on the diffusion model, which is only valid when detector is located at a distance of several l_{tr} from the source.

IV. SHAPE OF THE PARTICLE DISTRIBUTION

If the cumulants with order $n > 2$ are assumed all zero, the distribution becomes Gaussian. The Gaussian distribution is accurate at long times. At early times, particles at the front edge of the distribution travel faster than the free speed of the particles, thus violating causality, especially for particles

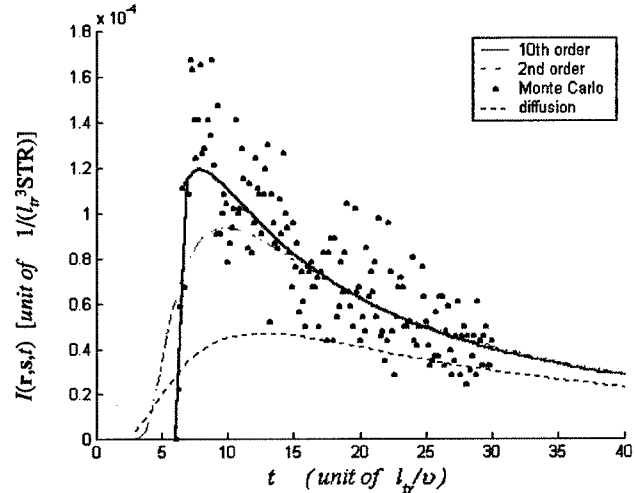


FIG. 4. Time-resolved profile of transmitted light in an infinite uniform medium, computed using the tenth order cumulant solution (solid curve), the second order cumulant solution (dotted curve), and the diffusion approximation (thick dotted curve), compared with that of the Monte Carlo simulation (discrete dots). The detector is located at $z=6l_{tr}$ from the source along the incident direction, and the received direction is $\theta=0$. The Heyney-Greenstein phase function with $g=0.9$ is used, and the absorption coefficient $1/l_a=0$.

that move along near forward directions. In the following, two approaches are used for overcoming this fault: (A) including higher cumulants; and (B) introducing a reshaped distribution.

A. Calculation including high-order cumulants

We have performed calculations including the higher-order cumulants to obtain a more accurate shape of the distribution. The Codes for calculation are designed based on a formula derived in Ref. [8].

Figure 4 shows $I(\mathbf{r}, \mathbf{s}, t)$ with the detector located at $z=6l_{tr}$ in front of the source and receiving direction along $\theta=0$, computed using the analytical cumulant solution up to tenth order of the cumulants (solid curve), up to the second order cumulants (dotted curve), in the diffusion approximation (thick dotted curve), and the Monte Carlo simulation (discrete dots). The figure shows that the tenth order cumulant solution is located in the middle of the data obtained by the Monte Carlo simulation, and $I(\mathbf{r}, \mathbf{s}, t) \approx 0$ before the ballistic time $t_b=6l_{tr}/v$. The second order cumulant solution has nonzero $I(\mathbf{r}, \mathbf{s}, t)$ before t_b , which violates causality. The computed $N(\mathbf{r}, t)/4\pi$ using the diffusion model has a large discrepancy with the Monte Carlo simulation, and the diffusion solution has more nonzero components before t_b , which violates causality.

Using the second order cumulant solution, the distribution function can be computed very fast. The associated Legendre functions can be quickly computed using recurrence relations with accuracy limited by the computer machine error. It takes 1 min to produce 10^5 data points of $I(\mathbf{r}, \mathbf{s}, t)$ on a personal computer. On the other hand, in order to reduce the statistical fluctuation to the level shown in Fig. 4, 10^9 events

are counted in the Monte Carlo simulation, which takes tens of hours computation time on a personal computer. Computation of high-order cumulants also is a cumbersome task, because the number of involved terms rapidly grows with increase of the order n . Also, for a distribution function that is positive definite, the Bust theorem states that the existence of nonzero cumulants of any order higher than 2 will be accompanied by nonzero cumulants of all orders [10]. Therefore, no matter how the cutoff at a finite high order n is taken, the cumulant solution of the BTE cannot be regarded as exact.

B. Reshaping the particle distribution

For practical applications, we use a semiphenomenological model. The Gaussian distribution is replaced by a different-shaped form, which maintains the correct center position and the correct half-width of the distribution. This distribution satisfies causality, namely, $I(\mathbf{r}, \mathbf{s}, t) = 0$ outside the ballistic limit vt . There are an infinite number of choices of shape of the distribution under the above conditions. We choose a simple analytical form as discussed later. At long times, the half-width of the distribution $\sigma \sim (4B)^{1/2}$, with B shown in Eq. (11), spreads as $t^{1/2}$; hence, $\sigma \ll vt$ at large t , and the Gaussian distribution at long times with half-width σ can be regarded as completely inside the ballistic sphere. The reshaped distribution of $I(\mathbf{r}, \mathbf{s}, t)$ hence should approach the Gaussian distribution at long times.

1. 1D density

We first discuss the one-dimensional density as an example to explain our model.

The Gaussian distribution of 1D density is described by

$$N(z) = (4\pi D_{zz}vt)^{-1/2} \exp[-(z - R_z^c)^2 / (4D_{zz}vt)], \quad (32)$$

where R_z^c and D_{zz} are given in Eqs. (21) and (22). As shown in Fig. 5, although the 1D Gaussian spatial distribution (the dashed curve) at time $t = 2l_{tr}/v$, Eq. (32), has the correct center and half-width, the curve deviates from the distribution computed by the Monte Carlo simulation (dots), and a remarkable part of the distribution appears outside the ballistic limit $vt = 2l_{tr}$. At early times the spatial distribution is not symmetric about the center R^c . When R^c moves from the source toward the forward side, causality prohibits particles appearing beyond vt . This requires the particles in the forward side to be squeezed in a narrow region between R^c and vt . For a balance of the parts of the distribution in the forward and backward sides of R^c , the peak of the distribution should move to a point at the forward side and the height of the peak should increase. The earlier the time t , the closer is R^c to vt , and the asymmetry of the distribution becomes stronger. Based on this observation we propose the following analytical expression: (1) to move the peak position of the distribution from R_z^c to z_c , where the parameter z_c will be determined later; (2) to take this point as the origin of new coordinates; and (3) to use the following form of the shape of the 1D density in the new coordinates:

$$N(\tilde{z}) = b \exp(-\alpha^2 \tilde{z}^2) [1 - (\tilde{z}/\tilde{z}_\pm)^2], \quad (33)$$

where

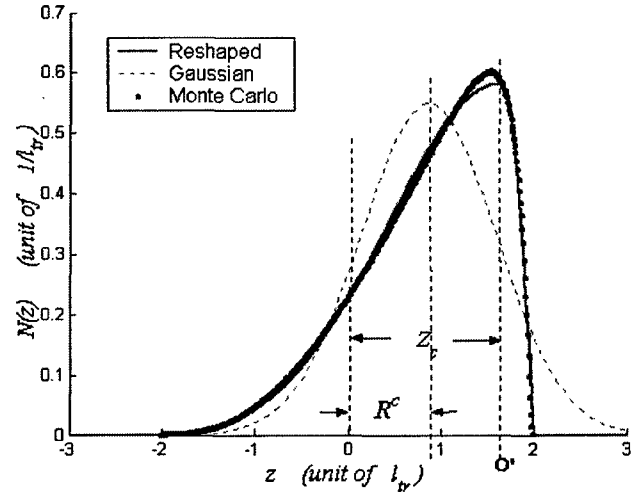


FIG. 5. The 1D spatial photon density at time $t = 2l_{tr}/v$, obtained by the reshaped form Eq. (33) (solid curve) and the Gaussian form (dashed curve), compared with that of the Monte Carlo simulation (dots). The Heyney-Greenstein phase function with $g = 0.9$ is used, and $1/l_a = 0$. In the figure, the unit on the z axis is l_{tr} ; R^c is the center position of the distribution computed by the cumulant solution; z_c is the distance between the origin of the new coordinates and the source.

$$\tilde{z}_\pm = vt \mp z_c \quad \begin{cases} \tilde{z} > 0, \\ \tilde{z} < 0. \end{cases} \quad (34)$$

At the ballistic limit $\tilde{z} = \tilde{z}_\pm$, $N(\tilde{z})$ reduces to zero, and $N(\tilde{z}) = 0$ when \tilde{z} is outside of \tilde{z}_\pm . The parameter b in Eq. (33) can be determined by normalization; the parameters (α, z_c) can be determined by fitting the center and half-width of the distribution. This fit requires

$$\int N(\tilde{z}) d\tilde{z} = 1, \quad (35)$$

$$\langle \tilde{z} \rangle = \int \tilde{z} N(\tilde{z}) d\tilde{z} = R_z^c - z_c, \quad (36)$$

$$\langle \tilde{z}^2 \rangle_c = \int (\tilde{z} - \langle \tilde{z} \rangle)^2 N(\tilde{z}) d\tilde{z} = 2D_{zz}vt. \quad (37)$$

The integrals in Eqs. (35)–(37) can be analytically performed; they are related to the standard error function (the incomplete gamma function, or the confluent hypergeometric function of the first kind):

$$F^{(0)}(\beta) = \int_0^\beta e^{-y^2} dy = \frac{\pi^{1/2}}{2} \text{erf}(\beta), \quad (38)$$

$$F^{(1)}(\beta) = \int_0^\beta e^{-y^2} y dy = \frac{1}{2} [1 - e^{-\beta^2}], \quad (39)$$

$$F^{(2n)}(\beta) = \int_0^\beta e^{-y^2} y^{2n} dy = \frac{1}{2}[(2n-1)F^{(2n-2)}(\beta) - \beta^{2n-1}e^{-\beta^2}], \quad (40)$$

$$F^{(2n+1)}(\beta) = \int_0^\beta e^{-y^2} y^{2n+1} dy = \frac{1}{2}[2nF^{(2n-1)}(\beta) - \beta^{2n}e^{-\beta^2}]. \quad (41)$$

For nonlinear fitting a difficulty is how to quickly find a global minimum. The optimization codes require setting a good initial value of the parameters, so the obtained local minimum is the true global minimum. Since we have no experience for setting good initial parameters at a special time, the following procedure is used. At the long time limit $z_c \approx R_z^c$ and $\alpha^2 \approx (4D_{zz}vt)^{-1}$, the distribution approaches the original Gaussian distribution. We make a nonlinear fitting at a point of long time t_m , using these values of the parameters as initial values. Then, we make a fitting at $t_{m-1} = t_m - \Delta t$, where Δt is a small time interval, with the initial values of parameters from those obtained at t_m , to produce parameters at t_{m-1} . Step by step, the parameters in the whole time period can be computed. Our test shows that the fitting program using this procedure runs quickly, with very small fitting error, up to a certain short time limit.

The solid curve in Fig. 5 shows the reshaped spatial distribution, Eq. (33), of 1D density at time $t = 2l_{tr}/v$, using the Heyney-Greenstein phase function with $g=0.9$, which satisfies causality and matches the Monte Carlo result much better than the Gaussian distribution.

2. 3D density

In this case the ballistic limit is represented by a sphere with center located at the source position and the radius vt . We move the peak position of the distribution from R_z^c to z_c along the $s_0 = \hat{z}$ direction, take this point as the origin of new coordinates, and use the following form of the shape of the 3D density as a function of position in the new coordinates, $\tilde{\mathbf{r}}$:

$$N(\tilde{\mathbf{r}}) = b \exp[-\alpha(\tilde{\chi})^2 \tilde{r}^2][1 - (\tilde{r}/\tilde{r}^*)^2], \quad (42)$$

and $N(\tilde{\mathbf{r}}) = 0$ when $\tilde{r} > \tilde{r}^*$, where $\tilde{\chi}$ is the polar angle of $\tilde{\mathbf{r}}$ in the new coordinates, and \tilde{r}^* is the distance between the new origin and the point obtained by extrapolating $\tilde{\mathbf{r}}$ to the surface of the ballistic sphere,

$$\tilde{r}^* = [(vt)^2 - z_c^2 \sin^2(\tilde{\chi})]^{1/2} - \cos(\tilde{\chi})z_c. \quad (43)$$

In Eq. (42) $\alpha(\tilde{\chi})$ is defined by

$$\alpha(\tilde{\chi})^2 \equiv \alpha_z^2 \cos^2(\tilde{\chi}) + \alpha_\perp^2 \sin^2(\tilde{\chi}). \quad (44)$$

The parameters b can be determined by normalization; the parameters $(\alpha_z, \alpha_\perp, z_c)$ are determined by fitting the center and half-width of the distribution. This fit requires

$$\langle \tilde{z} \rangle = \int \tilde{r} \cos(\tilde{\chi}) N(\tilde{\mathbf{r}}) d^3\tilde{\mathbf{r}} = R_z^c - z_c, \quad (45)$$

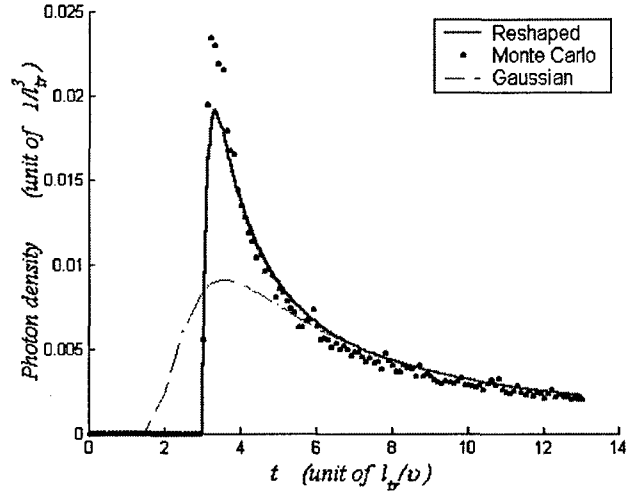


FIG. 6. Time-resolved profile of 3D photon density, where the detector is located at $z = 3l_{tr}$ from the source along the incident direction, obtained by the reshaped form Eq. (42) (solid curve) and the Gaussian form (dashed curve), compared with that of the Monte Carlo simulation (dots). The Heyney-Greenstein phase function with $g=0.9$ is used, and the absorption coefficient $1/l_a = 0$.

$$\int [\tilde{r} \cos(\tilde{\chi}) - \langle \tilde{z} \rangle]^2 N(\tilde{\mathbf{r}}) d^3\tilde{\mathbf{r}} = 2D_{zz}vt, \quad (46)$$

$$\int [\tilde{r} \sin(\tilde{\chi})]^2 N(\tilde{\mathbf{r}}) d^3\tilde{\mathbf{r}} = 4D_{xx}vt. \quad (47)$$

In the above integral $d^3\tilde{\mathbf{r}} = 2\pi\tilde{r}^2 d\tilde{r} d\cos(\tilde{\chi})$, integration over $\tilde{\mathbf{r}}$ can be analytically performed, and integration over $\tilde{\chi}$ is performed numerically.

Figure 6 shows the computed time profile of the 3D density $N(\mathbf{r}, t)$, with the source at the origin and the detector located at $\mathbf{r} = (0, 0, 3l_{tr})$, using the Heyney-Greenstein phase function with $g=0.9$. The solid curve is for the reshaped form using Eq. (42). The dashed curve is for the Gaussian form, and the dots are for the Monte Carlo simulation. The results clearly demonstrate an improvement by use of the reshaped form over use of the Gaussian form. The nonzero intensity before $t_b = 3l_{tr}/v$ in the reshaped form has been completely removed, while the Gaussian distribution has nonzero components before t_b . The reshaped time profile matches with the result of the Monte Carlo simulation in most of the time period, but the peak values are about 20% lower. The errors are much smaller than those of the Gaussian distribution. By integration over time, the density for the steady state can be obtained. The difference in the steady state density between the reshaped analytical model and the Monte Carlo simulation is about 3%.

3. Distribution function $I^{(s)}(\mathbf{r}, \mathbf{s}, t)$

When the detector is located less than $8l_{tr}$ from the source in a medium with large g factor, the distribution function $I^{(s)}(\mathbf{r}, \mathbf{s}, t)$ is highly anisotropic, and the intensity received

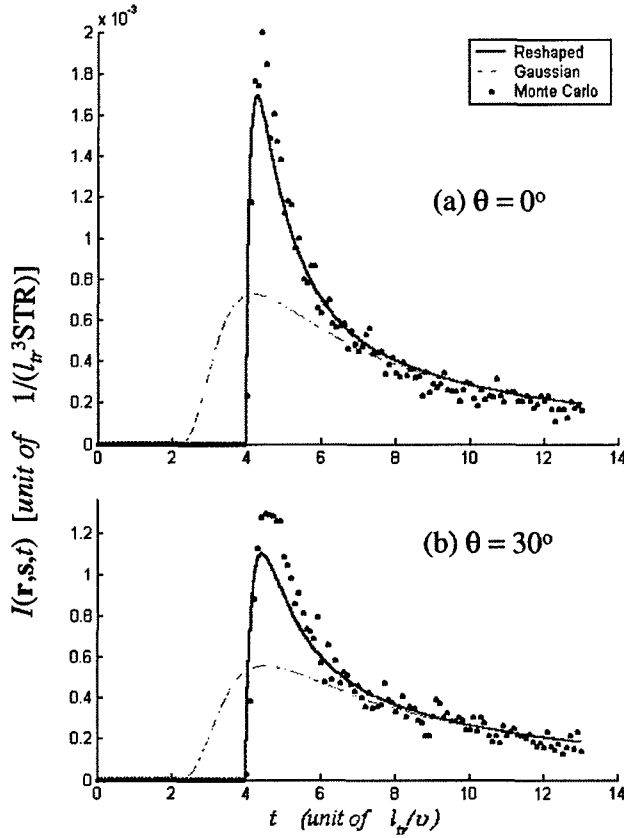


FIG. 9. Time-resolved profile of photon distribution function, for light directions $\theta =$ (a) 0° and (b) 30° , where the detector is located at $z = 4l_{tr}$ from the source along the incident direction. Other parameters are the same as in Fig. 8.

result much better than the Gaussian distribution, but the peak value is about 40% lower than that of the Monte Carlo simulation. Integrating over time shows that the difference in the steady state distribution function between the reshaped analytical model and the Monte Carlo simulation is about 7%. The ratio of the peak value at $\theta = 30^\circ$ is about 60% of that at $\theta = 0^\circ$, which shows stronger anisotropy at $d = 3l_{tr}$ compared to that at $d = 5l_{tr}$ shown in Fig. 2.

Figure 9 shows the distribution function $I^{(s)}(\mathbf{r}, \mathbf{s}, t)$ when the detector is located at $4l_{tr}$ in front of the source. The reshaped distribution matches the Monte Carlo result much better than that at $3l_{tr}$. It shows that the peak intensity at $4l_{tr}$ is about one order of magnitude smaller than that at $3l_{tr}$, but intensity decays with time more slowly at $4l_{tr}$ than at $3l_{tr}$.

V. DISCUSSION

While causality, together with the correct center and half-width of the distribution, are major controlling factors in determining the shape and the range of the particle distribution, the detailed shapes are, to some extent, different in the different models. Our choice of the reshaped form is based on simplicity and ease of computation, which obviously is not the only available choice. The initial results show that for $g = 0.9$ the parameters in our model can be quickly obtained

using the above fitting procedure up to $t \geq 4l_{tr}/v$ for the 3D case (up to $t \geq 2l_{tr}/v$ for 1D density). The Monte Carlo simulation is more time consuming in this time region. This model may work well for $g < 0.9$ in the above time region, because there is less forward scattering for a smaller g factor. The fitting error begins to increase during $3l_{tr}/v < t < 4l_{tr}/v$. At early time $t < 3l_{tr}/v$, \mathbf{r}^c becomes very close to the ballistic limit $v\mathbf{t}$; the front edge of the distribution almost perpendicularly jumps at the position $v\mathbf{t}$. In this case, the parameter $z_c \approx v\mathbf{t}$ in our model, is difficult to adjust through the fitting program. A more suitable model in this early time period is needed. Of course, Monte Carlo simulation also runs fast for short times and small spatial regions. For \mathbf{s} at the near backscattering direction, the Gaussian distribution can be a good approximation as shown in Fig. 3, because most particles suffer many scattering events to transfer from the forward direction to the backward direction. Our calculation shows that the center position \mathbf{r}^c is close to the source for $\theta \approx 180^\circ$ and far from the ballistic limit; hence, reshaping has little effect on the backscattering case.

In addition to improving convergence, separating the ballistic component from the scattered component also provides a more appropriate time-resolved profile for transmission. In the time-resolved transmission profile the ballistic component is described by a sharp jump exactly at time $v\mathbf{t}$, separated from the later scattered component. The intensity of the ballistic component, compared to the scattered component, strongly depends on the g factor. For $g = 0$, $l_{tr} = l_s$, the ballistic component decays to $\exp(-1) = 0.368$ at distance l_{tr} . But for $g = 0.9$ it decays to $\exp(-10) = 4.54 \times 10^{-5}$ at l_{tr} , because $l_{tr} = 10l_s$. The jump of the ballistic component can be seen in experiments of transmission of light for a medium of small sized scatterers (small g factor), but is difficult to observe for a medium of large sized scatterers (large g factor). Our formula presented in Sec. III provides a good estimation for both small and large g factors by explicitly separating these two components.

Using the obtained analytical expressions, the distribution $I(\mathbf{r}, \mathbf{s}, t)$ can be computed very fast. The cumulant solution of the BTE has been extended to the case of a polarized photon distribution [11], and to semi-infinite and slab geometries [12]. Using a perturbation method, the distribution $I(\mathbf{r}, \mathbf{s}, t)$ in a weak heterogeneous medium can be calculated based on the cumulant solution of the BTE [12]. The nonlinear effect for strongly heterogeneous objects inside a medium can also be calculated using a correction of the "self-energy" diagram [13]. Hence, the analytical form of the solution of the BTE may have many different applications.

In summary, the analytical cumulant solution of the Boltzmann transport equation is improved in two respects. The ballistic component is separated and the cumulants for the scattered component are computed. This treatment ensures that summation-over l is convergent. We replace the Gaussian distribution by a different shaped form, which satisfies causality, and maintains the correct center position and the correct half-width of the distribution computed by our analytical formula. Our results show that the reshaped distribution matches that obtained by the Monte Carlo simulation much better than does the Gaussian distribution.

ACKNOWLEDGMENTS

This work was supported in part by NASA URC Center for Optical Sensing and Imaging at CCNY (NASA Grant No. NCC-1-03009), in part by the Office of Naval Research

(ONR), and in part by U.S. Army Medical Research and Materials Command. M.X. acknowledges support from the U.S. Department of the Army (Grant No. DAMD17-02-1-0516).

-
- [1] K. M. Case, P. F. Zweifel, *Linear Transport Theory* (Addison-Wesley, New York, 1967).
 - [2] J. J. Duderstadt and W. R. Martin, *Transport Theory* (Wiley, New York, 1979).
 - [3] S. Chandrasekhar, *Radiative Transfer* (Oxford University Press, New York, 1950).
 - [4] P. Kubelka, J. Opt. Soc. Am. **44**, 330 (1954).
 - [5] A. D. Kim and A. Ishimaru, J. Comput. Phys. **152**, 264 (1999).
 - [6] L. Wang, S. L. Jacques, and L. Zheng, Comput. Methods Programs Biomed. **47**, 131 (1995).
 - [7] W. Cai, M. Lax, and R. R. Alfano, Phys. Rev. E **61**, 3871 (2000).
 - [8] W. Cai, M. Lax, and R. R. Alfano, J. Phys. Chem. B **104**, 3996 (2000).
 - [9] M. E. Zevallos, A. Y. Polischuck, B. B. Das, F. Liu, and R. R. Alfano, Phys. Rev. E **57**, 7244 (1998).
 - [10] R. F. Pawula, Phys. Rev. **162**, 186 (1967).
 - [11] W. Cai, M. Lax, and R. R. Alfano, Phys. Rev. E **63**, 016606 (2000).
 - [12] W. Cai, M. Xu, and R. R. Alfano, IEEE J. Sel. Top. Quantum Electron. **9**, 189 (2003).
 - [13] M. Xu, W. Cai, and R. R. Alfano, Opt. Lett. **29**, 1757 (2004).

Electric field Monte Carlo simulation of polarized light propagation in turbid media

Min Xu

Institute for Ultrafast Spectroscopy and Lasers, New York State Center of Advanced Technology for Ultrafast Photonics, and Department of Physics, The City College and Graduate Center of City University of New York, New York, NY 10031

Abstract: A Monte Carlo method based on tracing the multiply scattered electric field is presented to simulate the propagation of polarized light in turbid media. Multiple scattering of light comprises a series of updates of the parallel and perpendicular components of the complex electric field with respect to the scattering plane by the amplitude scattering matrix and rotations of the local coordinate system spanned by the unit vectors in the directions of the parallel and perpendicular electric field components and the propagation direction of light. The backscattering speckle pattern and the backscattering Mueller matrix of an aqueous suspension of polystyrene spheres in a slab geometry are computed using this Electric Field Monte Carlo (EMC) method. An efficient algorithm computing the Mueller matrix in the pure backscattering direction is detailed in the paper.

© 2004 Optical Society of America

OCIS codes: (170.5280) Photon migration; (030.5620) Radiative transfer (290.4210) Multiple scattering; (290.1350) Backscattering (290.7050) Turbid media; (030.6140) Speckle

References and links

1. A. Ishimaru, *Wave propagation and scattering in random media, I and II* (Academic, New York, 1978).
2. A. Yodh and B. Chance, "Spectroscopy and imaging with diffusing light," *Phys. Today* **48**(3), 38–40 (1995).
3. S. K. Gayen and R. R. Alfano, "Emerging optical biomedical imaging techniques," *Opt. Photon. News* **7**(3), 17–22 (1996).
4. S. R. Arridge, "Optical tomography in medical imaging," *Inverse Problems* **15**, R41–R93 (1999).
5. S. Chandrasekhar, *Radiative transfer* (Dover, New York, 1960).
6. K. F. Evans and G. L. Stephens, "A new polarized atmospheric radiative transfer model," *J. Quant. Spectrosc. Radiat. Transfer* **46**, 413–423 (1991).
7. A. D. Kim and M. Moscoso, "Chebyshev Spectral methods for radiative transfer," *SIAM J. Sci. Comput.* **23**, 2074–2094 (2002).
8. A. D. Kim and J. B. Keller, "Light propagation in biological tissue," *J. Opt. Soc. Am. A* **20**, 92–98 (2003).
9. G. W. Kattawar and G. N. Plass, "Radiance and polarization of multiple scattered light from haze and clouds," *Appl. Opt.* **7**, 1519–1527 (1968).
10. I. Lux and L. Koblinger, *Monte Carlo Particle Transport Methods: Neutron and Photon Calculations* (CRC Press, Boca Raton, Fla., 1991).
11. J. M. Schmitt, A. H. Gandjbakhche, and R. F. Bonner, "Use of polarized light to discriminate short-path photons in a multiply scattering medium," *Appl. Opt.* **31**(30), 6535– (1992).
12. P. Brusaglioni, G. Zaccanti, and Q. Wei, "Transmission of a pulsed polarized light beam through thick turbid media: numerical results," *Appl. Opt.* **32**(30), 6142–6150 (1993).
13. M. J. Rakovic, G. W. Kattawar, M. Mehrbeolu, B. D. Cameron, L. V. Wang, S. Rastegar, and G. L. Cote, "Light Backscattering Polarization Patterns from Turbid Media: Theory and Experiment," *Appl. Opt.* **38**(15), 3399–3408 (1999).
14. S. Bartel and A. H. Hielscher, "Monte Carlo Simulations of the Diffuse Backscattering Mueller Matrix for Highly Scattering Media," *Appl. Opt.* **39**(10), 1580–1588 (2000).

15. M. Moscoso, J. B. Keller, and G. Papanicolaou, "Depolarization and blurring of optical images by biological tissue," *J. Opt. Soc. Am. A* **18**(4), 948–960 (2001).
16. H. H. Tynes, G. W. Kattawar, E. P. Zege, I. L. Katsev, A. S. Prikhach, and L. I. Chaikovskaya, "Monte Carlo and Multicomponent Approximation Methods for Vector Radiative Transfer by use of Effective Mueller Matrix Calculations," *Appl. Opt.* **40**(3), 400–412 (2001).
17. B. Kaplan, G. Ledanois, and B. villon, "Mueller Matrix of Dense Polystyrene Latex Sphere Suspensions: Measurements and Monte Carlo Simulation," *Appl. Opt.* **40**(16), 2769–2777 (2001).
18. X. Wang and L. V. Wang, "Propagation of polarized light in birefringent turbid media: A Monte Carlo study," *J. Biomed. Opt.* **7**, 279–290 (2002).
19. G. W. Kattawar, M. J. Raković, and B. D. Cameron, "Laser backscattering polarization patterns from turbid media: theory and experiments," in *Advances in Optical Imaging and Photon Migration*, J. G. Fujimoto and M. S. Patterson, eds., vol. 21 of *OSA TOPS*, pp. 105–110 (1998).
20. J. C. Ramella-Roman, "Imaging skin pathologies with polarized light: empirical and theoretical studies," Ph.D. thesis. OGI School of Science & Engineering at Oregon Health & Science University (2004).
21. H. C. van de Hulst, *Light scattering by small particles* (Dover, New York, 1981).
22. C. F. Bohren and D. R. Huffman, *Absorption and scattering of light by small particles* (John Wiley & Sons, 1983).
23. R. Y. Rubinstein, *Simulation and the Monte Carlo method* (John Wiley & Sons, 1981).
24. J. von Neumann, "Various techniques used in connection with random digits," *J. Res. Natl. Bur. Stand.* **5**, 36–38 (1951).
25. W. H. Press, S. A. Teukolsky, W. T. Vetterling, and B. P. Flannery, *Numerical recipes in C* (Cambridge university press, 1996).
26. P.-E. Wolf and G. Maret, "Weak Localization and Coherent Backscattering of Photons in Disordered Media," *Phys. Rev. Lett.* **55**(24), 2696–2699 (1985).
27. M. P. V. Albada and A. Lagendijk, "Observation of Weak Localization of Light in a Random Medium," *Phys. Rev. Lett.* **55**(24), 2692–2695 (1985).
28. E. Akkermans, P. E. Wolf, and R. Maynard, "Coherent backscattering of light by disordered media: analysis of the peak line shape," *Phys. Rev. Lett.* **56**(14), 1471–1474 (1986).
29. J. W. Goodman, "Statistical properties of laser speckle patterns," in *Laser speckle and related phenomena*, J. C. Dainty, ed., pp. 9–75 (Springer-Verlag, Berlin, 1975).
30. D. S. Saxon, "Tensor Scattering Matrix for the Electromagnetic Field," *Phys. Rev.* **100**(6), 1771–1775 (1955).
31. B. D. Cameron, M. J. Rakovic, M. Mehrbeoglu, G. W. Kattawar, S. Rastegar, L. V. Wang, and G. L. Cot, "Measurement and calculation of the two-dimensional backscattering Mueller matrix of a turbid medium," *Opt. Lett.* **23**(7), 485–487 (1998).
32. I. Berezhnyy and A. Dogariu, "Time-resolved Mueller matrix imaging polarimetry," *Opt. Exp.* **12**(19), 4635–4649 (2004).
33. EMC is available at <http://www.sci.cuny.cuny.edu/minxu>.

1. Introduction

The propagation of polarized light in turbid media is fundamental to many practical applications of considerable interest including remote sensing of clouds and imaging of colloidal suspensions and biological materials[1–4]. Due to the lack of analytical solutions to radiative transfer[5] of polarized light within a bounded medium, numerical solutions[6–8] of the radiative transfer equation and Monte Carlo simulations[9–18] of propagation of polarized light in turbid media have been pursued extensively and applied to characterization of clouds, particle suspensions, and biological materials.

Most Monte Carlo methods trace the Stokes vector $\mathbf{I} = (I, Q, U, V)^T$ in simulation where $I = \langle |E_l|^2 + |E_r|^2 \rangle$, $Q = \langle |E_l|^2 - |E_r|^2 \rangle$, $U = \langle E_l^* E_r + E_l E_r^* \rangle$, $V = -i \langle E_l^* E_r - E_l E_r^* \rangle$, E_l and E_r are two orthogonal complex electric field components perpendicular to the propagation direction, the superscript "T" denotes transpose, and $\langle \rangle$ means ensemble average. Light scattering involves a rotation of the Stokes vector to a local scattering reference frame and the multiplication of the Stokes vector by the 4×4 Mueller matrix which prescribes how polarized light is scattered by an isolated particle in that reference frame. The Stokes vector is summed up at the detector assuming the detected light is incoherent. Many implementations of the above Monte Carlo approach to simulate polarized light propagation in turbid media

have appeared in the literature[9–18]. Some recent work includes [13, 14, 16–18]. Symmetry considerations[19], randomly polarized incident light[17], next event point estimators[17] and other techniques[14, 16] have been investigated to improve the efficiency of the Monte Carlo computation. Various implementations of the above Monte Carlo approach have also been compared[20].

In this article, we present a Monte Carlo method based on tracing the multiply scattered electric field to simulate the propagation of polarized light in turbid media. Multiple scattering of light comprises a series of updates of the parallel and perpendicular components of the complex electric field with respect to the scattering plane by the amplitude scattering matrix and rotations of the local coordinate system spanned by the unit vectors in the directions of the parallel and perpendicular electric field components and the propagation direction of light. The phase of light accrues from phase delays due to the interaction of light with scatterers and propagation through the host medium. In contrast with the conventional Monte Carlo approach based on tracing the Stokes vector, the Electric Field Monte Carlo (EMC) method traces the electric field and phase of light and makes it possible to simulate also coherent properties of multiply scattered light. The algorithm of EMC is straightforward and can be easily adapted to simulate the propagation of polarized light in optically active medium.

After outlining the theoretical formalism of the Electric Field Monte Carlo method in section 2, we present EMC computations of the backscattering speckle pattern and the backscattering Mueller matrix of an aqueous suspension of polystyrene spheres in a slab geometry in section 3. Special considerations to improve the efficiency of computing the Mueller matrix in the pure backscattering direction are detailed in section 3. We conclude in section 4.

2. Theoretical formalism

Light scattering by small particles is succinctly described by the amplitude scattering matrix[21]. For spherical or randomly-oriented aspheric scatterers, the amplitude scattering matrix is diagonal and depends only on the scattering angle θ due to the symmetry[22]. The parallel and perpendicular components of the electric field with respect to the scattering plane are scattered according to $S_j(\theta)$ where $j = 2, 1$, respectively[21].

The scattering of photons takes a simple form in the local orthonormal coordinate system $(\mathbf{m}, \mathbf{n}, \mathbf{s})$ where \mathbf{m} and \mathbf{n} are the unit vectors in the directions of the parallel and perpendicular components of the electric field with respect to the scattering plane of the previous scattering event and \mathbf{s} is the photon's propagation direction prior to the current scattering [see Fig. 1]. The propagation direction \mathbf{s}' of the photon after the current scattering is given by:

$$\mathbf{s}' = \mathbf{m} \sin \theta \cos \phi + \mathbf{n} \sin \theta \sin \phi + \mathbf{s} \cos \theta \quad (1)$$

where θ and ϕ are the scattering and azimuthal angles of the current scattering respectively.

The current scattering plane is the plane spanned by \mathbf{s} and \mathbf{s}' . The unit vectors in the directions of the parallel and perpendicular electric fields with respect to the current scattering plane are given by

$$\begin{aligned} \mathbf{e}_1 &= \mathbf{m} \cos \phi + \mathbf{n} \sin \phi \\ \mathbf{e}_2 &= -\mathbf{m} \sin \phi + \mathbf{n} \cos \phi \end{aligned} \quad (2)$$

prior to scattering and

$$\mathbf{e}'_1 = \mu \mathbf{m} \cos \phi + \mu \mathbf{n} \sin \phi - \sin \theta \mathbf{s}, \quad (3)$$

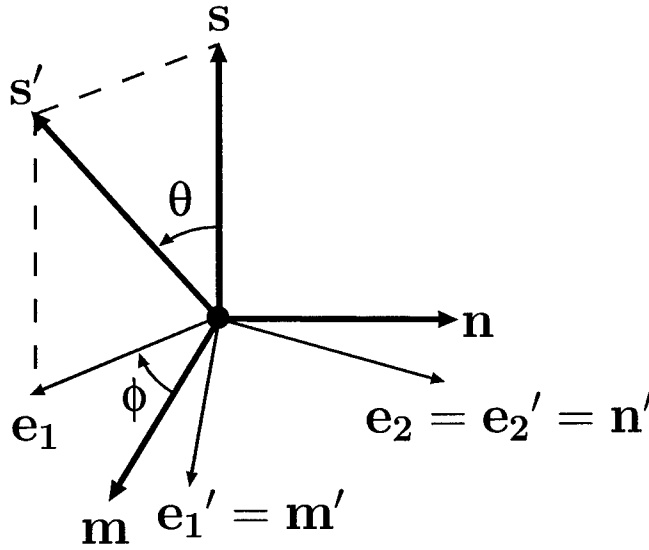


Fig. 1. A photon moving along s is scattered to s' with a scattering angle θ and an azimuthal angle ϕ inside a local coordinate system spanned by orthonormal bases $(\mathbf{m}, \mathbf{n}, \mathbf{s})$. $\mathbf{e}_{1,2}$ and $\mathbf{e}'_{1,2}$ are the unit vectors parallel and perpendicular to the current scattering plane spanned by s and s' prior to and after scattering. The local coordinate system $(\mathbf{m}, \mathbf{n}, \mathbf{s})$ is rotated to $(\mathbf{m}', \mathbf{n}', \mathbf{s}')$ after scattering.

$$\mathbf{e}'_2 = \mathbf{e}_2$$

after scattering, respectively. The local coordinate system $(\mathbf{m}, \mathbf{n}, \mathbf{s})$ is rotated to $(\mathbf{m}', \mathbf{n}', \mathbf{s}')$ whose $\mathbf{m}' = \mathbf{e}'_1$ and $\mathbf{n}' = \mathbf{e}'_2$ after scattering. The incident electric field $\mathbf{E} = E_1 \mathbf{m} + E_2 \mathbf{n}$ is scattered to $\mathbf{E}' = E'_1 \mathbf{m}' + E'_2 \mathbf{n}'$ whose parallel and perpendicular components are given by $E'_1 = S_2 \mathbf{E} \cdot \mathbf{e}_1$ and $E'_2 = S_1 \mathbf{E} \cdot \mathbf{e}_2$, respectively.

We can now summarize the updating rules of the local coordinate system and the electric field in EMC. For each scattering with the scattering angle θ and the azimuthal angle ϕ , the local coordinate system is updated by

$$\begin{pmatrix} \mathbf{m}' \\ \mathbf{n}' \\ \mathbf{s}' \end{pmatrix} = A \begin{pmatrix} \mathbf{m} \\ \mathbf{n} \\ \mathbf{s} \end{pmatrix} \quad (4)$$

with

$$A = \begin{pmatrix} \cos \theta \cos \phi & \cos \theta \sin \phi & -\sin \theta \\ -\sin \phi & \cos \phi & 0 \\ \sin \theta \cos \phi & \sin \theta \sin \phi & \cos \theta \end{pmatrix}, \quad (5)$$

and the electric field by

$$\begin{pmatrix} E'_1 \\ E'_2 \end{pmatrix} = B \begin{pmatrix} E_1 \\ E_2 \end{pmatrix} \quad (6)$$

with

$$B = [F(\theta, \phi)]^{-1/2} \begin{pmatrix} S_2 \cos \phi & S_2 \sin \phi \\ -S_1 \sin \phi & S_1 \cos \phi \end{pmatrix}. \quad (7)$$

We have introduced an extra factor $F(\theta, \phi)$, the scattered wave intensity propagating along the (θ, ϕ) direction, given by

$$F(\theta, \phi) = \left(|S_2|^2 \cos^2 \phi + |S_1|^2 \sin^2 \phi \right) |E_1|^2 + \left(|S_2|^2 \sin^2 \phi + |S_1|^2 \cos^2 \phi \right) |E_2|^2 + 2 \left(|S_2|^2 - |S_1|^2 \right) \cos \phi \sin \phi \Re [E_1 (E_2)^*] \quad (8)$$

to normalize the light intensity. The intensity of the incident light $|E_1|^2 + |E_2|^2 = 1$ is assumed unity in Eq. (8). The scattered light intensity $|E_1'|^2 + |E_2'|^2$ is then conserved (equal to unity) in the series of scattering events. Absorption of light, if any, is accounted for by adjusting the photon weight as in the conventional Monte Carlo simulations[23].

The orthogonal matrix A rotates the local coordinate system $(\mathbf{m}, \mathbf{n}, \mathbf{s})$ each time the photon is scattered by a scatterer. The electric field is updated simultaneously by the matrix B . The free path between consecutive scattering events is sampled in the same fashion as that in a conventional Monte Carlo method. The state of a multiply scattered photon is specified by the final local coordinate system $(\mathbf{m}^{(n)}, \mathbf{n}^{(n)}, \mathbf{s}^{(n)})$ after consecutive rotations, the final complex electric field components $E_{1,2}^{(n)}$ after consecutive updates, and the optical path l inside the host medium where n denotes the number of scattering events the photon have experienced before being detected. The detected electric field is given by $\mathbf{E}_d = [E_1^{(n)} \mathbf{m}^{(n)} + E_2^{(n)} \mathbf{n}^{(n)}] \exp(ikl)$ where $k = 2\pi/\lambda$ is the wave number, λ is the wavelength of light in the host medium, and we have assumed a convention that the temporal dependence of a plane wave of frequency ω is $\exp(-i\omega t)$. The phase of the detected photon accrues from phase delays due to the interaction of light with scatterers and propagation through the host medium. The photon weight w , unity at incidence, is multiplied by the albedo of the scatterer at each scattering event. Once the photon hits a detector, the electric field at the detector is increased by $w^{1/2} \mathbf{E}_d$ and the Stokes vector is increased by the Stokes vector computed from the electric field $w^{1/2} \mathbf{E}_d$.

Propagation of multiply scattered light is describable by the radiative transport equation in which any interference effects are neglected[5]. The conventional Monte Carlo methods based on tracing the Stokes vector of light solve the radiative transfer equation numerically and do not include any correlation effect of multiply scattered light. By tracing the electric field associated with a wave packet, EMC provides much more detailed information about the propagation of multiply scattered light than just the transfer of energy. EMC should be regarded as a method to sample the probability distribution of the electric field at selected spatial positions where the detectors are located. Detectors of finer resolution than the speckle size are required to resolve the interference pattern of light well. Detectors of a larger cell size will smear the interference pattern. It should be noted that EMC only probes one instantaneous picture of the disordered medium when accumulating the electric field coherently while it yields the detected light ensemble averaged over all pictures of the disordered medium when accumulating the Stokes vector incoherently. This point is addressed in more detail in section 3.1.

One key step in the Monte Carlo simulation of polarized light is the sampling of the scattering angles (θ, ϕ) which distribute according to the normalized phase function $p(\theta, \phi) = F(\theta, \phi)/\pi Q_{\text{sca}} x^2$ where Q_{sca} is the scattering efficiency, $x = ka$ is the size parameter, and a is the radius of the particle. The rejection technique[24, 25] has been widely used to sample such a distribution function. The procedure is to choose a doublet $(\mu \equiv \cos \theta, \phi)$ where μ and ϕ are uniformly distributed over $[-1, 1]$ and $[0, 2\pi]$ respectively and a random number f uni-

formly distributed over $[0, \max_{\theta, \phi} p(\theta, \phi)]$, the doublet (μ, ϕ) is accepted as the scattering and azimuthal angles if $f < p(\arccos \mu, \phi)$, otherwise generate a new doublet (μ, ϕ) , a new f and start over. Each trial involves one Mie calculation of the amplitude scattering matrix at that trial scattering angle. The number of rejections per scattering event is large (on the order of one for Rayleigh particles and can be much more significant for larger particles). This limits the efficiency of the Monte Carlo simulation. Mie calculations of the amplitude scattering matrix are hence usually performed on a fixed set of scattering angles in advance to generate a table of scattering matrices and reduce the computation load.

We generate the scattering angle θ by drawing of one random number uniformly distributed over $[0, 1]$ and looking up an inverse table of the marginal distribution function

$$p(\theta) = \int_0^{2\pi} p(\theta, \phi) d\phi = \frac{|S_2|^2 + |S_1|^2}{Q_{\text{sca}} x^2} \quad (9)$$

which does not depend on the electric field and is pre-calculated before simulation. The azimuthal angle ϕ is then obtained by the rejection method for the conditional probability $p(\phi|\theta) = p(\theta, \phi)/p(\theta)$. One Mie calculation for the looked up scattering angle is required if the table of scattering matrices is not generated in advance for each scattering event.

A different sampling strategy is to sample the scattering angle θ according to $p(\theta)$ while to sample ϕ uniformly distributed over $[0, 2\pi]$. At the same time, we modify $F(\theta, \phi)$ in the update rule of the electric field (6) to $F'(\theta) = (|S_2|^2 + |S_1|^2)/2$ such that the light intensity is no longer conserved in the series of scattering events. This strategy saves the rejection sampling of the angle ϕ but the simulation result is prone to be contaminated by hotspots and has a larger variance compared to the first strategy because it is unfavorable to the statistical variance when photons of varying weights, rather than equal weights, are accumulated by the detector. The second sampling strategy is not used in simulation.

3. Results and Discussion

3.1. Backscattering speckle pattern

Due to the large ratio between the velocities of light and of the scatterers, coherent light probes an instantaneous picture of the disordered medium and realizes speckle patterns when the multiple scattered light emerges from within the medium. The $\alpha = x, y, z$ component of the outgoing light intensity $I_\alpha(\theta, \phi)$ in direction (θ, ϕ) on the boundary of the medium comprises a multitude of independently-phased additive complex electric fields in that direction (outside the coherent backscattering cone[26–28]) and follows a Rayleigh distribution[29] $p(I_\alpha) = \frac{1}{\langle I_\alpha \rangle} \exp(-I_\alpha/\langle I_\alpha \rangle)$ where $\langle I_\alpha \rangle$ is the mean intensity. The normalized light intensity $\eta = I_\alpha/\langle I_\alpha \rangle$ follows the exponential distribution $\exp(-\eta)$.

We perform EMC to study the plane wave light backscattering from an aqueous solution of polystyrene spheres inside a slab. Incident light is polarized in the x direction and propagates in the z direction (normal to the surface of the slab). The size of the polystyrene sphere is $0.46\mu\text{m}$. The wavelength of the incident wave is $\lambda_{\text{vac}} = 0.52\mu\text{m}$ in vacuum. The refractive indices of the polystyrene sphere and water is $n_{\text{sct}} = 1.59$ and $n_{\text{bg}} = 1.33$, respectively. The mean scattering length of light inside the solution is $l_s = 2.80\mu\text{m}$ with $2\pi n_{\text{bg}} l_s / \lambda_{\text{vac}} = 45$. The thickness of the slab is $L_z = 4l_s$. Total 5×10^8 photons are launched into the medium. Both backscattering electric field and Stokes vector are recorded versus the direction (θ, ϕ) of the backscattered light where θ is the angle away from the surface normal ($0 \leq \theta \leq \pi/2$) and ϕ is the azimuthal angle ($0 \leq \phi \leq 2\pi$). The ranges of the angles θ and ϕ are uniformly divided into 1125 and 360 bins in simulation, respectively.

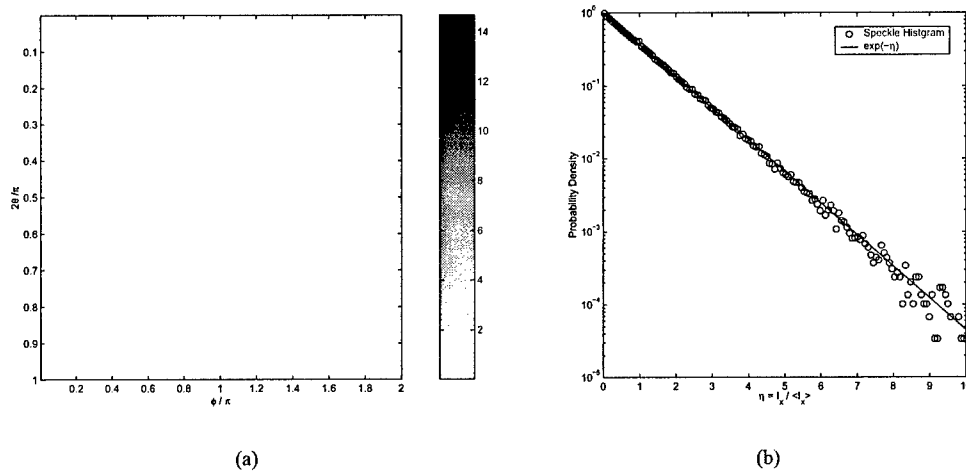


Fig. 2. (a) Speckle pattern formed by the angular-resolved backscattering light. (b) Normalized speckle $I_x / \langle I_x \rangle$ follows a negative exponential distribution.

EMC, like an experiment probing one static random medium, only probes one instantaneous picture of the disordered medium. The ensemble average is realized in experiments, for example, through the movement of the scatterers in the medium or sampling different regions of the random media. EMC, as a numerical experiment, can record both the electric field and the Stokes vectors in simulation. The recorded electric field added coherently yields the emergent light from the one instantaneous picture of the disordered medium. The recorded Stokes vector added incoherently, on the other hand, yields the emergent light ensemble averaged over all pictures of the disordered medium.

Figure 2(a) displays the x component $I_x / \langle I_x \rangle$ where $I_x = |E_x|^2$ and $\langle I_x \rangle$ is estimated by the mean of the first and second Stokes vectors. The appearance of speckles is obvious in Fig. 2(a). The first order statistics about $I_x / \langle I_x \rangle$ can be computed from its histogram. This yields a negative exponential distribution $\exp(-\eta)$ as expected [see Fig. 2(b)]. The other two y and z components of light behave similarly and not displayed.

3.2. Backscattering Mueller matrix

We then compute the backscattering Mueller matrix from a pencil beam incident normally on an aqueous solution of polystyrene spheres inside a slab. The size of the polystyrene sphere is $2\mu\text{m}$. The wavelength of the incident wave is $\lambda_{\text{vac}} = 0.63\mu\text{m}$ in vacuum. The refractive indices of the polystyrene sphere and water is $n_{\text{scl}} = 1.59$ and $n_{\text{bg}} = 1.33$, respectively. The thickness of the slab is $L_z = 4l_s$. Total 3×10^8 photons are launched into the medium.

To improve its efficiency of the Monte Carlo simulation, we combined symmetry considerations[19], randomly polarized incident light[17] and the next event point estimator[17] in computing the backscattering Mueller matrix. The computation time is less than 2 hours for each 10^8 photons launched using one Pentium III 1GHz CPU. In computation of the Stokes vector in Monte Carlo simulations, one should note that the Stokes vector upon which Mueller matrix is defined depends on the reference system used. The backscattered Stokes vector is defined in the reference system whose $x'y'z'$ axes coincide with $-x, y, -z$ axes of the reference

system of the incident Stokes vector respectively.

In the backscattering geometry investigated here where the incident light is normal to the surface of the medium and the outgoing beam is exactly backscattering, the Mueller matrix $M^{bs}(\rho, \phi)$ of the medium shall satisfy the following relation[19, 30]

$$M^{bs}(\rho, \phi) = R(-\phi)M^{bs}(\rho, \phi = 0)R(-\phi) \quad (10)$$

where ρ, ϕ is the polar coordinate of the position of the outgoing beam and $R(\phi)$ is the rotation matrix

$$R(\phi) = \begin{pmatrix} 1 & 0 & 0 & 0 \\ 0 & \cos 2\phi & \sin 2\phi & 0 \\ 0 & -\sin 2\phi & \cos 2\phi & 0 \\ 0 & 0 & 0 & 1 \end{pmatrix}. \quad (11)$$

The reduced Mueller matrix $M_0^{bs}(\rho) \equiv M^{bs}(\rho, \phi = 0)$ relates

$$\mathbf{I}'_o = M_0^{bs}(\rho)\mathbf{I}'_i \quad (12)$$

where $\mathbf{I}'_{i,o}$ are the incident and outgoing Stokes vectors with respect to the $\phi = 0$ plane.

In our simulation, the incident electric field is randomly polarized as $\mathbf{E}_i = \cos \alpha e^{-i\beta} \hat{x} + \sin \alpha e^{i\beta} \hat{y}$ where $\alpha \in (0, \pi/2)$ and $\beta \in (0, \pi)$ are uniform random numbers. The corresponding incident Stokes vector with respect to the xy axes (i.e., the $y = 0$ plane) is $\mathbf{I}_i = (1, \cos 2\alpha, \sin 2\alpha \cos 2\beta, \sin 2\alpha \sin 2\beta)^T$. The incident Stokes vector with respect to the $\phi = 0$ plane is given by $\mathbf{I}'_i = R(\phi)\mathbf{I}_i$. The ensemble average of $\mathbf{I}'_i(\mathbf{I}'_i)^T$ over the random variates α and β yields

$$\langle \mathbf{I}'_i(\mathbf{I}'_i)^T \rangle = R(\phi) \langle \mathbf{I}_i \mathbf{I}_i^T \rangle R(-\phi) = R(\phi) \begin{pmatrix} 1 & 0 & 0 & 0 \\ 0 & 1/2 & 0 & 0 \\ 0 & 0 & 1/4 & 0 \\ 0 & 0 & 0 & 1/4 \end{pmatrix} R(-\phi). \quad (13)$$

Noting that the inverse of the matrix $\langle \mathbf{I}'_i(\mathbf{I}'_i)^T \rangle$ is given by

$$D = [\langle \mathbf{I}'_i(\mathbf{I}'_i)^T \rangle]^{-1} = \begin{pmatrix} 1 & 0 & 0 & 0 \\ 0 & 3 - \cos 4\phi & \sin 4\phi & 0 \\ 0 & \sin 4\phi & 3 + \cos 4\phi & 0 \\ 0 & 0 & 0 & 4 \end{pmatrix}, \quad (14)$$

we obtain

$$M_0^{bs}(\rho) = \mathbf{I}'_o(\mathbf{I}'_i)^T D \quad (15)$$

from Eq. (12). The backscattering Mueller matrix is then computed from the reduced Mueller matrix by Eq. (10).

The computed backscattering Mueller matrix is displayed in Fig. (3). Each matrix element is given as a two-dimensional image of the surface, $20l_s \times 20l_s$ in size, with the laser being incident in the center. The displayed Mueller matrix has been normalized by the maximum light intensity of the (1, 1) element of M^{bs} . Only 7 elements of the Mueller matrix are independent. The symmetrical relation between different elements of the Mueller matrix has been considered by Kattawa et. al.[19, 31]. The symmetry of the backscattering Mueller matrix in Fig. (3) agrees with Kattawa et. al.[13, 19, 31] and Berezhnyy et. al.[32]. The elements M_{14}^{bs} and M_{41}^{bs} vanish as predicted by the theory[13, 19].

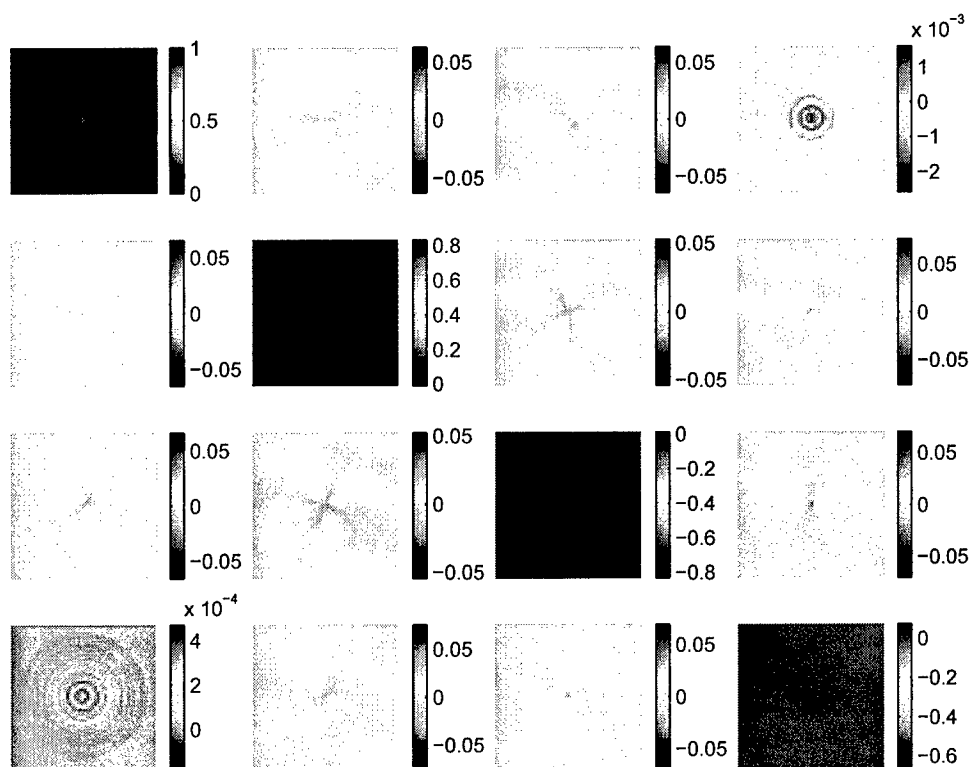


Fig. 3. Backscattering Mueller matrix for the slab. All 4×4 matrix element are displayed as a two-dimensional image of the surface, $20l_s \times 20l_s$ in size, with the laser being incident in the center. The displayed Mueller matrix has been normalized by the maximum light intensity of the $(1, 1)$ element. The parameters of the slab is given in the text.

It is more instructive, though, to display the reduced Mueller matrix $M_0^{bs}(\rho)$. Each element of the reduced Mueller matrix is given as a one-dimensional curve versus the distance ρ from the origin in Fig. (4). The reduced backscattering Mueller matrix is found to be 2×2 block diagonal. The first two elements of the Stokes vector $I'_{1,2}$ are then decoupled from the rest two elements of the Stokes vector $I'_{3,4}$. This means, for example, the backscattered light due to a normally incident light linearly polarized in the $\phi = 0$ plane ($\mathbf{I}'_i = (1, 1, 0, 0)^T$) has no circular polarization component (the fourth element of Stokes vector $\mathbf{I}'_o = M_0^{bs}(\rho)\mathbf{I}'_i$ is always zero) with respect to the $\phi = 0$ plane. The circular polarization component of this backscattered light is no longer zero with respect to a different reference frame rather than the $\phi = 0$ plane.

4. Conclusion

In conclusion, we have presented a Monte Carlo method based on tracing the electric field for simulating polarized light propagation in turbid media. The Electric Field Monte Carlo method has been successfully used to study the backscattering speckle pattern and the backscattering Mueller matrix of an aqueous suspension of polystyrene spheres in a slab geometry. The tracing of the electric field in simulation makes the Electric Field Monte Carlo method possible to simulate also coherent properties of light. The EMC source code will be put in the public

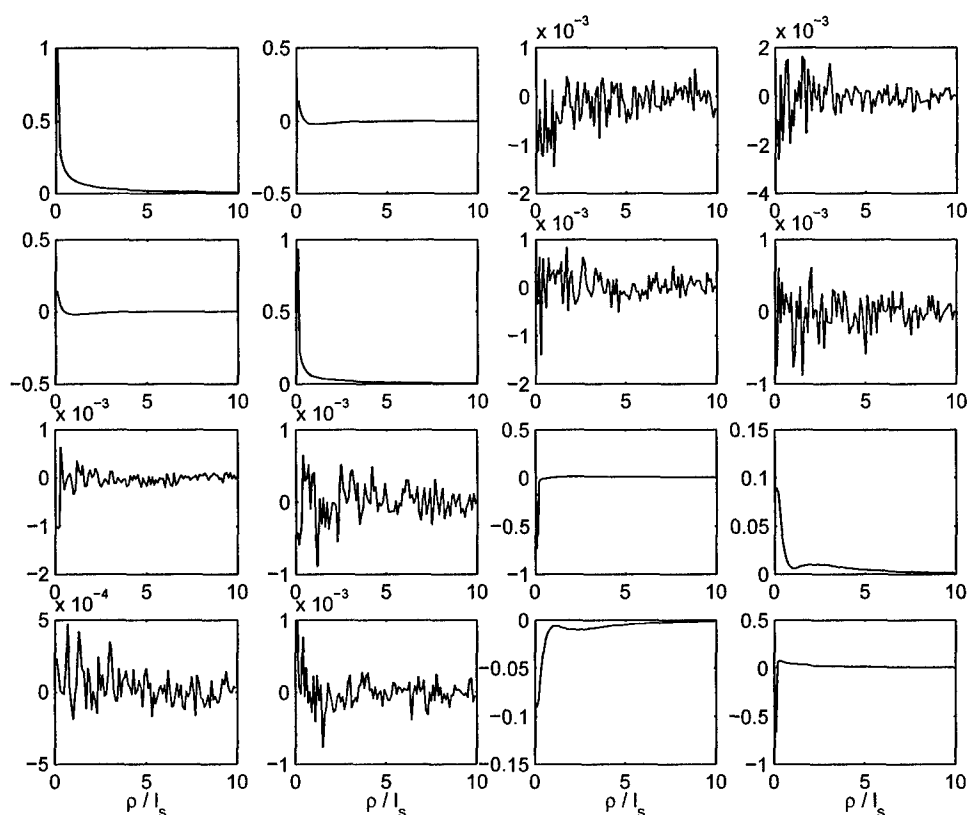


Fig. 4. Reduced backscattering Mueller matrix for the slab. All 4×4 elements of the reduced Mueller matrix is displayed as a one-dimensional curve versus the distance ρ/l_s from the origin. The reduced backscattering Mueller matrix is 2×2 block diagonal.

domain[33].

Acknowledgments

This work is supported in part by US Army Medical Research and Materials Command, ONR and NASA. M. X. thanks the support by the Department of Army (Grant# DAMD17-02-1-0516). The U. S. Army Medical Research Acquisition Activity, 820 Chandler Street, Fort Detrick MD 21702-5014 is the awarding and administering acquisition office. We acknowledge Jessica C Ramella-Roman for sending us her thesis.

Three-dimensional localization and optical imaging of objects in turbid media with independent component analysis

M. Xu, M. Alrubaiee, S. K. Gayen, and R. R. Alfano

A new approach for optical imaging and localization of objects in turbid media that makes use of the independent component analysis (ICA) from information theory is demonstrated. Experimental arrangement realizes a multisource illumination of a turbid medium with embedded objects and a multidetector acquisition of transmitted light on the medium boundary. The resulting spatial diversity and multiple angular observations provide robust data for three-dimensional localization and characterization of absorbing and scattering inhomogeneities embedded in a turbid medium. ICA of the perturbations in the spatial intensity distribution on the medium boundary sorts out the embedded objects, and their locations are obtained from Green's function analysis based on any appropriate light propagation model. Imaging experiments were carried out on two highly scattering samples of thickness approximately 50 times the transport mean-free path of the respective medium. One turbid medium had two embedded absorptive objects, and the other had four scattering objects. An independent component separation of the signal, in conjunction with diffusive photon migration theory, was used to locate the embedded inhomogeneities. In both cases, improved lateral and axial localizations of the objects over the result obtained by use of common photon migration reconstruction algorithms were achieved. The approach is applicable to different medium geometries, can be used with any suitable photon propagation model, and is amenable to near-real-time imaging applications. © 2005 Optical Society of America

OCIS codes: 170.7050, 170.5280, 170.3660, 100.3190, 100.3010.

1. Introduction

Optical tomographic imaging of objects in turbid media is an aggressively pursued area of contemporary research that derives impetus from a variety of potential practical applications.^{1–17} Of particular interest are medical applications in which optical tomography and spectroscopy have the potential to provide diagnostic information about tumors in breast and prostate tissue and functional information about brain activities. Simultaneous developments in experimental apparatus and techniques for object interrogation and signal acquisition,^{2,4,5,18,19} analytical models for light propagation,^{10,20–22} and computer al-

gorithms for image reconstruction^{6,8} hold promise for realization of these potentials of optical tomography.

Researchers today use continuous-wave, amplitude-modulated, or ultrashort light pulses to probe the target(s) embedded in the turbid medium and obtain steady-state, frequency-domain, or time-varying optical signals, respectively, by using a variety of detection schemes.^{2,4,5,18,19} Multiple scattering of light in turbid media, such as breast tissue, precludes direct imaging of embedded targets. One then resorts to an inverse image reconstruction (IIR)^{6,8} approach that uses a forward model for light propagation, the measured light intensity distribution on the boundary of the turbid medium, and an inversion algorithm to generate a map of the optical properties, such as the absorption coefficient (μ_a) and the scattering coefficient (μ_s), of the medium and the embedded objects. The objects are desired to appear as localized inhomogeneities in the spatial distribution of these optical coefficients.

The inversion problem is ill posed, and its adequate theoretical treatment is critical to the achievement of a unique solution.⁸ Although three general approaches—Radon-transform-type straight line in-

The authors are with the Department of Physics, the Institute for Ultrafast Spectroscopy and Lasers, New York State Center of Advanced Technology for Ultrafast Photonic Materials and Applications, City College of New York, 136th Street Convent Avenue J419, New York, New York 10031.

Received 14 July 2004; revised manuscript received 24 November 2004; accepted 5 December 2004.

0003-6935/05/101889-09\$15.00/0

© 2005 Optical Society of America

tegrals,²³ modeling of light scattering as a Markov random process,^{24,25} and development and inversions of a partial differential equation (PDE) of diffusion type—are pursued, it is the PDE-based methods that seem more practical in consideration of the signal-to-noise (S/N) ratio of the data and computationally efficient methods available for solution.^{6,8} The commonly used PDE is the diffusion approximation (DA) of the radiative transfer equation (RTE). Both iterative reconstruction and noniterative linearized inversion approaches have been used to solve the inversion problem, which is weakly nonlinear with limited success. The reconstruction of images with adequate spatial resolution and optical contrast and the determination of the location of the inhomogeneities remain formidable tasks. The time required for data acquisition and image reconstruction is another important consideration.

In this article we present a simple and fast approach that employs (for test of concept) continuous-wave transillumination measurements and a novel algorithm based on independent component analysis (ICA)^{26,27} from information theory to locate tumorlike inhomogeneities embedded in breast-simulating turbid media. ICA has been successfully applied in a variety of other applications.^{27–30} We refer to this information-theory-inspired approach as optical tomography that uses independent component analysis, abbreviated as OPTICA. Experimental arrangement for OPTICA realizes a multisource illumination and multidetector signal-acquisition scheme that provides a variety of spatial and angular views that are essential for three-dimensional (3-D) object localization. Multisource illumination is realized in practice by scanning the input surface (or source plane) across the incident beam in a two-dimensional (2-D) array of points $(x_{sk}, y_{sk}; k = 1, 2, \dots, n)$. Corresponding to illumination of the k th grid point on the source plane, a charge-coupled device (CCD) camera records the spatial intensity distribution, $I_k(x_d, y_d)$, on the exit surface (or detector plane). Every pixel of the CCD camera thus acts as a detector implementing the multidetector measurement arrangement. The difference, $\Delta I_k(x_d, y_d)$, between the above-mentioned spatial intensity distribution, $I_k(x_d, y_d)$, and an estimated background (say, an averaged intensity distribution from different source scanning positions) provides the perturbation in the spatial intensity distribution in the detector plane for illumination at the k th grid point.

The localization algorithm is based on the premise that each object (or inhomogeneity) within the turbid medium alters the propagation of light through the medium. Consequently, the spatial distribution of the light intensity at the detector plane of the medium is different with embedded inhomogeneities than that without them. The influence of an object on $\Delta I_k(x_d, y_d)$ involves propagation of light from the source to the object, and from the object to the detector, and can be described in terms of two Green's functions (propagators): The first $G(\mathbf{r}, \mathbf{r}_s)$ describes light propagation from the source at \mathbf{r}_s to the object at \mathbf{r} , and the second

$G(\mathbf{r}_d, \mathbf{r})$ describes that from the object to the detector at \mathbf{r}_d . To correlate the perturbations in the light intensity distributions, $\Delta I_k(x_d, y_d)$, with the objects embedded in the turbid medium, we assumed that these objects illuminated by the incident wave are *virtual sources* and that $\Delta I_k(x_d, y_d)$ are taken to be some weighted mixtures of signals arriving from these virtual sources to the detector plane. ICA assumes these virtual sources to be *independent*, and based on that assumption it provides the independent components. The number of leading independent components is the same as the number of the embedded objects. The effective contributions of independent components to the light intensity distribution on the source and detector planes are proportional to the projection of the Green's function, $G(\mathbf{r}, \mathbf{r}_s)$ and $G(\mathbf{r}_d, \mathbf{r})$, on the source and detector planes, respectively. The location and characteristics of the objects are obtained from fitting *either* or *both* of these projections to those of the model Green's function in the background medium.

The remainder of the article is organized as follows. In Section 2, we present the general theoretical framework for OPTICA and then discuss the specific case of a turbid medium in the form of a slab. However, the approach can be adapted to any arbitrary geometry. Scattering and absorbing objects are considered separately. Section 3 presents the experimental methods, materials, and parameters. The results are presented in Section 4. Finally, the implications of these results and the scope of OPTICA are discussed in Section 5.

2. Theoretical Formalism

In the linearized scheme of inversion, the perturbation of the detected light intensities on the boundaries of the medium (the scattered wave field) due to absorptive and scattering objects (inhomogeneities) is given by^{3,13}

$$\begin{aligned} \phi_{\text{sca}}(\mathbf{r}_d, \mathbf{r}_s) = & - \int G(\mathbf{r}_d, \mathbf{r}) \delta \mu_a(\mathbf{r}) c G(\mathbf{r}, \mathbf{r}_s) d^3 \mathbf{r} \\ & - \int d^3 \mathbf{r} \delta D(\mathbf{r}) c \nabla_r G(\mathbf{r}_d, \mathbf{r}) \cdot \nabla_r G(\mathbf{r}, \mathbf{r}_s) \end{aligned} \quad (1)$$

in the DA (Ref. 31) when illuminated by a unit point source, where \mathbf{r}_s , \mathbf{r} and \mathbf{r}_d are the positions of the source, the inhomogeneity, and the detector, respectively; $\delta \mu_a = \mu_{a,\text{obj}} - \mu_a$ and $\delta D = D_{\text{obj}} - D$ are the differences in the absorption coefficient and the diffusion coefficient, respectively, between the inhomogeneity and the background; c is the speed of light in the medium; and $G(\mathbf{r}, \mathbf{r}')$ is the Green's function describing light propagation from \mathbf{r}' to \mathbf{r} inside the background turbid medium of the absorption and diffusion coefficients μ_a and D , respectively. We do not explicitly include the modulation frequency ω of

the incident wave in the arguments of Eq. (1) for clarity. The following formalism can be applied to continuous-wave, frequency-domain, and time-resolved measurements. The time-domain measurement is first Fourier transformed over time to obtain data over many different frequencies. Although Eq. (1) starts with DA, it should be emphasized that the formalism is not limited to DA, but can be used with other models of light propagation in turbid media, such as the cumulant approximation,^{20,22,32} the random-walk model,^{10,24} and radiative transfer^{17,33} when they are linearized.

The Green's function G for a slab geometry in the diffusion approximation is given by

$$G(\mathbf{r}, \mathbf{r}') = G(\rho, z, z') = \frac{1}{4\pi D} \sum_{k=-\infty}^{\infty} \left[\frac{\exp(-\kappa r_k^+)}{r_k^+} - \frac{\exp(-\kappa r_k^-)}{r_k^-} \right], \quad (2)$$

$$r_k^{\pm} = [\rho^2 + (z \mp z' \pm 2kd)^2]^{1/2}$$

for an incident amplitude-modulated wave of modulation frequency ω , where $k = 0, \pm 1, \pm 2, \dots$, $\rho = [x - x']^2 + [y - y']^2]^{1/2}$ is the distance between the two points $\mathbf{r} = (x, y, z)$ and $\mathbf{r}' = (x', y', z')$ projected onto the xy plane, $\kappa = [(\mu_a - i\omega/c)/D]^{1/2}$ chosen to have a nonnegative real part, and the extrapolated boundaries of the slab are located at $z = 0$ and $z = d = L_z + 2z_e$, respectively, where L_z is the physical thickness of the slab and the extrapolation length z_e should be determined from the boundary condition of the slab.³⁴⁻³⁶ Equation (2) serves as the model Green's function for the uniform background medium of a slab geometry. The modulation frequency $\omega = 0$ for continuous-wave light.

In practice, the projections of the Green's function on the source and detector planes are determined from the measured perturbations in the light intensity distribution through independent component analysis. The comparison with the Green's function computed with Eq. (2) is then used to locate and characterize the inhomogeneities. We develop the formalism for absorptive and scattering inhomogeneities in the Subsections 2.A and 2.B, respectively.

A. Absorptive Inhomogeneity

The assumption that absorptive inhomogeneities are localized [that is, the j th one is contained in volume V_j centered at \mathbf{r}_j ($1 \leq j \leq J$)] enables one to rewrite the scattered wave field in Eq. (1) as

$$-\phi_{\text{sca}}(\mathbf{r}_d, \mathbf{r}_s) = \sum_{j=1}^J G(\mathbf{r}_d, \mathbf{r}_j) q_j G(\mathbf{r}_j, \mathbf{r}_s), \quad (3)$$

where $q_j = \delta\mu_a(\mathbf{r}_j)cV_j$ is the absorption strength of the j th inhomogeneity. The scattered wave may be interpreted as an instantaneous linear mixture³⁷

$$\mathbf{x}(\mathbf{r}_s) = A\mathbf{s}(\mathbf{r}_s). \quad (4)$$

Here $\mathbf{s}(\mathbf{r}_s) = [q_1 G(\mathbf{r}_1, \mathbf{r}_s), \dots, q_J G(\mathbf{r}_J, \mathbf{r}_s)]^T$ represents the J virtual sources; i.e., the J inhomogeneities illuminated by the incident wave, A is the mixing matrix given by

$$A = \begin{bmatrix} G(\mathbf{r}_{d_1}, \mathbf{r}_1) & G(\mathbf{r}_{d_1}, \mathbf{r}_2) & \dots & G(\mathbf{r}_{d_1}, \mathbf{r}_J) \\ G(\mathbf{r}_{d_2}, \mathbf{r}_1) & G(\mathbf{r}_{d_2}, \mathbf{r}_2) & \dots & G(\mathbf{r}_{d_2}, \mathbf{r}_J) \\ \vdots & \vdots & \ddots & \vdots \\ G(\mathbf{r}_{d_m}, \mathbf{r}_1) & G(\mathbf{r}_{d_m}, \mathbf{r}_2) & \dots & G(\mathbf{r}_{d_m}, \mathbf{r}_J) \end{bmatrix}, \quad (5)$$

whose j th column (mixing vector) provides the weight factors for the contributions from the j th inhomogeneity to the detectors, and $\mathbf{x}(\mathbf{r}_s) = [-\phi_{\text{sca}}(\mathbf{r}_{d_1}, \mathbf{r}_s), \dots, -\phi_{\text{sca}}(\mathbf{r}_{d_m}, \mathbf{r}_s)]^T$ is the observed light intensity change. The superscript T denotes light intensity change. The incident light source scans a total of n positions $\mathbf{r}_{s_1}, \dots, \mathbf{r}_{s_n}$ sequentially. For each source position \mathbf{r}_{s_j} , the observation is made over m positions $\mathbf{r}_{d_1}, \dots, \mathbf{r}_{d_m}$. Each set of such measurement is considered data at one temporal sampling point, as used in the conventional instantaneous linear mixture model.³⁸ The multisource, multidetector data set $\mathbf{x}(\mathbf{r}_s)$ thus describes signals observed in m channels (m detectors) from J virtual sources (or J inhomogeneities) simultaneously over n discrete temporal points (n spatial scanning points). One absorptive inhomogeneity is represented by one virtual source $q_j G(\mathbf{r}_j, \mathbf{r}_s)$. The virtual source $q_j G(\mathbf{r}_j, \mathbf{r}_s)$ represents the individual inhomogeneity illuminated by the incident wave and is similar to the concept of the secondary source in Huygen's principle.³⁹ The role of detectors and sources can be interchanged owing to the reciprocal property of light propagation.

The principal assumption of this formalism is that the virtual source $q_j G(\mathbf{r}_j, \mathbf{r}_s)$ at the j th inhomogeneity is independent of the virtual sources at other locations. Under this assumption, ICA can be used with the observations from the light source scanned at $n \gg J$ positions to separate out both virtual sources $\mathbf{s}(\mathbf{r}_s)$ and the mixing matrix A .^{26,37}

ICA is a statistical approach to separate independent sources from linear instantaneous or convolutive mixtures of independent signals without relying on any specific knowledge of the sources except that they are independent. The sources are recovered by a minimization of a measure of dependence, such as mutual information,^{26,27} between the reconstructed sources.^{30,37} The recovered virtual sources and mixing vectors from ICA are unique up to permutation and scaling.^{30,37}

The two Green's functions of light propagating from the source to the inhomogeneity and from the inhomogeneity to the detector are retrieved from the separated virtual sources $\mathbf{s}(\mathbf{r}_s)$ and the mixing matrix A . The j th element $s_j(\mathbf{r}_s)$ of the virtual source array and the j th column \mathbf{a}_j (mixing vector) of the mixing matrix A provide the scaled projections of the Green's function on the source and detector planes, $G(\mathbf{r}_j, \mathbf{r}_s)$ and $G(\mathbf{r}_d, \mathbf{r}_j)$, respectively. We can write

$$s_j(\mathbf{r}_s) = \alpha_j G(\mathbf{r}_j, \mathbf{r}_s),$$

$$a_j(\mathbf{r}_d) = \beta_j G(\mathbf{r}_d, \mathbf{r}_j), \quad (6)$$

where α_j and β_j are scaling constants for the j th inhomogeneity.

Both the location and the strength of the j th object can be computed by a simple fitting procedure by use of Eq. (6). We adopted a least-square fitting procedure given by

$$\min_{\mathbf{r}_j, \alpha_j, \beta_j} \left\{ \sum_{\mathbf{r}_s} [\alpha_j^{-1} s_j(\mathbf{r}_s) - G(\mathbf{r}_j, \mathbf{r}_s)]^2 + \sum_{\mathbf{r}_d} [\beta_j^{-1} a_j(\mathbf{r}_d) - G(\mathbf{r}_d, \mathbf{r}_j)]^2 \right\}. \quad (7)$$

The fitting yields the location \mathbf{r}_j of and the two scaling constants α_j and β_j for the j th inhomogeneity, whose absorption strength is then given by $q_j = \alpha_j \beta_j$.

B. Scattering Inhomogeneity

For scattering inhomogeneities, under the assumption that the inhomogeneities are localized in a few regions, the same analysis can be carried out as that for absorptive inhomogeneities. The only modification is that up to three virtual sources may appear for one scattering inhomogeneity corresponding to the x, y, z components in the dot product $\nabla_{\mathbf{r}} G(\mathbf{r}_d, \mathbf{r}) \cdot \nabla_{\mathbf{r}} G(\mathbf{r}, \mathbf{r}_s) = \partial_x G(\mathbf{r}_d, \mathbf{r}) \partial_x G(\mathbf{r}, \mathbf{r}_s) + \partial_y G(\mathbf{r}_d, \mathbf{r}) \partial_y G(\mathbf{r}, \mathbf{r}_s) + \partial_z G(\mathbf{r}_d, \mathbf{r}) \partial_z G(\mathbf{r}, \mathbf{r}_s)$ in Eq. (1).

Introducing two auxiliary functions

$$g_{\perp}(\mathbf{r}, \mathbf{r}') = \frac{1}{4\pi D} \sum_{k=-\infty}^{+\infty} \left[(\kappa r_k^+ + 1) \frac{\exp(-\kappa r_k^+)}{(r_k^+)^3} - (\kappa r_k^- + 1) \frac{\exp(-\kappa r_k^-)}{(r_k^-)^3} \right], \quad (8)$$

$$g_z(\mathbf{r}, \mathbf{r}') = \frac{1}{4\pi D} \sum_{k=-\infty}^{+\infty} \left\{ (z - z' + 2kd)(\kappa r_k^+ + 1) \frac{\exp(-\kappa r_k^+)}{(r_k^+)^3} - (z + z' - 2kd) \times (\kappa r_k^- + 1) \frac{\exp(-\kappa r_k^-)}{(r_k^-)^3} \right\}, \quad (9)$$

and the scattered wave due to scattering inhomogeneities can be rewritten as

$$\phi_{\text{sca}}(\mathbf{r}_d, \mathbf{r}_s) = - \int d^3 \mathbf{r} \delta D(\mathbf{r}) c \{ [(x - x_d)(x - x_s) + (y - y_d)(y - y_s)] g_{\perp}(\mathbf{r}, \mathbf{r}_d) g_{\perp}(\mathbf{r}, \mathbf{r}_s) + g_z(\mathbf{r}, \mathbf{r}_d) g_z(\mathbf{r}, \mathbf{r}_s) \}. \quad (10)$$

Denoting the scattering inhomogeneities as $q_j' = \delta D(\mathbf{r}_j) c V_j'$, where c is the speed of light in the

medium, and V_j' is the volume of the j th scattering inhomogeneity, the scattered wave field can be transformed to

$$\begin{aligned} -\phi_{\text{sca}}(\mathbf{r}_d, \mathbf{r}_s) = & \sum_{j=1}^{J'} g_z(\mathbf{r}_j, \mathbf{r}_d) q_j' g_z(\mathbf{r}_j, \mathbf{r}_s) + \sum_{j=1}^{J'} \rho_{dj} \\ & \times \cos \theta_d g_{\perp}(\mathbf{r}_j, \mathbf{r}_d) q_j' \rho_{sj} \cos \theta_s g_{\perp}(\mathbf{r}_j, \mathbf{r}_s) \\ & + \sum_{j=1}^{J'} \rho_{dj} \sin \theta_d g_{\perp}(\mathbf{r}_j, \mathbf{r}_d) q_j' \rho_{sj} \\ & \times \sin \theta_s g_{\perp}(\mathbf{r}_j, \mathbf{r}_s), \end{aligned} \quad (11)$$

where $\rho_{dj} = [(x_d - x_j)^2 + (y_d - y_j)^2]^{1/2}$, $\rho_{sj} = [(x_s - x_j)^2 + (y_s - y_j)^2]^{1/2}$, and θ_d and θ_s are the azimuthal angles of $\mathbf{r}_d - \mathbf{r}_j$ and $\mathbf{r}_s - \mathbf{r}_j$, respectively. This scattered wave can be regarded as a mixture of contributions from $(3J')$ virtual sources:

$$q_j' g_z(\mathbf{r}_j, \mathbf{r}_s), \quad q_j' \rho_{sj} \cos \theta_s g_{\perp}(\mathbf{r}_j, \mathbf{r}_s), \\ q_j' \rho_{sj} \sin \theta_s g_{\perp}(\mathbf{r}_j, \mathbf{r}_s), \quad (12)$$

with mixing vectors

$$g_z(\mathbf{r}_j, \mathbf{r}_d), \quad \rho_{dj} \cos \theta_d g_{\perp}(\mathbf{r}_j, \mathbf{r}_d), \quad \rho_{dj} \sin \theta_d g_{\perp}(\mathbf{r}_j, \mathbf{r}_d), \quad (13)$$

where $1 \leq j \leq J'$, respectively. There are in general three virtual sources of specific patterns (one centrosymmetric and two dumbbell shaped) associated with one scattering inhomogeneity, whereas only one centrosymmetric virtual source is associated with one absorptive inhomogeneity. This difference may be used to discriminate absorptive inhomogeneities from scattering inhomogeneities. However, for scattering inhomogeneities deep within turbid media, only the $q_j' g_z(\mathbf{r}_j, \mathbf{r}_s)$ virtual source remains significant and the other two are much diminished. In such a situation, other corroborative evidence, such as multiwavelength measurements, are required to determine the nature of inhomogeneities. Both the location and the strength of the j th scattering object are computed by fitting the retrieved virtual sources and mixing vectors to expressions (12) and (13), respectively.

No specific light propagation model is assumed in ICA. The only assumption is that virtual sources are mutually independent. The number of inhomogeneities within the medium is determined by the number of the independent components presented in the multisource, multidetector data set. The analysis of retrieved independent components from ICA then localizes and characterizes the absorptive and scattering inhomogeneities inside the turbid medium in which an appropriate model of the light propagator is adopted. When the noise level is high or systematic errors are present, or both, extra independent components may appear. Only the leading independent components need to be analyzed to detect and characterize the inhomogeneities of interest, and other components can be discarded.

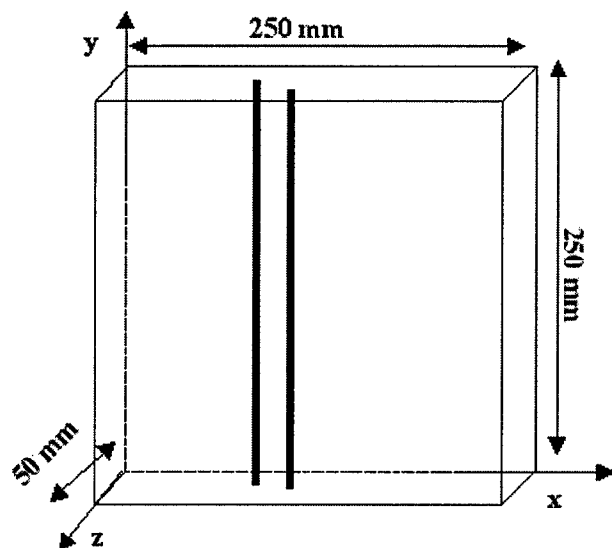


Fig. 1. Schematic diagram of specimen 1 comprising an Intralipid-10% suspension in water with two long cylindrical absorbing objects of absorption coefficient 0.23 mm^{-1} .

3. Experimental Methods and Materials

Two tissue-simulating phantoms with absorption and scattering coefficients within the reported range of values for healthy human breast tissue were used in the study reported here.⁴⁰

The first specimen (1), shown schematically in Fig. 1, was a $250 \text{ mm} \times 250 \text{ mm} \times 50 \text{ mm}$ transparent plastic container filled with Intralipid-10% suspension in water. The concentration of Intralipid-10% was adjusted⁴¹ to provide a transport length $l_t \sim 1 \text{ mm}$ and an absorption coefficient $\mu_a = 0.003 \text{ mm}^{-1}$ at 785 nm , emulating those of human breast tissue. Two cylindrical glass tubes (outer diameter, 8 mm ; inner diameter, 6.98 mm ; and length, 250 mm) were filled with an Intralipid-10% suspension to provide the same scattering coefficient, but the absorption coefficient was changed to 0.023 mm^{-1} by the addition of absorbing ink. The two absorptive rods are placed at $(x, z) = (24, 29) \text{ mm}$ and $(x, z) = (47, 33) \text{ mm}$, respectively, with the axes of cylindrical tubes along y .

The second specimen (2), loaned to us by J. C. Hebden of University College London and displayed schematically in Fig. 2, was a 166-mm-long , 82-mm-wide , and 55-mm-thick slab made of materials with a reduced scattering coefficient $\mu_s' \sim 0.9 \text{ mm}^{-1}$ (transport length, $l_t \sim 1.1 \text{ mm}$) and an absorption coefficient $\mu_a \sim 0.006 \text{ mm}^{-1}$. The slab contained four 5-mm-diameter , 5-mm-long cylindrical inhomogeneities. The center of each cylinder was located in the plane halfway between the front and the back faces of the slabs. The absorption coefficient of each cylinder was 0.006 mm^{-1} , the same as that of the material of the slab, but the scattering coefficients were 4, 2, 1.5, and 1.1 times greater. The first and the third cylinders, and the second and the fourth cylinders, are on two horizontal lines approximately

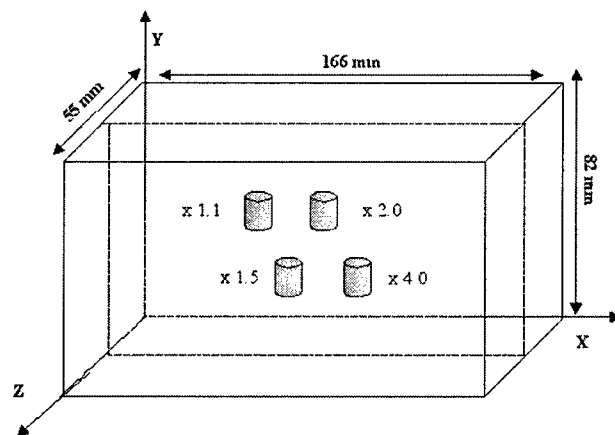


Fig. 2. Schematic diagram of specimen 2 obtained from University College London. It is a solid rectangular block embedded with four 5-mm-diameter and 5-mm-long scattering cylindrical objects with their centers on the central plane. The absorption and scattering characteristics of the specimens and the lateral positions of the four cylinders are described in the text.

22 mm apart. The distance between neighboring cylinders is 11 mm . Further details about the slab may be obtained from an article published by Hall *et al.*⁴²

The experimental arrangement used for imaging of these two specimens (1 and 2) is shown schematically in Fig. 3. For cw measurements, a $200\text{-}\mu\text{m}$ fiber delivered a beam of 784-nm light from a diode laser (Ocean Optics R-2000) to illuminate the input surface (or source plane) of the specimen. A cooled CCD camera set at an acquisition time of 150 ms recorded 2-D intensity patterns of the light transmitted through the opposite side of the slab specimen. For time-resolved measurements, we used a 1-mm-diameter collimated beam of 784-nm , 150-fs , 1-kHz repetition rate light pulses from a Ti:sapphire laser and amplifier system⁴³ for sample illu-

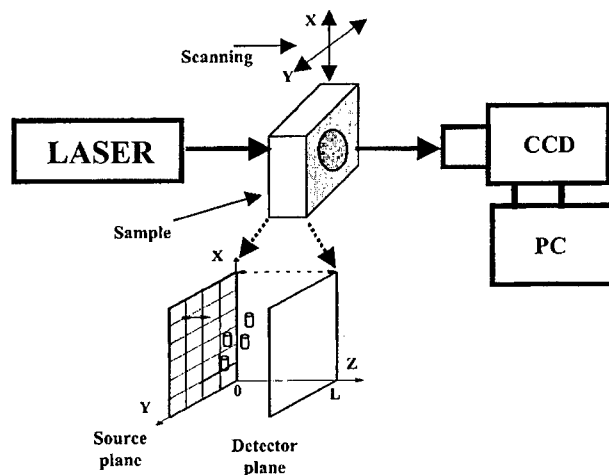


Fig. 3. Schematic diagram of the experimental arrangement for imaging objects embedded in a turbid medium. Inset shows the 2-D array in the input plane that is scanned across the incident laser beam.

mination. An ultrafast gated intensified camera system (UGICS), which provided a FWHM gate width variable from 80 ps to 6 ns, recorded the 2-D intensity patterns of the light transmitted through the opposite side of the slab. Computer-controlled xy translation stages scanned the specimens in an array of points in the xy plane, as displayed in Fig. 3. For the long cylindrical tubes in specimen 1, a line scan of 16 points with a step size of 2.5 mm along the x axis was enough to obtain the (x, z) locations of the absorbing cylinders. An array of 20×18 points with a step size of 2.5 mm across the lateral positions of the four inhomogeneities in specimen 2 was scanned to obtain their locations.

4. Results

Temporal profiles of the transmitted pulses were measured by use of the UGICS in the scan mode with an 80-ps gate width. The average optical properties of the turbid medium were estimated by fitting the temporal profiles to the DA of the RTE for a slab geometry.

ICA of the perturbations in the spatial intensity distributions provided the corresponding independent intensity distributions on the source and detector planes. ICA-generated independent intensity distributions on the source and detector planes are shown in the first and second rows, respectively, of Fig. 4 for the two absorbing cylinders in specimen 1. The locations of the absorbing cylinders are obtained from fitting these independent component intensity distributions to those of the DA in a slab [Eq. (2)]. The first cylinder is found at $x = 24$ mm, 29 mm away from the source plane and 21 mm away from the detector plane. The second cylinder is found at $x = 47$ mm, 33 mm away from the source plane and 17 mm away from the detector plane. The (x, z) coordinates of both the cylinders agree to within 0.5 mm of their known locations. The absorption strengths of the two rods are estimated by use of a least-square fitting procedure [Eq. (7)]. The resolved absorption strengths are $q_1 = 0.152 \text{ mm}^2/\text{ps}$ and $q_2 = 0.132 \text{ mm}^2/\text{ps}$, respectively, for the left and right rods. The values are 88% and 76%, respectively, of the true value of $q = 0.173 \text{ mm}^2/\text{ps}$.

The independent intensity distributions at the detector plane corresponding to the four scattering inhomogeneities in specimen 2 are displayed in Figs. 5(a)–5(d). These independent components are then used to obtain the projections of the inhomogeneity detector Green's function, $G(\mathbf{r}_d, \mathbf{r}_j)$, $j = 1, 2, 3, 4$, on the detector plane for the four small cylindrical scattering inhomogeneities embedded in specimen 2. The locations of the inhomogeneities are determined by fitting the projections to those of the model Green's function. The locations of all four inhomogeneities were obtained. Even the weakest scatterer, with a scattering coefficient just 1.1 times the background and hence considered to be rather unlikely to be found,⁴² was detected. Positions along the z axis (depth) of the cylinders were found to be at 28.1, 27.9, 27.1, and 32.6 mm. Except for the last cylinder, the

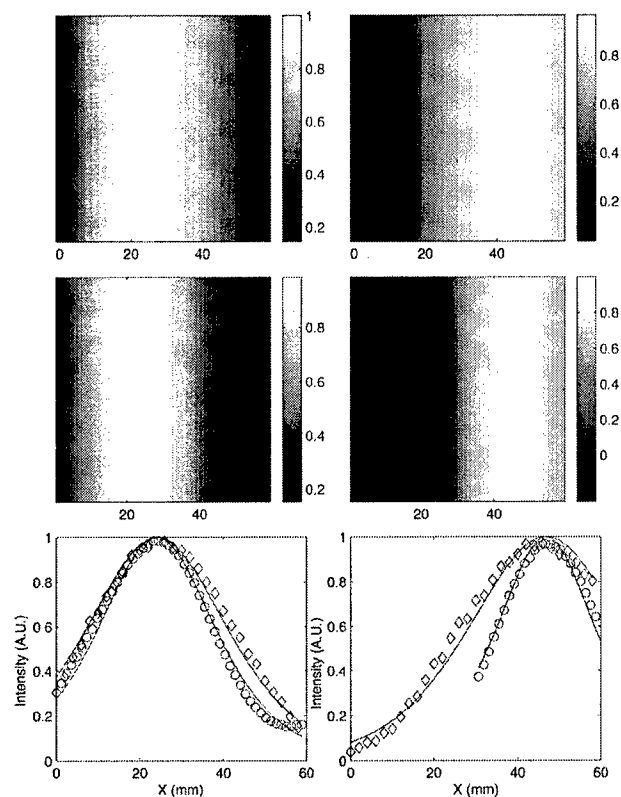


Fig. 4. Normalized independent spatial intensity distributions as a function of the lateral position x at the input (or source) plane (first row) and the exit (or detector) plane (second row) generated by ICA for the two absorbing cylinders in specimen 1. The horizontal profile of the intensity distributions on the source plane (diamond) and on the detector plane (circle) are displayed in the third row. Solid curves show the respective Green's-function fit used for obtaining the locations of the objects.

depth of the cylinders agree well with their known center positions of 27.5 mm. The lateral positions are determined to be (62, 63), (48, 33), (33, 62), and (18, 33) mm for the four scattering cylinders (see Table 1). The strongest and the third-strongest scatterers are on the same horizontal line $y \sim 62$ mm, whereas the second-strongest and the weakest scatterers are on the horizontal line $y \sim 33$ mm with a spacing of 29 mm. The four scatterers are separated by equal spacing, ~ 14 mm in the horizontal direction. The lateral positions agree well with the known (x, y) coordinate values. The uncertainties in location and separation are not greater than 3 mm except for the weakest target.

5. Discussion

The OPTICA presented in this article introduces the information theory technique of ICA to the problem of optical tomographic imaging of objects in turbid media. It is shown to provide object locations accurate to ~ 1 mm in human-breast-like turbid media. It uses multiple-source (realized in this case through scanning of the sample in the xy plane across the incident beam propagating in the z direction) illumination and a multiple-detector (each pixel on the CCD may be

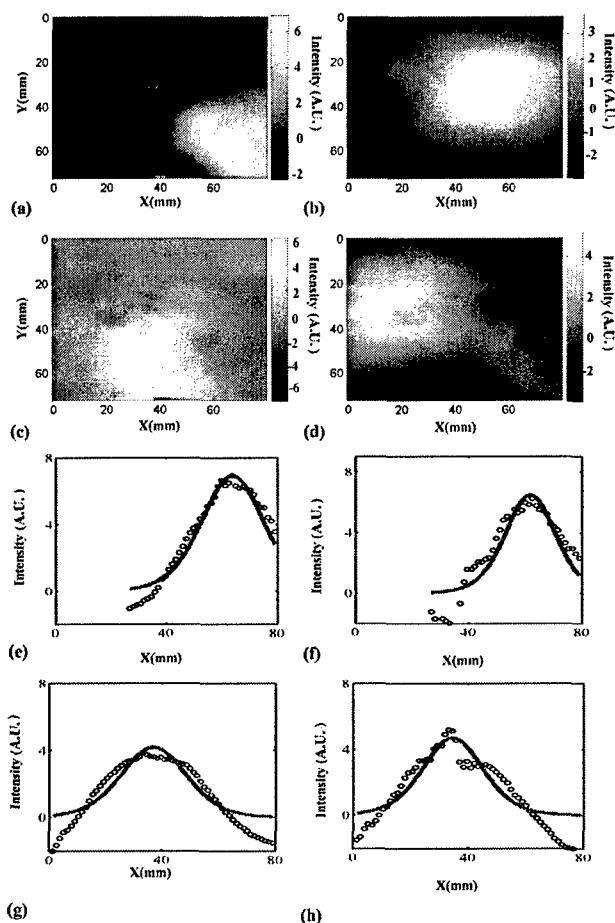


Fig. 5. Independent spatial intensity distributions at the exit (or detector) plane generated by ICA corresponding to objects with scattering coefficients: (a) 4 times, (b) 2 times, (c) 1.5 times, and (d) 1.1 times that of the material of the slab in specimen 2. Horizontal profiles of the intensity distributions in (a)–(d) are shown by circles in (e)–(h), respectively, with solid curves representing the Green's-function fit used for extracting object locations.

viewed as a detector) data-acquisition scheme. The resulting spatial diversity and multiple angular observations provide robust data for extracting 3-D location information about the embedded objects (inhomogeneities) in the medium. A salient feature of OPTICA is that ICA provides the independent components due to the inhomogeneities with minimal

processing of the data and does not have to resort to any specific light propagation model for obtaining this information. Specific light propagation models are needed only in the later stage to determine the location by curve fitting of the Green's functions. OPTICA is not model specific; any appropriate model for light propagation, including the DA and the cumulant solutions of the RTE, may be used. OPTICA can be used with contrast agents such as fluorescence-based optical tomography as well.

Although we used the slab geometry in the study reported in this article, the approach does not depend on any specific geometry. It may be used for other geometries or even an arbitrary-shaped boundary. The approach is fast and is expected to be amenable to near-real-time detection and localization of objects in a turbid medium, which is a key consideration for *in vivo* medical imaging. The approach is remarkably sensitive, considering that it could discern all four cylinders in specimen 2. The approach successfully detected even the lowest-contrast inhomogeneity of the four that had a reduced scattering coefficient only 10% higher than the surrounding medium and was considered improbable to be detected.⁴² OPTICA obtains locations of the objects by fitting *either* or *both* of the Green's functions $G(\mathbf{r}, \mathbf{r}_s)$ and $G(\mathbf{r}_d, \mathbf{r})$, and is suited for physically small inhomogeneities. Given its capability of identifying low-contrast small objects, the approach is expected to be useful for detecting tumors at their early stages of development, a coveted goal in medical imaging.

As demonstrated with specimen 1 and specimen 2, the approach could locate both absorptive and scattering objects. When both absorptive and scattering objects are present in the same turbid specimen, OPTICA can locate them, but their identification as absorbing or scattering entities becomes a more challenging task. As discussed in connection with expressions (12) and (13), each scattering inhomogeneity is expected to be represented by three virtual sources, yielding three pairs of effective intensity distributions each on the detector and source planes. When the background scattering is not severe and the S/N ratio is high, contributions from all three virtual sources may be distinguished and the corresponding object may be identified as a scattering entity. Our simulation results support this assertion. For highly scattering conditions with lower S/N ratios, contributions from the two dumbbell-shaped virtual sources may not be discerned, and corroborative information obtained by other means, such as measurements using light of different wavelengths, are required for identification of the object as an absorptive or scattering entity. Multiwavelength spectroscopic imaging measurements have the potential to provide diagnostic information, such as whether a tumor is malignant or benign.

In summary, OPTICA has the potential to emerge as a new versatile tool for locating targets in turbid media, particularly in diagnostic medical imaging and underwater imaging.

Table 1. Comparison of Known and OPTICA-Determined Positions of the Four Targets^a

Target Number	Target Strength	Known Position (x, y, z) (mm)	OPTICA-Estimated Position (x, y, z) (mm)
1	4	(60, 60, 27.5)	(62, 63, 28.1)
2	2	(47, 30, 27.5)	(48, 33, 27.9)
3	1.5	(33, 60, 27.5)	(33, 62, 27.1)
4	1.1	(20, 30, 27.5)	(18, 33, 32.6)

^aTarget strength is the ratio of the scattering coefficients of the target to that of the surrounding medium. The errors in location are not greater than 3 mm.

This study is supported in part by the U.S. Army Medical Research and Materials Command, Office of Naval Research, New York State Office of Science, Technology and Academic Research, and City University of New York organized research programs. M. Xu acknowledges the support by the Department of Army (grant DAMD17-02-1-0516). M. Alrubaiee thanks the National Science Foundation for an Advance Placement Fellowship. We acknowledge J. C. Hebden of University College London for the loan of specimen 2 and W. Cai for helpful discussions.

References

- G. Muller, R. R. Alfano, S. R. Arridge, J. Beuthan, E. Gratton, M. Kaschke, B. R. Masters, S. Svanberg, and P. van der Zee, eds., *Medical Optical Tomography: Functional Imaging and Monitoring*, Vol. IS11 of SPIE Institute Series (SPIE, Bellingham, Wash., 1993).
- A. Yodh and B. Chance, "Spectroscopy and imaging with diffusing light," *Phys. Today* **48**, 38–40 (1995).
- M. A. O'Leary, D. A. Boas, B. Chance, and A. G. Yodh, "Experimental images of heterogeneous turbid media by frequency-domain diffusing-photon tomography," *Opt. Lett.* **20**, 426–428 (1995).
- S. K. Gayen and R. R. Alfano, "Emerging optical biomedical imaging techniques," *Opt. Photon. News* **7**, 17–22 (1996).
- J. C. Hebden, S. R. Arridge, and D. T. Delpy, "Optical imaging in medicine: I. Experimental techniques," *Phys. Med. Biol.* **42**, 825–840 (1997).
- S. R. Arridge and J. C. Hebden, "Optical imaging in medicine: II. Modelling and reconstruction," *Phys. Med. Biol.* **42**, 841–853 (1997).
- W. Cai, S. K. Gayen, M. Xu, M. Zevallos, M. Alrubaiee, M. Lax, and R. R. Alfano, "Optical tomographic image reconstruction from ultrafast time-sliced transmission measurements," *Appl. Opt.* **38**, 4237–4246 (1999).
- S. R. Arridge, "Optical tomography in medical imaging," *Inverse Probl.* **15**, R41–R93 (1999).
- D. Grosenick, H. Wabnitz, H. H. Rinneberg, K. T. Moesta, and P. M. Schlag, "Development of a time-domain optical mammograph and first *in vivo* applications," *Appl. Opt.* **38**, 2927–2943 (1999).
- V. Chernomordik, D. Hattery, A. H. Gandjbakhche, A. Pifferi, P. Taroni, A. Torricelli, G. Valentini, and R. Cubeddu, "Quantification by random walk of the optical parameters of nonlocalized abnormalities embedded within tissuelike phantoms," *Opt. Lett.* **25**, 951–953 (2000).
- V. A. Markel and J. C. Schotland, "Inverse scattering for the diffusion equation with general boundary conditions," *Phys. Rev. E* **64**, 035601 (2001).
- A. H. Hielscher and S. Bartel, "Use of penalty terms in gradient-based iterative reconstruction schemes for optical tomography," *J. Biomed. Opt.* **6**, 183–192 (2001).
- M. Xu, M. Lax, and R. R. Alfano, "Time-resolved Fourier optical diffuse tomography," *J. Opt. Soc. Am. A* **18**, 1535–1542 (2001).
- B. A. Brooksby, H. Dehghani, B. W. Pogue, and K. D. Paulsen, "Near-infrared (NIR) tomography breast image reconstruction with *a priori* structural information from MRI: algorithm development for reconstructing heterogeneities," *IEEE J. Sel. Top. Quantum Electron.* **9**, 199–209 (2003).
- H. Dehghani, B. W. Pogue, S. P. Poplack, and K. D. Paulsen, "Multiwavelength three-dimensional near-infrared tomography of the breast: initial simulation, phantom, and clinical results," *Appl. Opt.* **42**, 135–145 (2003).
- J. C. Hebden, D. A. Boas, J. S. George, and A. J. Durkin, "Topics in biomedical optics: introduction," *Appl. Opt.* **42**, 2869–3329 (2003).
- W. Cai, M. Xu, and R. R. Alfano, "Three dimensional radiative transfer tomography for turbid media," *IEEE J. Sel. Top. Quantum Electron.* **9**, 189–198 (2003).
- L. Wang, P. P. Ho, C. Liu, G. Zhang, and R. R. Alfano, "Ballistic 2-D imaging through scattering walls using an ultrafast optical Kerr gate," *Science* **253**, 769–771 (1991).
- R. R. Alfano, X. Liang, L. Wang, and P. Ho, "Time-resolved imaging of translucent droplets in highly scattering media," *Science* **264**, 1913–1914 (1994).
- W. Cai, M. Lax, and R. R. Alfano, "Analytical solution of the elastic Boltzmann transport equation in an infinite uniform medium using cumulant expansion," *J. Phys. Chem. B* **104**, 3996–4000 (2000).
- W. Cai, M. Lax, and R. R. Alfano, "Analytical solution of the polarized photon transport equation in an infinite uniform medium using cumulant expansion," *Phys. Rev. E* **63**, 016606 (2000).
- M. Xu, W. Cai, M. Lax, and R. R. Alfano, "Photon migration in turbid media using a cumulant approximation to radiative transfer," *Phys. Rev. E* **65**, 066609 (2002).
- F. Natterer, *The Mathematics of Computerized Tomography* (Wiley, New York, 1986).
- A. H. Gandjbakhche, G. H. Weiss, R. F. Bonner, and R. Nossal, "Photon path-length distributions for transmission through optically turbid slabs," *Phys. Rev. E* **48**, 810–818 (1993).
- A. H. Gandjbakhche, V. Chernomordik, J. C. Hebden, and R. Nossal, "Time-dependent contrast functions for quantitative imaging in time-resolved transillumination experiments," *Appl. Opt.* **37**, 1973–1981 (1998).
- P. Comon, "Independent component analysis—a new concept?" *Signal Process.* **36**, 287–314 (1994).
- A. J. Bell, "Information theory, independent component analysis, and applications," in *Unsupervised Adaptive Filtering, Vol. I*, S. Haykin, ed. (Wiley, New York, 2000), pp. 237–264.
- D. Nuzillard and J.-M. Nuzillard, "Application of blind source separation to 1-D and 2-D nuclear magnetic resonance spectroscopy," *IEEE Signal Process. Lett.* **5**, 209–211 (1998).
- R. Vigário, J. Särelä, V. Jousmäki, M. Hämmäläinen, and E. Oja, "Independent component approach to the analysis of EEG and MEG recordings," *IEEE Trans. Biomed. Eng.* **47**, 589–593 (2000).
- A. Hyvärinen, J. Karhunen, and E. Oja, *Independent Component Analysis* (Wiley, New York, 2001).
- P. M. Morse and H. Feshbach, *Methods of Theoretical Physics* (McGraw-Hill, New York, 1953), Vols. I and II.
- M. Xu, W. Cai, M. Lax, and R. R. Alfano, "A photon transport forward model for imaging in turbid media," *Opt. Lett.* **26**, 1066–1068 (2001).
- S. Chandrasekhar, *Radiative Transfer* (Dover, New York, 1960).
- M. Lax, V. Nayaramamurti, and R. C. Fulton, "Classical diffusion photon transport in a slab," in *Laser Optics of Condensed Matter*, J. L. Birman, H. Z. Cummins, and A. A. Kaplyanskii, eds. (Plenum, New York, 1987), pp. 229–237.
- J. X. Zhu, D. J. Pine, and D. A. Weitz, "Internal reflection of diffusive light in random media," *Phys. Rev. A* **44**, 3948–3959 (1991).
- R. C. Haskell, L. O. Svaasand, T.-T. Tsay, T.-C. Feng, M. S. McAdams, and B. J. Tromber, "Boundary conditions for the diffusion equation in radiative transfer," *J. Opt. Soc. Am. A* **11**, 2727–2741 (1994).
- S. Roberts and R. Everson, eds., *Independent Component Analysis: Principles and Practice* (Cambridge U. Press, Cambridge, UK, 2001).
- J.-F. Cardoso, "Blind signal separation: statistical principles," *Proc. IEEE* **86**, 2009–2025 (1998).
- M. V. Klein, *Optics* (Wiley, New York, 1970).
- H. Heusmann, J. Kölzer, and G. Mitic, "Characterization of female breasts *in vivo* by time resolved and spectroscopic mea-

- surements in near infrared spectroscopy," *J. Biomed. Opt.* **1**, 425-434 (1996).
41. H. J. van Staveren, C. J. M. Moes, J. van Marle, S. A. Prahl, and M. J. C. van Gemert, "Light scattering in intralipid-10% in the wavelength range of 400-1100 nm," *Appl. Opt.* **30**, 4507-4514 (1991).
42. D. J. Hall, J. C. Hebden, and D. T. Delpy, "Imaging very-low-contrast objects in breastlike scattering media with a time-resolved method," *Appl. Opt.* **36**, 7270-7276 (1997).
43. Q. Fu, F. Seier, S. K. Gayen, and R. R. Alfano, "High-average-power kilohertz-repetition-rate sub-100-fs Ti:sapphire amplifier system," *Opt. Lett.* **22**, 712-714 (1997).

Optical imaging of turbid media using independent component analysis: Theory and Simulation

M. Xu^{*}, M. Alrubaiee, S. K. Gayen and R. R. Alfano

December 7, 2004

Institute for Ultrafast Spectroscopy and Lasers, New York State Center of Advanced Technology for Ultrafast Photonic Materials and Applications, and Department of Physics, The City College and Graduate Center of City University of New York, New York, NY 10031

Abstract

A new imaging approach for three-dimensional localization and characterization of objects in a turbid medium using independent component analysis (ICA) from information theory is developed and demonstrated using simulated data. This approach uses a multi-source and multi-detector signal acquisition scheme. Independent component analysis of the perturbations in the spatial intensity distribution measured on the medium boundary sorts out the embedded objects. The locations and optical characteristics of the embedded objects are obtained from a Green's function analysis based on any appropriate model for light propagation in the background medium. This approach is shown to locate and characterize absorptive and scattering inhomogeneities within highly scattering medium to a high degree of accuracy. In particular, we show this approach can discriminate between absorptive and scattering inhomogeneities, and can locate and characterize complex inhomogeneities which is both absorptive and scattering. The influence of noise and uncertainty in background absorption or scattering on the performance of this approach is investigated.

Keywords: image processing, image reconstruction, medical imaging, inverse problems, absorption, scattering, diffusion, radiative transfer

Tel: 212-650-6865

Fax: 212-650-5530

Email: minxu@sci.ccny.cuny.edu

Address: J419, Phys. Dept, CCNY; 138th St & Convent Av.; New York, NY 10031

1 Introduction

Optical probing of the interior of multiply scattering colloidal suspensions and biological materials has attracted much attention over the last decade. In particular, biomedical optical tomography and spectroscopy which has the potential to provide functional information about brain activities and diagnostic information about tumors in breast and prostate are being actively pursued[1, 2, 3, 4, 5, 6, 7, 8, 9, 10, 11, 12, 13, 14, 15, 16, 17]. Simultaneous developments in experimental apparatus and techniques for object interrogation and signal acquisition,[4, 5, 2, 18, 19] analytical models for light propagation,[10, 20, 21, 22] and computer algorithms for image reconstruction[8, 6] hold promise for realization of these potentials of optical tomography.

Multiple scattering of light in thick turbid media precludes direct imaging of embedded targets. One typically uses an inverse image reconstruction (IIR)[8, 6] approach to reconstruct a map of the optical properties, such as, absorption coefficient (μ_a) and scattering coefficient (μ_s), of the medium by matching the measured light intensity distribution on the boundary of the turbid medium to that calculated by a forward model for the propagation of light in that medium. The commonly used forward models include the radiative transfer equation (RTE),[23, 17] the diffusion approximation (DA) of RTE,[8, 6] and random walk of photons.[24, 25]

The inversion problem is ill-posed and needs to be regularized to stabilize the inversion at a cost of reduced resolution.[26, 8] Both iterative reconstruction and noniterative linearized inversion approaches have been used to solve the inversion problem in optical tomography, which is weakly nonlinear, with limited success. Reconstruction of images with adequate spatial resolution and accurate localization and characterization of the inhomogeneities remain a formidable task. Time required for data acquisition and image reconstruction is another important consideration.

In this article, we present a novel algorithm based on the independent component analysis (ICA)[27, 28] from information theory to locate absorptive and scattering inhomogeneities embedded in a thick turbid medium and demonstrate the efficacy using simulated data. ICA has been successfully applied in various other application such as electroencephalogram and nuclear magnetic resonance spectroscopy[29, 30, 28, 31] We refer to this information theory-inspired approach as optical imaging using independent component analysis, abbreviated as, OPTICA. The novelty

of OPTICA over other ICA applications is that OPTICA associates directly the independent components to the Green's functions responsible for light propagation in the turbid medium from the inhomogeneities to the source and the detector, and therefore the retrieved independent components can be used to locate and characterize the inhomogeneities.

OPTICA uses a multi-source illumination and multi-detector signal acquisition scheme providing a variety of spatial and angular views essential for three-dimensional (3D) object localization. Each object (or, inhomogeneity) within the turbid medium alters the propagation of light through the medium. The influence of an object on the spatial distribution of the light intensity at the detector plane involves propagation of light from the source to the object, and from the object to the detector, and can be described in terms of two Green's functions (propagators) describing light propagation from source to the object and that from the object to the detector, respectively.

The absorptive or scattering inhomogeneities illuminated by the incident wave are assumed to be *virtual sources*, and the perturbation of the spatial distribution of the light intensity on the medium boundary is taken to be some weighted mixture of signals arriving from these virtual sources. These virtual sources are statistically independent and can be recovered by independent component analysis of the recorded data set. The number of leading independent components is same as the number of embedded objects. The location and characterization of inhomogeneities are obtained from the analysis of the retrieved virtual sources using an appropriate model of light propagation in the background medium.

The remainder of this article is organized as follows. In Section 2, we present a brief introduction to independent component analysis and review the general theoretical framework for OPTICA. Section 3 presents the results from simulations for different configurations. Implications of these results are discussed in Section 4.

2 Theoretical Formalism

2.1 Independent component analysis

Blind source separation is a class of problem of general interest which consists of recovering unobserved signals or virtual sources from several observed mixtures. Typically the observations are the output of a set of sensors, where each sensor receives a different combination of the source signals. Prior knowledge about the mixture in such problems is usually not available. The lack of prior knowledge is compensated by a statistically strong but often physically plausible assumption of independence between the source signals. Over the last decade, independent component analysis (ICA) has been proposed as a solution to the blind source separation problem and emerged as a new paradigm in signal processing and data analysis.[27, 28, 32, 31]

The simplest ICA model, an instantaneous linear mixture model[32], assumes the existence of n independent signals $s_i(t)$ ($i = 1, 2, \dots, n$) and the observation of at least as many mixtures $x_i(t)$ ($i = 1, 2, \dots, m$) by $m \geq n$ sensors, these mixtures being linear and instantaneous, i.e, $x_i(t) = \sum_{j=1}^n a_{ij}s_j(t)$ for each i at a sequence of time t . In a matrix notation,

$$\mathbf{x}(t) = A\mathbf{s}(t), \quad A \in \mathbb{R}^{m \times n} \quad (1)$$

where A is the mixing matrix. The j th column of A gives the mixing vector for the j th virtual source. Independent component analysis can be formulated as the computation of an $n \times m$ separating matrix B whose output

$$\mathbf{y}(t) = B\mathbf{x}(t) = C\mathbf{s}(t), \quad B \in \mathbb{R}^{n \times m}, \quad C \equiv BA \in \mathbb{R}^{n \times n} \quad (2)$$

is an estimate of the vector $\mathbf{s}(t)$ of the source signals.

The basic principle of ICA can be understood in the following way. The central limit theorem in probability theory tells that the distribution of independent random variables tends toward a Gaussian distribution under certain conditions. Thus a sum of multiple independent random variables usually has a distribution that is closer to Gaussian than any of the original random

variables. $y_i(t) = \sum_j C_{ij}s_j(t)$ in Eq. 2, as a summation of independent random variables $s_j(t)$, is usually more Gaussian than $s_j(t)$ while $y_i(t)$ becomes least Gaussian when it in fact equals one of the $s_j(t)$. This heuristic argument shows that independent component analysis can be intuitively regarded as a statistical approach to find the separating matrix B such that $y_i(t)$ is least Gaussian. This can be achieved by maximizing some measure of nongaussianity such as, maximizing kurtosis (the fourth order cumulant), of $y_i(t)$. [33, 32]

Independent component analysis separates independent sources from linear instantaneous or convolutive mixtures of independent signals without relying on any specific knowledge of the sources except that they are independent. The sources are recovered by a maximization of a measure of independence (or, a minimization of a measure of dependence), such as nongaussianity and mutual information between the reconstructed sources. [32, 31] The recovered virtual sources and mixing vectors from ICA are unique up to permutation and scaling. [32, 31]

2.2 Optical imaging using independent component analysis

The classical approach to propagation of multiply scattered light in turbid media, which assumes that phases are uncorrelated on scales larger than the scattering mean free path l_s , leads to the radiative transport equation (RTE) in which any interference effects are neglected. [34] RTE does not admit closed-form analytical solutions in bounded regions and its numerical solution is computational expensive. The commonly used forward models in optical imaging of highly scattering media is the diffusion approximation (DA) to RTE. [8, 6]

The approach OPTICA can be applied to different models of light propagation in turbid media, such as, the diffusion approximation, [8, 6] the cumulant approximation [20, 35, 22], the random walk model, [24, 10] and radiative transfer [34, 17] when they are linearized. The diffusion approximation is valid when the inhomogeneities are deep within a highly scattering medium. We only discuss the formalism of OPTICA in the diffusion approximation in this article.

In the diffusion approximation, the perturbation of the detected light intensities on the boundaries of the medium, the scattered wave field, due to absorptive and scattering objects (inhomo-

geneities) can be written as:[3, 13]

$$\phi_{\text{sca}}(\mathbf{r}_d, \mathbf{r}_s) = - \int G(\mathbf{r}_d, \mathbf{r}) \delta\mu_a(\mathbf{r}) c G(\mathbf{r}, \mathbf{r}_s) d\mathbf{r} - \int \delta D(\mathbf{r}) c \nabla_{\mathbf{r}} G(\mathbf{r}_d, \mathbf{r}) \cdot \nabla_{\mathbf{r}} G(\mathbf{r}, \mathbf{r}_s) d\mathbf{r} \quad (3)$$

to the first order of Born approximation[36] when illuminated by a point source of unit power, where \mathbf{r}_s , \mathbf{r} and \mathbf{r}_d are the positions of the source, the inhomogeneity and the detector respectively, $\delta\mu_a = \mu_{a,\text{obj}} - \mu_a$ and $\delta D = D_{\text{obj}} - D$ are the differences in absorption coefficient and diffusion coefficient, respectively, between the inhomogeneity and the background, c is the speed of light in the medium, and $G(\mathbf{r}, \mathbf{r}')$ is the Green's function describing light propagation from \mathbf{r}' to \mathbf{r} inside the background turbid medium of absorption and diffusion coefficients μ_a and D .

Eq. (3) is written in the frequency domain and does not explicitly show the modulation frequency ω of the incident wave for clarity. The following formalism applies to continuous wave, frequency-domain and time-resolved measurements. The time domain measurement is first Fourier transformed over time to obtain data over many different frequencies.

The Green's function G for a slab geometry in DA is given by

$$G(\mathbf{r}, \mathbf{r}') \equiv G(\rho, z, z') = \frac{1}{4\pi D} \sum_{k=-\infty}^{\infty} \left[\frac{\exp(-\kappa r_k^+)}{r_k^+} - \frac{\exp(-\kappa r_k^-)}{r_k^-} \right] \quad (4)$$

$$r_k^{\pm} = \sqrt{\rho^2 + (z \mp z' \pm 2kd)^2}$$

for an incident amplitude-modulated wave of modulation frequency ω , where $k = 0, \pm 1, \pm 2, \dots$, $\rho = \sqrt{(x - x')^2 + (y - y')^2}$ is the distance between the two points $\mathbf{r} = (x, y, z)$ and $\mathbf{r}' = (x', y', z')$ projected onto the xy plane, $\kappa = \sqrt{(\mu_a - i\omega/c)/D}$ chosen to have a nonnegative real part, and the extrapolated boundaries of the slab are located at $z = 0$ and $z = d = L_z + 2z_e$, respectively, where L_z is the physical thickness of the slab and the extrapolation length z_e should be determined from the boundary condition of the slab.[37, 38, 39] Greens' functions in Eq. (3) for other geometries can be obtained either analytically or numerically.[40, 41]

2.2.1 Absorptive inhomogeneities

We first consider absorptive inhomogeneities. Under the assumption that absorptive inhomogeneities are localized, that is, the j th one is contained in volume V_j centered at \mathbf{r}_j ($1 \leq j \leq J$), the scattered wave field in Eq. (3) can be rewritten as

$$-\phi_{\text{sca}}(\mathbf{r}_d, \mathbf{r}_s) = \sum_{j=1}^J G(\mathbf{r}_d, \mathbf{r}_j) q_j G(\mathbf{r}_j, \mathbf{r}_s) \quad (5)$$

where $q_j = \delta\mu_a(\mathbf{r}_j)cV_j$ is the absorption strength of the j th inhomogeneity. The scattered wave is in a form of in an instantaneous linear mixture (1). One absorptive inhomogeneity is represented by one virtual source $q_j G(\mathbf{r}_j, \mathbf{r}_s)$ with a mixing vector $G(\mathbf{r}_d, \mathbf{r}_j)$.

As the virtual source $q_j G(\mathbf{r}_j, \mathbf{r}_s)$ at the j th inhomogeneity is independent of the virtual sources at other locations, independent component analysis can be used with the observations obtained for the light source at $n \gg J$ different positions to separate out both virtual sources $s_j(\mathbf{r}_s)$ and the mixing vectors $a_j(\mathbf{r}_d)$. [27, 32] The j th virtual source $s_j(\mathbf{r}_s)$ and the j th mixing vector $a_j(\mathbf{r}_d)$ provide the scaled projections of the Green's function on the source and detector planes, $G(\mathbf{r}_j, \mathbf{r}_s)$ and $G(\mathbf{r}_d, \mathbf{r}_j)$, respectively. We can write

$$\begin{aligned} s_j(\mathbf{r}_s) &= \alpha_j G(\mathbf{r}_j, \mathbf{r}_s), \\ a_j(\mathbf{r}_d) &= \beta_j G(\mathbf{r}_d, \mathbf{r}_j) \end{aligned} \quad (6)$$

where α_j and β_j are scaling constants for the j th inhomogeneity.

Both the location and strength of the j th object can be computed by a simple fitting procedure using Eq. (6). We adopted a least square fitting procedure given by:

$$\min_{\mathbf{r}_j, \alpha_j, \beta_j} \left\{ \sum_{\mathbf{r}_s} [\alpha_j^{-1} s_j(\mathbf{r}_s) - G(\mathbf{r}_j, \mathbf{r}_s)]^2 + \sum_{\mathbf{r}_d} [\beta_j^{-1} a_j(\mathbf{r}_d) - G(\mathbf{r}_d, \mathbf{r}_j)]^2 \right\}. \quad (7)$$

The fitting yields the location \mathbf{r}_j of and the two scaling constants α_j and β_j for the j th inhomogeneity whose absorption strength is then given by $q_j = \alpha_j \beta_j$.

2.2.2 Scattering inhomogeneities

For scattering inhomogeneities, a similar analysis shows the scattered wave can be written as:

$$\begin{aligned}
 -\phi_{\text{sca}}(\mathbf{r}_d, \mathbf{r}_s) = & \sum_{j=1}^{J'} g_z(\mathbf{r}_j, \mathbf{r}_d) q'_j g_z(\mathbf{r}_j, \mathbf{r}_s) \\
 & + \sum_{j=1}^{J'} \rho_{dj} \cos \theta_d g_{\perp}(\mathbf{r}_j, \mathbf{r}_d) q'_j \rho_{sj} \cos \theta_s g_{\perp}(\mathbf{r}_j, \mathbf{r}_s) \\
 & + \sum_{j=1}^{J'} \rho_{dj} \sin \theta_d g_{\perp}(\mathbf{r}_j, \mathbf{r}_d) q'_j \rho_{sj} \sin \theta_s g_{\perp}(\mathbf{r}_j, \mathbf{r}_s)
 \end{aligned} \tag{8}$$

where $q'_j = \delta D(\mathbf{r}_j) c V'_j$ is the diffusion strength of the j th scattering inhomogeneity of volume V'_j ($j = 1, 2, \dots, J'$), $\rho_{dj} = \sqrt{(x_d - x_j)^2 + (y_d - y_j)^2}$, $\rho_{sj} = \sqrt{(x_s - x_j)^2 + (y_s - y_j)^2}$, θ_d and θ_s are the azimuthal angles of $\mathbf{r}_d - \mathbf{r}_j$ and $\mathbf{r}_s - \mathbf{r}_j$ respectively, and the two auxiliary functions are given by

$$g_{\perp}(\mathbf{r}, \mathbf{r}') = \frac{1}{4\pi D} \sum_{k=-\infty}^{+\infty} \left[(\kappa r_k^+ + 1) \frac{\exp(-\kappa r_k^+)}{(r_k^+)^3} - (\kappa r_k^- + 1) \frac{\exp(-\kappa r_k^-)}{(r_k^-)^3} \right], \tag{9}$$

and

$$\begin{aligned}
 g_z(\mathbf{r}, \mathbf{r}') = & \frac{1}{4\pi D} \sum_{k=-\infty}^{+\infty} \left\{ (z - z' + 2kd) (\kappa r_k^+ + 1) \frac{\exp(-\kappa r_k^+)}{(r_k^+)^3} \right. \\
 & \left. - (z + z' - 2kd) (\kappa r_k^- + 1) \frac{\exp(-\kappa r_k^-)}{(r_k^-)^3} \right\}.
 \end{aligned} \tag{10}$$

The scattered wave from one scattering inhomogeneity is thus a mixture of contributions from $(3J')$ virtual sources:

$$q'_j g_z(\mathbf{r}_j, \mathbf{r}_s), \quad q'_j \rho_{sj} \cos \theta_s g_{\perp}(\mathbf{r}_j, \mathbf{r}_s), \quad q'_j \rho_{sj} \sin \theta_s g_{\perp}(\mathbf{r}_j, \mathbf{r}_s), \tag{11}$$

with mixing vectors

$$g_z(\mathbf{r}_j, \mathbf{r}_d), \quad \rho_{dj} \cos \theta_d g_{\perp}(\mathbf{r}_j, \mathbf{r}_d), \quad \rho_{dj} \sin \theta_d g_{\perp}(\mathbf{r}_j, \mathbf{r}_d) \tag{12}$$

where $1 \leq j \leq J'$, respectively. Both the location and strength of the j th scattering object are computed by fitting the retrieved virtual sources and mixing vectors to Eq. (11) and Eq. (12) using a least square procedure, respectively.

There are in general three virtual sources of specific patterns (one centrosymmetric and two dumbbell-shaped) associated with one scattering inhomogeneity, whereas only one centrosymmetric virtual source is associated with one absorptive inhomogeneity. This difference may serve as the basis to discriminate absorptive and scattering inhomogeneities.

The only assumption made in OPTICA is that virtual sources are mutually independent. The number of inhomogeneities within the medium is determined by the number of the independent components presented in the multi-source multi-detector data set. No specific light propagation model is assumed in this step. The analysis of retrieved independent components from ICA then localizes and characterizes the absorptive and scattering inhomogeneities inside the turbid medium using an appropriate model of the light propagator. Extra independent components may appear depending on the level of noise in the data. These components can be discarded and only the leading independent components need to be analyzed to detect and characterize inhomogeneities of interest.

3 Results

Simulations were performed for a slab of thickness 50mm shown schematically in Fig. 1. The absorption and diffusion coefficients of the uniform slab is $\mu_a = 1/300\text{mm}^{-1}$ and $D = 1/3\text{mm}$ respectively, close to that of human breast tissue.[42] The incident CW beam scans a set of 21×21 grid points covering an area of $90 \times 90\text{mm}^2$. The spacing between two consecutive grid points is 4.5mm. The light intensity on the other side of the slab is recorded by a CCD camera on 42×42 grid points covering the same area.

[Figure 1 about here.]

In the simulations presented in the following subsections, we fix the ratio of strength of absorption to that of diffusion to be 0.01, which produce perturbations of comparable magnitude on the light

intensities measured on the detector plane from the absorption and scattering inhomogeneities. As the scattered wave is linear with respect to the absorption and diffusion strengths, we also set the strength of either absorption or diffusion to be unity in simulations for convenience.

3.1 Absorptive Inhomogeneities

Two absorptive inhomogeneities, each of a unity absorption strength, are placed at positions (50, 60, 20)mm and (30, 30, 30)mm, respectively. Gaussian noise of 5% was added to the simulated light intensity change on the detector plane. OPTICA operates on a noisy scattering wave $-\phi_{\text{sca}}(\mathbf{r}_d, \mathbf{r}_s)[1 + n(\mathbf{r}_d, \mathbf{r}_s)]$ where $n(\mathbf{r}_d, \mathbf{r}_s)$ is a Gaussian random variable of a standard deviation 0.05.

Independent component analysis of the perturbations in the spatial intensity distributions provided corresponding independent intensity distributions on the source and detector planes. ICA generated independent intensity distributions on the source and detector planes are shown in Fig. 2, for the two absorptive inhomogeneities. Locations of the absorptive objects are obtained from fitting these independent component intensity distributions to those of the diffusion approximation in a slab Eq. (4) by the least square procedure Eq. (7). The first object is found at (50.0, 60.0, 20.0)mm and the second one at (30.0, 30.0, 30.1)mm. The coordinates of both objects agree to within 0.1mm of their known locations. The strengths of the two objects are $q_1 = 1.00$ and $q_2 = 0.99$ respectively, with an error not greater than 1% of the true values.

[Figure 2 about here.]

3.2 Discrimination between absorptive and scattering inhomogeneities

In the second example, one absorptive object of absorption strength of 0.01 is placed at (50, 60, 20)mm and one scattering object of diffusion strength of negative unity (corresponding to an increase in scattering for the inhomogeneity) is placed at (30, 30, 30)mm respectively. 5% Gaussian noise was added to the simulated light intensity change on the detector plane.

Fig. 3 shows the ICA generated independent intensity distributions on the source and detector planes and the least square fitting. The first column corresponds to the absorptive inhomogeneity.

The second through fourth columns correspond to the scattering object which produces one pair of centrosymmetric and two pairs of dumbbell-shaped virtual sources and mixing vectors. The absorptive inhomogeneity is found to be at (50.2, 60.3, 20.2)mm with a strength $q_1 = 0.0101$. The scattering object produces three pairs (one centrosymmetric and two dumbbell-shaped) of virtual sources and mixing vectors centering around the position $(x, y) = (30, 30)$ mm [see the second through fourth columns in Fig. 3]. The dumbbell-shaped virtual source or mixing vector comprises one bright part and its antisymmetric dark counterpart. The resolved position and strength of the scattering object are found to be (30.0, 30.0, 30.0)mm and $q_2 = -0.99$, (32.1, 32.4, 30.2)mm and $q_2 = -0.96$, and (31.3, 30.2, 27.1)mm and $q_2 = -1.05$, respectively, through fitting to the individual pair. For the scattering object, the best result is obtained from the fitting to the first pair of centrosymmetric virtual source and mixing vector from the scattering object. Taking the position and strength of the scattering object to be that from fitting the centrosymmetric virtual source and mixing vector, the error of the resolved positions of both objects is within 0.3mm of their known locations. The error of the resolved strengths of both objects is approximately 1% of the true values.

[Figure 3 about here.]

3.3 Co-located absorptive and scattering inhomogeneities

For one complex inhomogeneity which is both absorptive and scattering, the two pairs of dumbbell-shaped virtual sources and mixing vectors produced by its scattering abnormality can be used to obtain its scattering strength. By subtracting the scattering contribution off the measured scattered wave, our procedure can be applied again to the cleaned data and proceed to obtain its absorption strength. The third example considers a complex inhomogeneity at (30, 30, 20)mm with strengths of absorption $q_1 = 0.01$ and diffusion $q_2 = 1$ (corresponding to a decrease in scattering) respectively. 5% Gaussian noise was added to the simulated light intensity change on the detector plane.

Fig. 4 shows the ICA generated independent intensity distributions on the source and detector planes and the least square fitting. The first and second columns correspond to the pairs of dumbbell-shaped virtual sources and mixing vectors produced by its scattering component. The position and strength of this diffusive component is obtained to be (32.7, 33.0, 20.5)mm and $q_2 = 0.95$,

and (31.7, 30.1, 20.4)mm and $q_2 = 0.96$ by fitting the two individual dumbbell-shaped pair respectively. The position and strength of the diffusive component is found to be (30.9, 30.9, 20.4)mm and $q_2 = 0.95$ if both dumbbell-shaped virtual sources and mixing vectors are used in fitting. The third column of Fig. 4 corresponds to its absorptive component obtained by first removing the scattering contribution from the measured scattered wave. The depth and strength of the absorption component is found to be (30.8, 30.7, 32.7)mm and $q_1 = 0.0091$.

The error in positioning the scattering component is less than 1mm and the error of the resolved strength of the scattering strength is $\sim 5\%$. The errors in positioning and the resolved strength of the absorptive component equal to ~ 3 mm and $\sim 10\%$, respectively, which are larger than those of the scattering component because the error is amplified when the estimated scattering component is used in subtraction off its contribution to the scattered wave in our procedure.

[Figure 4 about here.]

3.4 Effect of noise

To demonstrate the effect of noise on the performance of OPTICA, different levels of Gaussian noise were added to the simulated light intensity change on the detector plane.

Fig. 5 shows the case presented in Fig. 3 of Sec. 3.2 with instead 10% and 20% Gaussian noise added to the scattered wave. The resolved absorptive inhomogeneity is at (50.2, 60.3, 20.1)mm with strength 0.0101 at 10% noise, and at (50.1, 60.3, 20.5)mm with strength 0.0102 at 20% noise. The resolved position and strength of the scattering object are found to be (30.0, 30.1, 30.0)mm and $q_2 = -0.98$, (32.1, 32.4, 30.4)mm and $q_2 = -0.95$, and (31.4, 30.1, 27.5)mm and $q_2 = -1.00$ respectively through fitting to the pair of centrosymmetric and two pairs of dumbbell-shaped virtual sources and mixing vectors [see the second to fourth columns of Fig. 5(a)], respectively, at 10% noise. The resolved values become (28.9, 27.0, 32.9)mm and $q_2 = -0.59$ from fitting the pair of centrosymmetric virtual source and mixing vector [see the second column of Fig. 5(b)], and (30.3, 32.3, 26.6)mm and $q_2 = -1.33$ from fitting the first pair of dumbbell-shaped virtual source and mixing vector [see the third column of Fig. 5(b)], respectively, at 20% noise. The dumbbell-shaped virtual source on the source plane, of the second pair of dumbbell-shaped virtual source and mixing vector, is deformed

and the fitting is not shown [see the fourth column of Fig. 5(b)]. The deformation of dumb bell appears first on the source plane with the increase of noise as the grid spacing on the source plane is larger than that on the detector plane in the simulation.

The error in localization and characterization of scattering inhomogeneities increases rapidly with the increase of noise, from $\sim 0.1\text{mm}$ in positioning and $\sim 2\%$ in strength at 10% noise to $\sim 3\text{mm}$ in positioning and $\sim 50\%$ in strength at 20% noise. On the other hand, the effect of noise on localization and characterization of absorptive inhomogeneities is much smaller, the errors at both noise levels are less than 0.5mm in positioning and $\sim 2\%$ in strength. The results in Sec. 3.2 and this section are summarized in Tab. 1.

[Figure 5 about here.]

[Table 1 about here.]

3.5 Effect of uncertainty in background

In the examples discussed above, we have assumed the light intensities change measured on the detector plane is obtained with an exact knowledge about the background. To examine the effect of uncertainty in background optical property on the performance of OPTICA, we model the error in the estimation of the background absorption or diffusion coefficients as a uniform Gaussian random field $f(\mathbf{r})$. The Gaussian noise addressed in Sec. 3.4 is set to be zero here. OPTICA operates on a “dirty” scattering wave $-\phi_{\text{sca}}(\mathbf{r}_d, \mathbf{r}_s) + \delta\phi_{\text{sca}}(\mathbf{r}_d, \mathbf{r}_s)$ where $\delta\phi_{\text{sca}}(\mathbf{r}_d, \mathbf{r}_s)$ is the change in the scattered wave from that of a uniform background of absorption μ_a (or diffusion D) to that of a background of absorption $\mu_a + f(\mathbf{r})$ (or diffusion $D + f(\mathbf{r})$). The magnitude of the background uncertainty is represented by the signal to noise ratio (SNR) defined by

$$\text{SNR(dB)} = 10 \log_{10} \frac{\sum_{\mathbf{r}_d} \sum_{\mathbf{r}_s} |\phi_{\text{sca}}(\mathbf{r}_d, \mathbf{r}_s)|^2}{\sum_{\mathbf{r}_d} \sum_{\mathbf{r}_s} |\delta\phi_{\text{sca}}(\mathbf{r}_d, \mathbf{r}_s)|^2}. \quad (13)$$

Figs. 6(a-c) show the case presented in Fig. 3 of Sec. 3.2 with 40dB, 34dB and 10dB SNR due to background absorption uncertainty, respectively. The resolved absorptive inhomogeneity is at

(50.2, 60.3, 20.1)mm with strength 0.0101 at 40dB SNR, and at (50.2, 60.3, 20.1)mm with strength 0.0100 at 34dB SNR, and at (50.6, 60.3, 20.3)mm with strength 0.0090 at 10dB SNR.

The resolved position and strength of the scattering object are found to be (30.1, 30.1, 30.0)mm and $q_2 = -0.99$, (32.1, 32.9, 30.0)mm and $q_2 = -0.95$, and (31.4, 30.0, 27.5)mm and $q_2 = -1.01$ respectively through fitting to the pair of centrosymmetric and two pairs of dumbbell-shaped virtual sources and mixing vectors [see the second to fourth columns of Fig. 5(a)], respectively, at 40dB SNR. The resolved values become (31.6, 31.7, 25.3)mm and $q_2 = -0.52$ and (31.7, 29.6, 31.7) and $q_2 = -0.78$ at 34dB and 10dB SNRs, respectively, from fitting the pair of centrosymmetric virtual source and mixing vector [see the second columns of Figs. 5(b),(c)]. The dumbbell-shaped virtual sources and mixing vectors, esp dumbbell-shaped virtual sources on the source plane, are deformed and the fitting are not shown [see the third and fourth columns of Fig. 5(b),(c)]. The results for the influence of background absorption uncertainty on the performance are summarized in Tab. 2.

[Figure 6 about here.]

[Table 2 about here.]

Figs. 7(a,b) show the case presented in Fig. 3 of Sec. 3.2 with 34dB and 10dB SNR due to background scattering uncertainty. The resolved absorptive inhomogeneity is at (50.1, 60.3, 20.1)mm with strength 0.0100 at 34dB SNR and at (49.9, 60.5, 20.1)mm with strength 0.0099 at 10dB SNR.

The resolved position and strength of the scattering object are found to be (30.0, 30.1, 30.0)mm and $q_2 = -0.99$, (32.2, 33.0, 30.0)mm and $q_2 = -0.96$, and (32.3, 29.3, 27.1)mm and $q_2 = -1.08$ respectively through fitting to the pair of centrosymmetric and two pairs of dumbbell-shaped virtual sources and mixing vectors [see the second to fourth columns of Fig. 5(a)], respectively, at 34dB SNR. The resolved position and strength of the scattering object are found to be (31.7, 31.1, 32.5)mm and $q_2 = -0.75$, (30.9, 31.4, 27.5)mm and $q_2 = -1.08$, respectively through fitting to the pair of centrosymmetric and the first pair of dumbbell-shaped virtual sources and mixing vectors [see the second to fourth columns of Fig. 5(b)] at 10dB SNR. The results for the influence of background scattering uncertainty on the performance are summarized in Tab. 3.

[Figure 7 about here.]

[Table 3 about here.]

The uncertainty in the background absorption or diffusion coefficients affects the performance of OPTICA in a similar fashion as the noise does discussed in Sec. 3.4. The error in localization and characterization of scattering inhomogeneities increases rapidly while the error in localization and characterization of absorptive inhomogeneities only increases mildly with the increase of the uncertainty in the background optical property. The uncertainty in background scattering has a less adverse effect on the performance of OPTICA than that in background absorption.

4 Discussion

The simulational study of OPTICA presented in this article demonstrates its potential in optical imaging of objects in turbid media. It is shown to be able to locate and characterize absorptive and scattering inhomogeneities within highly scattering medium. In particular, OPTICA can discriminate between absorptive and scattering inhomogeneities and locate and characterize complex inhomogeneities which is both absorptive and scattering. The accuracy of localization and characterization of inhomogeneities is high. In the cases investigated for concentrated inhomogeneities within a tissue emulating slab of thickness of 50mm, the errors in resolved object locations are not greater than 1mm and the errors in the resolved optical strengths are $\sim 2\%$ under favorable noise levels and reliable background estimations.

Noise at higher levels and/or larger uncertainty in the optical property of the background medium makes it difficult to discriminate between absorptive and scattering inhomogeneities. In such a situation, other corroborative evidences, such as, multi-wavelength measurements are required to determine the nature of inhomogeneities. Noise at higher levels and/or larger uncertainty in the optical property of the background medium also introduces larger errors in localization and characterization of scattering inhomogeneities. The accuracy of localization and characterization of absorptive inhomogeneities is only affected mildly by the amount of noise and/or uncertainty in the range investigated.

OPTICA has several salient features. First, OPTICA provides the independent components due to the inhomogeneities with minimal processing of the data and does not have to resort to any

specific light propagation model for obtaining this information. Specific light propagation models are needed only in the later stage to determine location and optical strength. Second, different geometries, or even an arbitrary shaped boundary, can be used with OPTICA. Although we used the slab geometry in the work reported in this article, the approach does not depend on any specific geometry. Third, the approach is fast and is amenable to near real time detection and localization of objects in a turbid medium, which is a key consideration for *in vivo* medical imaging.

As it is well known, the diffusion approximation to RTE which is widely used in inverse image reconstruction, does not apply when the separation between any two of the source, the inhomogeneity and the detector is small, or when there are clear regions in the medium. A special treatment is also required when the medium has aligned microstructures, such as, myofibrils, axons, or collagen fibers in tissues.[43] The fact that a prior assumption of a specific model of light propagation in the medium is not assumed in the identification of independent components by ICA and only required in a Green's function analysis of the retrieved independent component is desirable, esp. in such situations which demands a more complex model than the conventional DA. Performing the fitting procedure for each identified independent component is much simpler and transparent than matching the measured light intensity to a forward model iteratively. The quality of reconstruction of OPTICA is expected to be higher than the conventional approach when only an imperfect forward model is available.

OPTICA is most suited to detect small objects. Given its ability to identify low-contrast small objects, the approach is expected to be especially useful for detection of tumors at their early stages of development.

5 Acknowledgments

This work is supported in part by US Army Medical Research and Materials Command, ONR, NYSTAR, and CUNY organized research programs. M. X. thanks the support by the Department of Army (Grant# DAMD17-02-1-0516). M. Alrubaiee thanks NSF for an Advance Placement Fellowship. We acknowledge Dr. W. Cai for helpful discussions.

References

- [1] *Medical optical tomography: functional imaging and monitoring*, Vol. IS11 of *SPIE Institute Series*, G. Muller, R. R. Alfano, S. R. Arridge, J. Beuthan, E. Gratton, M. Kaschke, B. R. Masters, S. Svanberg, and P. van der Zee, eds., (1993).
- [2] A. Yodh and B. Chance, "Spectroscopy and imaging with diffusing light," *Phys. Today* **48**, 38–40 (1995).
- [3] M. A. O’Leary, D. A. Boas, B. Chance, and A. G. Yodh, "Experimental images of heterogeneous turbid media by frequency-domain diffusing-photon tomography," *Opt. Lett.* **20**, 426–428 (1995).
- [4] S. K. Gayen and R. R. Alfano, "Emerging optical biomedical imaging techniques," *Opt. Photon. News* **7**, 17–22 (1996).
- [5] J. C. Hebden, S. R. Arridge, and D. T. Delpy, "Optical imaging in medicine: I. experimental techniques," *Phys. Med. Biol.* **42**, 825–840 (1997).
- [6] S. R. Arridge and J. C. Hebden, "Optical imaging in medicine: II. Modelling and reconstruction," *Phys Med Biol* **42**, 841–853 (1997), (eng).
- [7] W. Cai, S. K. Gayen, M. Xu, M. Zavallos, M. Alrubaiee, M. Lax, and R. R. Alfano, "Optical tomographic image reconstruction from ultrafast time-sliced transmission measurements," *Appl. Opt.* **38**, 4237–4246 (1999).
- [8] S. R. Arridge, "Optical tomography in medical imaging," *Inverse Problems* **15**, R41–R93 (1999).
- [9] D. Grosenick, H. Wabnitz, H. H. Rinneberg, K. T. Moesta, and P. M. Schlag, "Development of a Time-Domain Optical Mammograph and First in vivo Applications," *Appl. Opt.* **38**, 2927–2943 (1999).
- [10] V. Chernomordik, D. Hattery, A. H. Gandjbakhche, A. Pifferi, P. Taroni, A. Torricelli, G. Valentini, and R. Cubeddu, "Quantification by random walk of the optical parameters of

nonlocalized abnormalities embedded within tissuelike phantoms," *Opt. Lett.* **25**, 951–953 (2000).

- [11] V. A. Markel and J. C. Schotland, "Inverse scattering for the diffusion equation with general boundary conditions," *Phys. Rev. E* **64**, 035601 (2001).
- [12] A. H. Hielscher and S. Bartel, "Use of penalty terms in gradient-based iterative reconstruction schemes for optical tomography," *J. Biomed. Opt.* **6**, 183–192 (2001).
- [13] M. Xu, M. Lax, and R. R. Alfano, "Time-resolved Fourier optical diffuse tomography," *J. Opt. Soc. Am. A* **18**, 1535–1542 (2001).
- [14] B. A. Brooksby, H. Dehghani, B. W. Pogue, and K. D. Paulsen, "Near-Infrared (NIR) tomography breast image reconstruction with a priori structural information from MRI: algorithm development for reconstructing heterogeneities," *IEEE J. Selected Topics in Quantum Electron.* **9**, 199–209 (2003).
- [15] H. Dehghani, B. W. Pogue, S. P. Poplack, and K. D. Paulsen, "Multiwavelength three-dimensional near-infrared tomography of the breast: initial simulation, phantom, and clinical results," *Appl. Opt.* **42**, 135–145 (2003).
- [16] in *Topics in Biomedical Optics*, J. C. Hebden, D. A. Boas, J. S. George, and A. J. Durkin, eds., (OSA, 2003), pp. 2869–3329, a special issue of *Appl. Opt.*, Vol 42.
- [17] W. Cai, M. Xu, and R. R. Alfano, "Three dimensional radiative transfer tomography for turbid media," *IEEE JSTQE* **9**, 189–198 (2003).
- [18] L. Wang, P. P. Ho, C. Liu, G. Zhang, and R. R. Alfano, "Ballistic 2-D imaging through scattering walls using an ultrafast optical Kerr gate," *Science* **253**, 769–771 (1991).
- [19] R. R. Alfano, X. Liang, L. Wang, and P. Ho, "Time-resolved imaging of translucent droplets in highly scattering media," *Science* **264**, 1913–1914 (1994).

- [20] W. Cai, M. Lax, and R. R. Alfano, "Analytical solution of the elastic Boltzmann transport equation in an infinite uniform medium using cumulant expansion," *J. Phys. Chem. B* **104**, 3996–4000 (2000).
- [21] W. Cai, M. Lax, and R. R. Alfano, "Analytical solution of the polarized photon transport equation in an infinite uniform medium using cumulant expansion," *Phys. Rev. E* **63**, 016606 (2000), (10 pages).
- [22] M. Xu, W. Cai, M. Lax, and R. R. Alfano, "Photon migration in turbid media using a cumulant approximation to radiative transfer," *Phys. Rev. E* **65**, 066609 (2002).
- [23] A. D. Klose and A. Hielscher, "Fluorescence tomography with simulated data based on the equation of radiative transfer," *Opt. Lett.* **28**, 1019–1021 (2003).
- [24] A. H. Gandjbakhche, G. H. Weiss, R. F. Bonner, and R. Nossal, "Photon path-length distributions for transmission through optically turbid slabs," *Phys. Rev. E* **48**, 810–818 (1993).
- [25] A. H. Gandjbakhche, V. Chernomordik, J. C. Hebden, and R. Nossal, "Time-Dependent Contrast Functions for Quantitative Imaging in Time-Resolved Transillumination Experiments," *Appl. Opt.* **37**, 1973–1981 (1998).
- [26] *Ill-posed problems in the natural sciences*, A. N. Tikhonov and A. V. Groncharsky, eds., (MIR, Moscow, 1987).
- [27] P. Comon, "Independent component analysis—a new concept?," *Signal Processing* **36**, 287–314 (1994).
- [28] A. J. Bell, "Information Theory, Independent Component Analysis, and Applications," in *Unsupervised Adaptive Filtering, Vol. I*, S. Haykin, ed., (Wiley, 2000), pp. 237–264.
- [29] D. Nuzillard and J.-M. Nuzillard, "Application of Blind Source Separation to 1-D and 2-D Nuclear Magnetic Resonance Spectroscopy," *IEEE Signal Processing Letters* **5**, 209–211 (August 1998).

- [30] R. Vigário, J. Särelä, V. Jousmäki, M. Hämäläinen, and E. Oja, "Independent Component Approach to the Analysis of EEG and MEG Recordings," *IEEE Trans. Biomedical Engineering* **47**, 589–593 (2000).
- [31] A. Hyvärinen, J. Karhunen, and E. Oja, *Independent Component Analysis* (John Wiley, New York, 2001), 481+xxii pages.
- [32] J.-F. Cardoso, "Blind signal separation: statistical principles," *Proceedings of the IEEE* **9**, 2009–2025 (1998).
- [33] A. Hyvärinen and E. Oja, "Independent component analysis: algorithms and applications," *Neural Networks* **13**, 411–430 (2000).
- [34] S. Chandrasekhar, *Radiative transfer* (Dover, New York, 1960).
- [35] M. Xu, W. Cai, M. Lax, and R. R. Alfano, "A photon transport forward model for imaging in turbid media," *Opt. Lett.* **26**, 1066–1068 (2001).
- [36] P. M. Morse and H. Feshbach, *Methods of theoretical physics* (McGraw-Hill, New York, 1953), Vol. I and II.
- [37] M. Lax, V. Nayaramamurti, and R. C. Fulton, "Classical diffusion photon transport in a slab," in *Laser Optics of Condensed Matter*, J. L. Birman, H. Z. Cummins, and A. A. Kaplyanskii, eds., (Plenum, New York, 1987), pp. 229–237.
- [38] J. X. Zhu, D. J. Pine, and D. A. Weitz, "Internal reflection of diffusive light in random media," *Phys. Rev. A* **44**, 3948–3959 (1991).
- [39] R. C. Haskell, L. O. Svaasand, T.-T. Tsay, T.-C. Feng, M. S. McAdams, and B. J. Tromber, "Boundary conditions for the diffusion equation in radiative transfer," *J. Opt. Soc. Am. A* **11**, 2727–2741 (1994).
- [40] S. R. Arridge, "Photon-measurement density functions. Part I: Analytic forms," *Appl. Opt.* **34**, 7395–7409 (1995).

- [41] S. R. Arridge and M. Schweiger, "Photon-measurement density functions. Part 2: Finite-element-method calculations," *Appl. Opt.* **34**, 8026–8037 (1995).
- [42] H. Heusmann, J. Kölzer, and G. Mitic, "Characterization of female breasts *in vivo* by time resolved and spectroscopic measurements in near infrared spectroscopy," *J. Biomed. Opt.* **1**, 425–434 (1996).
- [43] J. Heino, S. Arridge, J. Sikora, and E. Somersalo, "Anisotropic effects in highly scattering media," *Phys. Rev. E* **68**, 031908 (2003), (8 pages).

List of Figures

1	The light intensity on one side of the slab is measured when a point source scans on the other side. Two inhomogeneities are placed at (50, 60, 20)mm and (30, 30, 30)mm inside the slab.	24
2	Normalized independent spatial intensity distributions on the input (or source) plane (the first row), the exit (or detector) plane (the second row), and the least square fitting using Eq. ?? (the third row). The left column is for the first absorptive inhomogeneity at (50, 60, 20)mm and the right column is for the second absorptive inhomogeneity at (30, 30, 30)mm. On the third row, the horizontal profile of intensity distributions on the source plane (diamond) and on the detector plane (circle) are displayed, and solid lines show the respective Green's function fit used for obtaining locations and strengths of objects. The noise level is 5%.	25
3	Normalized independent spatial intensity distribution on the source plane, i.e., virtual sources (the first row) and on the detector plane, i.e., mixing vectors (the second row), and the least square fitting (the third row). The first column is for the first absorptive inhomogeneity at (50, 60, 20)mm and the second through fourth columns are for the second scattering inhomogeneity at (30, 30, 30)mm and represent the centrosymmetric and two dumbbell-shaped pairs of virtual sources and mixing vectors, respectively. The dumb bell comprises one bright part and its antisymmetric dark counterpart. On the third row, the profile of intensity distributions on the source plane (diamond) and on the detector plane (circle) are displayed, and solid lines show the respective Green's function fit used for obtaining locations and strengths of objects. The coordinate X is the horizontal coordinate. The coordinate ρ is the coordinate on the symmetrical line passing through the dumb bell axis. The small dark circular region appearing near the right-upper corner of the normalized independent spatial intensity distribution on on the first row and in the fourth column is an artifact.	26
4	Normalized independent spatial intensity distribution on the source plane (the first row) and on the detector plane (the second row), and the least square fitting (the third row) for one inhomogeneity located at (30, 30, 20)mm with strengths of absorption $q_1 = 0.01$ and diffusion $q_2 = 1$. The first and second columns correspond to the pairs of dumbbell-shaped virtual sources and mixing vectors produced by its scattering component. The third column corresponds to its absorptive component obtained by first removal the scattering contribution. On the third row, the profile of intensity distributions on the source plane (diamond) and on the detector plane (circle) are displayed, and solid lines show the respective Green's function fit used for obtaining locations and strengths of objects. The coordinate X is the horizontal coordinate. The coordinate ρ is the coordinate on the symmetrical line passing through the dumb bell axis.	27
5	Same as Fig. 3 with (a) 10% and (b) 20% Gaussian noise. The dumbbell-shaped virtual source on the source plane in the fourth column of (b) is deformed and the least square fitting is not shown.	28
6	Same as Fig. 3 with (a) 40dB, (b) 34dB and (c) 10dB background absorption uncertainty.	29
7	Same as Fig. 3 with (a) 34dB and (b) 10dB background scattering uncertainty. . .	30

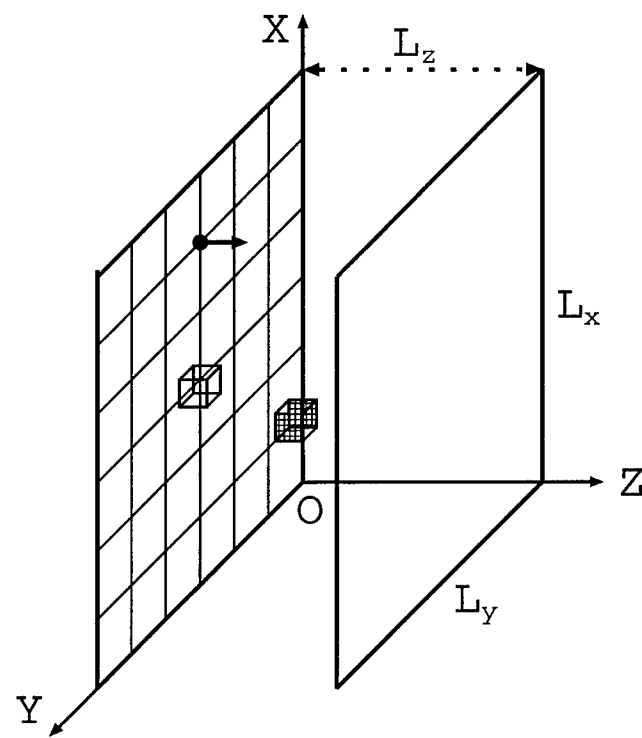


Figure 1: M. Xu et. al.

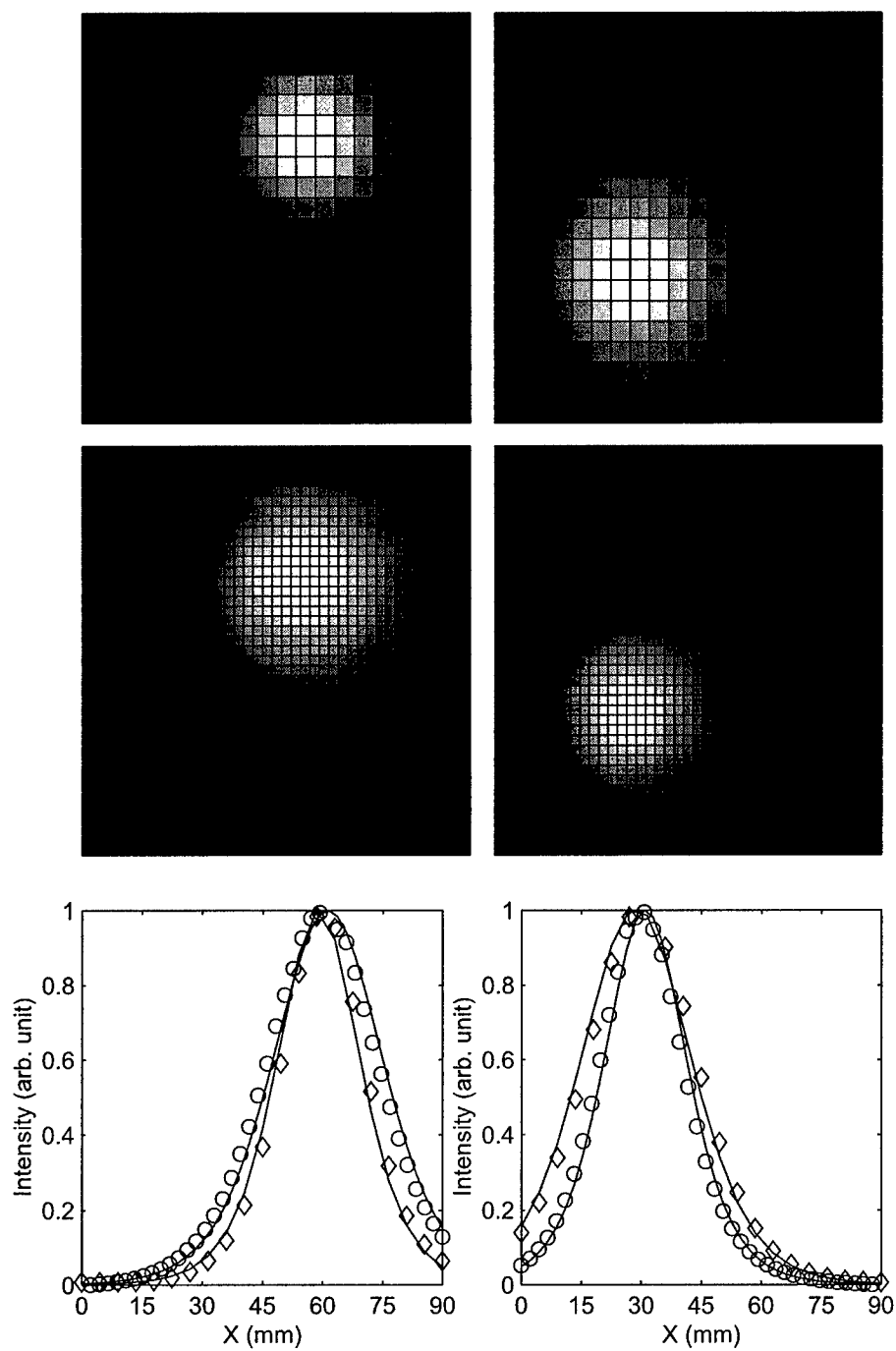


Figure 2: M. Xu et. al.

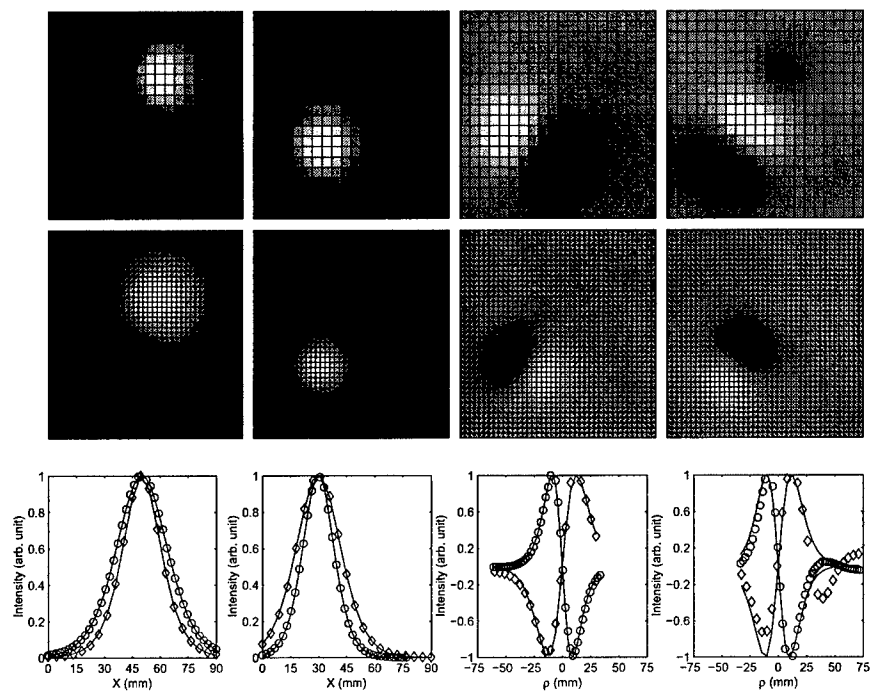


Figure 3: M. Xu et. al.

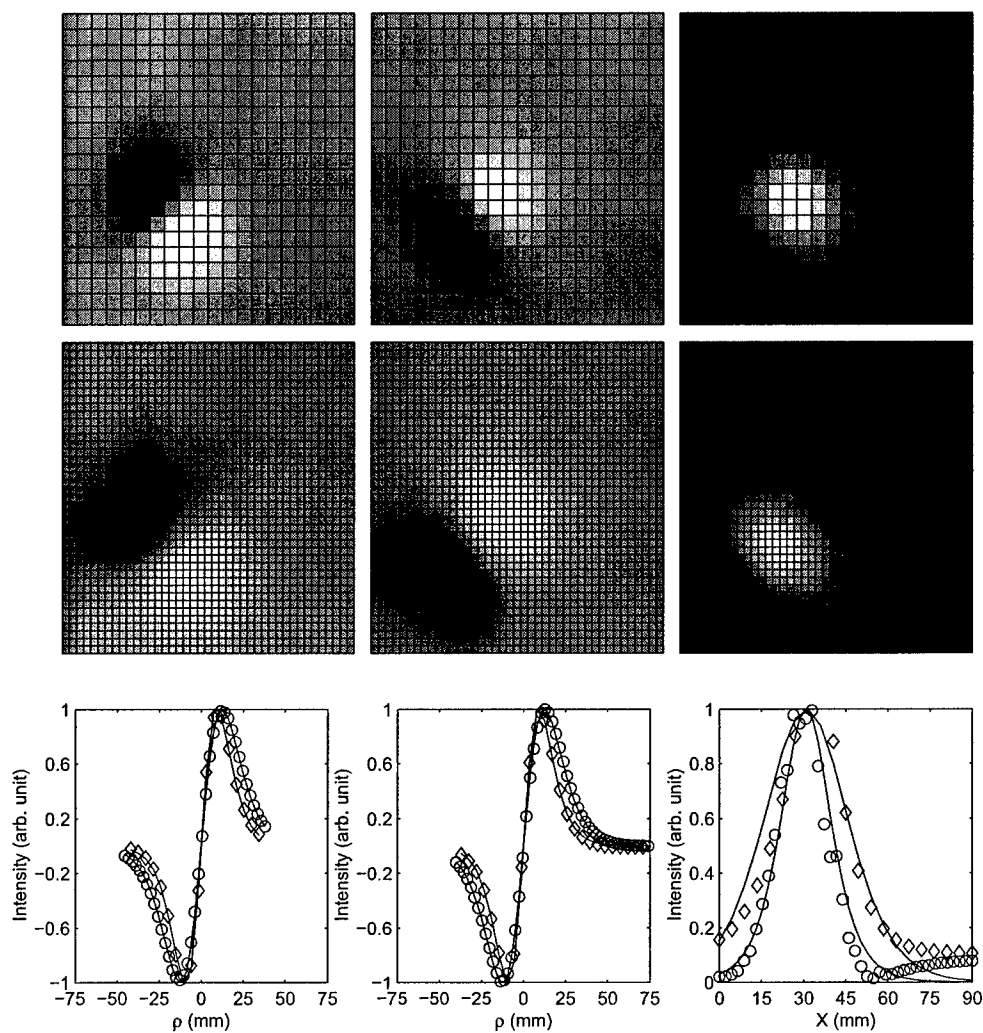


Figure 4: M. Xu et. al.

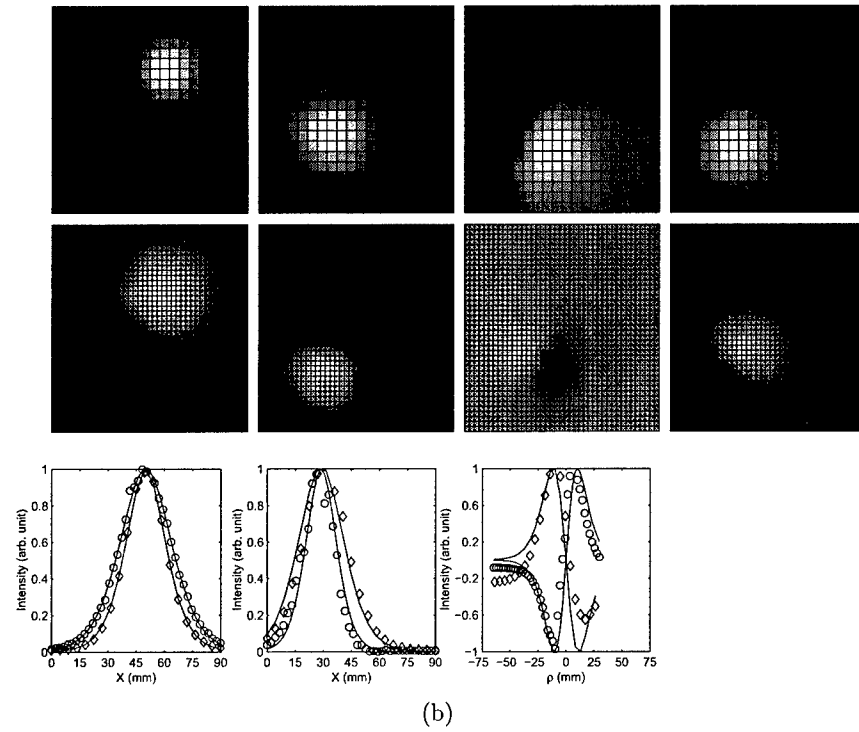
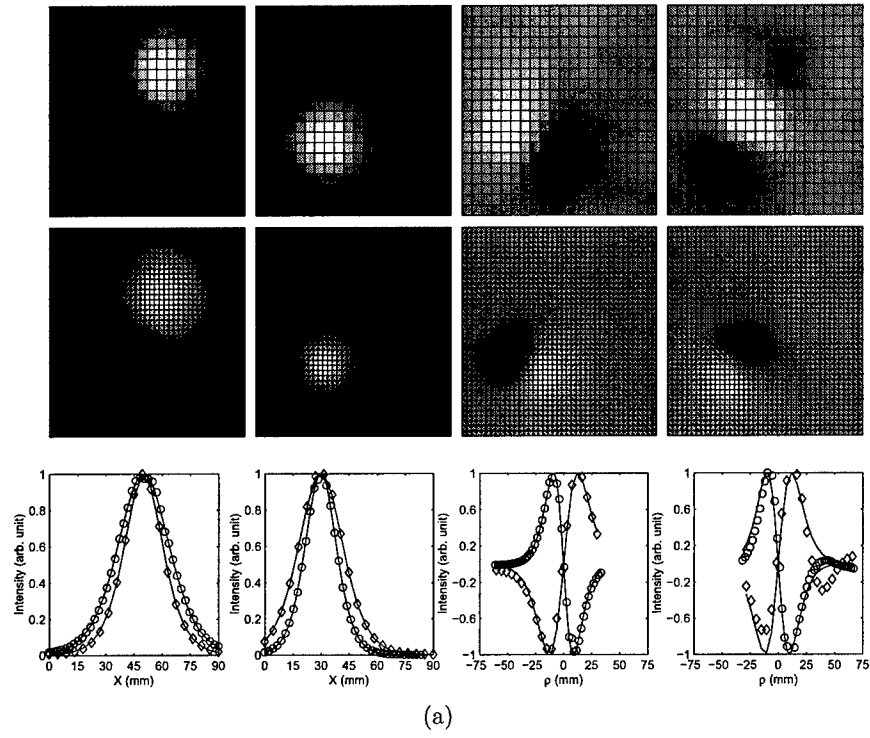


Figure 5: M. Xu et. al.

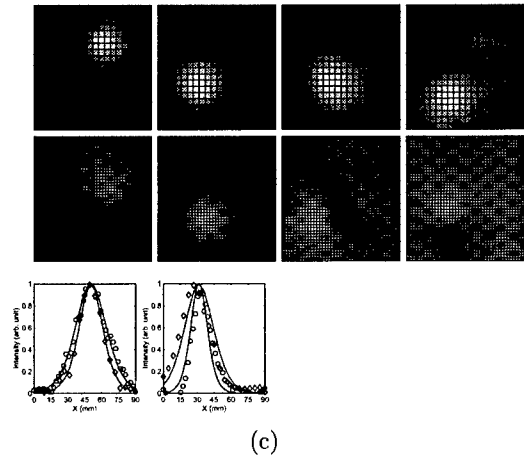
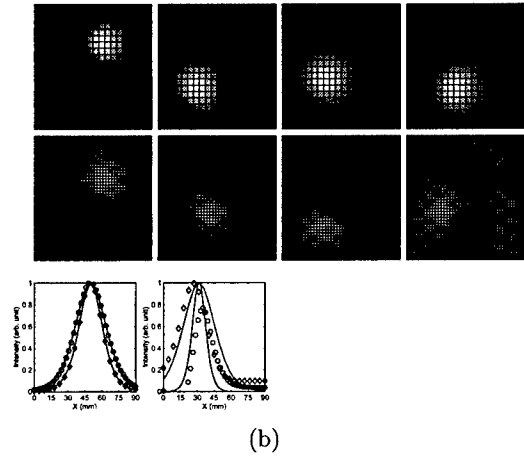
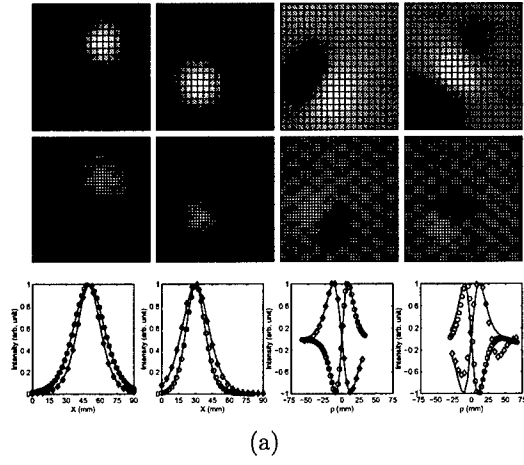


Figure 6: M. Xu et. al.

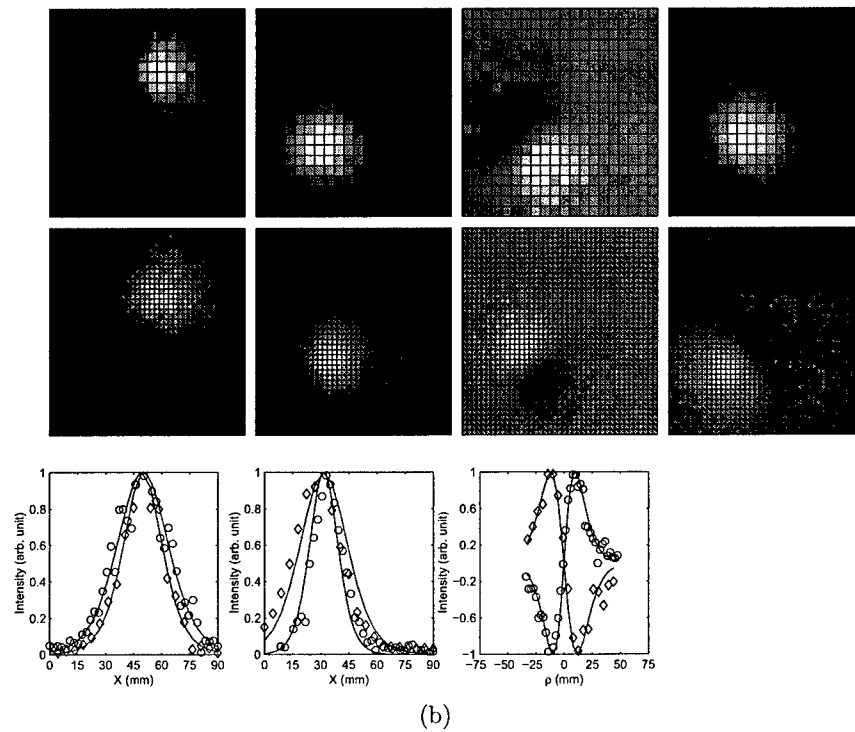
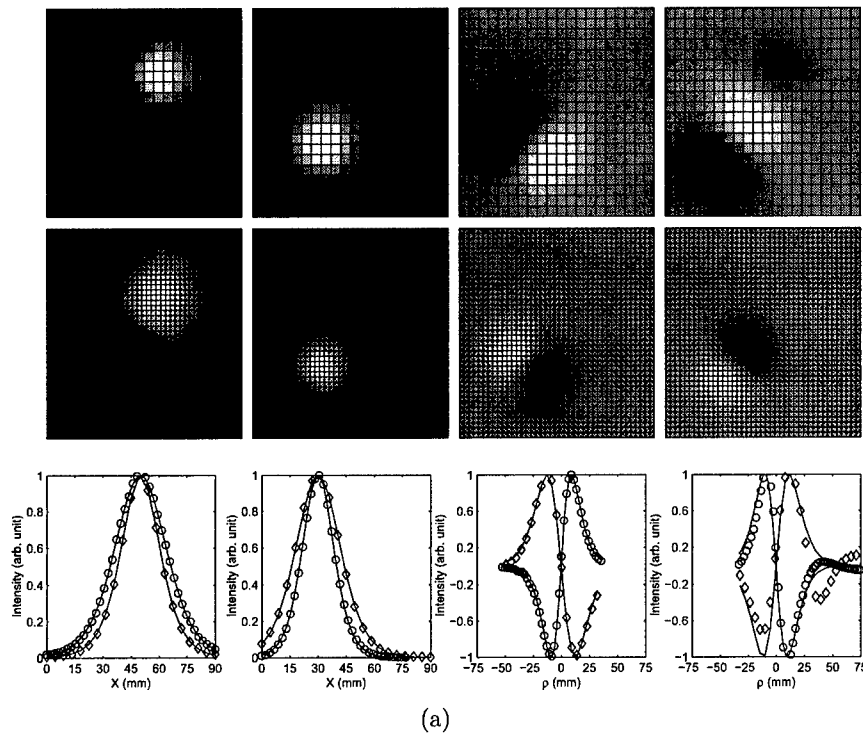


Figure 7: M. Xu et. al.

List of Tables

1	Comparison of known and OPTICA determined positions and strengths of absorption (Abs) and scattering (Sca) inhomogeneities under different levels of Gaussian noise.	32
2	Comparison of known and OPTICA determined positions and strengths of absorption (Abs) and scattering (Sca) inhomogeneities under different levels of background absorption uncertainty.	33
3	Comparison of known and OPTICA determined positions and strengths of absorption (Abs) and scattering (Sca) inhomogeneities under different levels of background scattering uncertainty.	34

Noise	Target	Known Position (x, y, z) (mm)	Known Strength	Resolved Position (x, y, z) (mm)	Resolved Strength	Error in Position	Error in Strength
5%	Abs	(50, 60, 20)	0.01	(50.2, 60.3, 20.2)	0.0101	$\sim 0.3\text{mm}$	$\sim 1\%$
	Sca	(30, 30, 30)	-1	(30.0, 30.0, 30.0)	-0.99	$\sim 0.1\text{mm}$	$\sim 1\%$
10%	Abs	(50, 60, 20)	0.01	(50.2, 60.3, 20.1)	0.0101	$\sim 0.3\text{mm}$	$\sim 1\%$
	Sca	(30, 30, 30)	-1	(30.0, 30.1, 30.0)	-0.98	$\sim 0.1\text{mm}$	$\sim 2\%$
20%	Abs	(50, 60, 20)	0.01	(50.1, 60.3, 20.5)	0.0102	$\sim 0.5\text{mm}$	$\sim 2\%$
	Sca	(30, 30, 30)	-1	(28.9, 27.0, 32.9)	-0.59	$\sim 3\text{mm}$	$\sim 50\%$

Table 1: M. Xu et. al.

SNR (dB)	Target	Known Position (x, y, z) (mm)	Known Strength	Resolved Position (x, y, z) (mm)	Resolved Strength	Error in Position	Error in Strength
40	Abs	(50, 60, 20)	0.01	(50.2, 60.3, 20.1)	0.0101	$\sim 0.3\text{mm}$	$\sim 1\%$
	Sca	(30, 30, 30)	-1	(30.1, 30.1, 30.0)	-0.99	$\sim 0.1\text{mm}$	$\sim 1\%$
34	Abs	(50, 60, 20)	0.01	(50.2, 60.3, 20.1)	0.0100	$\sim 0.3\text{mm}$	$\sim 1\%$
	Sca	(30, 30, 30)	-1	(31.6, 31.7, 25.3)	-0.52	$\sim 5\text{mm}$	$\sim 50\%$
10	Abs	(50, 60, 20)	0.01	(50.6, 60.3, 20.3)	0.0090	$\sim 0.3\text{mm}$	$\sim 10\%$
	Sca	(30, 30, 30)	-1	(31.7, 29.6, 31.7)	-0.78	$\sim 5\text{mm}$	$\sim 50\%$

Table 2: M. Xu et. al.

SNR (dB)	Target	Known Position (x, y, z) (mm)	Known Strength	Resolved Position (x, y, z) (mm)	Resolved Strength	Error in Position	Error in Strength
34	Abs	(50, 60, 20)	0.01	(50.1, 60.3, 20.1)	0.0100	$\sim 0.3\text{mm}$	$\sim 1\%$
	Sca	(30, 30, 30)	-1	(30.0, 30.1, 30.0)	-0.99	$\sim 0.1\text{mm}$	$\sim 1\%$
10	Abs	(50, 60, 20)	0.01	(49.9, 60.5, 20.1)	0.0099	$\sim 0.5\text{mm}$	$\sim 1\%$
	Sca	(30, 30, 30)	-1	(31.7, 31.1, 32.5)	-0.75	$\sim 2.5\text{mm}$	$\sim 25\%$

Table 3: M. Xu et. al.

Multiple passages of light through an absorption inhomogeneity in optical imaging of turbid media

M. Xu, W. Cai, and R. R. Alfano

Institute for Ultrafast Spectroscopy and Lasers, New York State Center of Advanced Technology for Ultrafast Photonic Materials and Applications, and Department of Physics, The City College and Graduate Center of the City University of New York, New York, New York 10031

Received March 24, 2004

Multiple passages of light through an absorption inhomogeneity of finite size deep within a turbid medium are analyzed for optical imaging by use of the self-energy diagram. The nonlinear correction becomes more important for an inhomogeneity of a larger size and with greater contrast in absorption with respect to the host background. The nonlinear correction factor agrees well with that from Monte Carlo simulations for cw light. The correction is approximately 50%–75% in the near infrared for an absorption inhomogeneity with the typical optical properties found in tissues and five times the size of the transport mean free path. © 2004 Optical Society of America

OCIS codes: 290.4210, 290.7050, 170.3660.

The main objective of optical imaging of turbid media is to locate and identify the embedded inhomogeneities by essentially inverting the difference in photon transmittance in the time or frequency domains due to the presence of these inhomogeneities.^{1–4} The key quantity involved is the Jacobian, which quantifies the influence on the detected signal due to the change of the optical parameters of the medium. The linear perturbation approach is suitable for calculating the Jacobian for only a small and weak absorption inhomogeneity and is not valid when the absorption strength is large.⁵ This failure can be attributed to the multiple passages through the abnormal site by the photon. The most important correction is the self-energy correction,⁶ which takes into account the repeated visits made by a photon through the site up to an infinite number of times. The presence of other inhomogeneity islands can be ignored because the photon propagator decreases rapidly with the distance between two separate sites.

In this Letter the nonlinear correction for an absorption inhomogeneity of a large strength due to repeated visits by the photon is modeled by a nonlinear correction factor (NCF) to the linear perturbation approach. The NCF as a function of the size and the strength of the inhomogeneity is estimated by use of the self-energy diagram. The NCF is obtained from the cumulant approximation to the radiative transfer and verified by Monte Carlo simulations for cw light. The magnitude of the NCF is 0.5–1 for an absorptive inhomogeneity of up to $5l_t$ (l_t is the mean transport free path of light) and of the typical optical properties of human tissues ($\mu_a l_t / c \sim 0.01$ – 0.05 , where μ_a is the absorption coefficient and c is the speed of light in the medium).

If we consider an absorption site centered at $\bar{\mathbf{r}}$ and far away from both the source and the detector, change in detected light ΔI at detector \mathbf{r}_d from a modulated point source at \mathbf{r}_s including the multiple passages through the site is given by

$$\begin{aligned} \Delta I &= -G(\mathbf{r}_d, \omega | \bar{\mathbf{r}}) V \delta \mu_a(\bar{\mathbf{r}}) \sum_{n=0}^{\infty} [-\bar{N}_{\text{self}}(\omega; R) V \delta \mu_a(\bar{\mathbf{r}})]^n \\ &\quad \times G(\bar{\mathbf{r}}, \omega | \mathbf{r}_s) \\ &= -G(\mathbf{r}_d, \omega | \bar{\mathbf{r}}) \frac{V \delta \mu_a(\bar{\mathbf{r}})}{1 + \bar{N}_{\text{self}}(\omega; R) V \delta \mu_a(\bar{\mathbf{r}})} \\ &\quad \times G(\bar{\mathbf{r}}, \omega | \mathbf{r}_s), \end{aligned} \quad (1)$$

where $\delta \mu_a$ is the excess absorption of the absorption site of size R and volume V , ω is the modulation frequency of light, G is the propagator of photon migration in the background medium, and

$$\bar{N}_{\text{self}}(\omega; R) = \frac{1}{V^2} \int_V \int_V G(\mathbf{r}_2, \omega | \mathbf{r}_1) d^3 \mathbf{r}_2 d^3 \mathbf{r}_1 \quad (2)$$

is the self-propagator that describes the probability that a photon revisits volume V . Here $G(\mathbf{r}_2, \omega | \mathbf{r}_1)$ gives the probability density that a photon leaves the volume at \mathbf{r}_1 and reenters it at \mathbf{r}_2 . The scattering property of the site is the same as that of the background. In Eq. (1) $G(\mathbf{r}_d, \omega | \bar{\mathbf{r}})$ and $G(\bar{\mathbf{r}}, \omega | \mathbf{r}_s)$ are well modeled by the center-moved diffusion model as long as separations $|\mathbf{r}_d - \bar{\mathbf{r}}|$ and $|\mathbf{r}_s - \bar{\mathbf{r}}|$ are much greater than l_t .⁷ However, the diffusion Green's function cannot be used in Eq. (2) to evaluate $\bar{N}_{\text{self}}(\omega; R)$ because the diffusion approximation breaks down when \mathbf{r}_1 is in the proximity of \mathbf{r}_2 .

Comparing Eq. (1) with the standard linear perturbation approach, the nonlinear multiple passage effect of an absorption site is represented by a NCF:

$$\text{NCF} = [1 + \bar{N}_{\text{self}}(\omega; R) V \delta \mu_a(\bar{\mathbf{r}})]^{-1}. \quad (3)$$

This factor serves as a universal measure of the nonlinear multiple-passage effect as long as the absorption site is far from both the source and the detector and its size is much smaller than its distance to both the source and the detector. This correction is more significant when the NCF is further away from unity.

Photon propagator $N(\mathbf{r}_2, t | \mathbf{r}_1, \mathbf{s})$, the probability that a photon propagates from position \mathbf{r}_1 with propagation direction \mathbf{s} to position \mathbf{r}_2 in time t , for any separation between \mathbf{r}_1 and \mathbf{r}_2 , was recently derived^{7,8} in the form of a cumulant approximation to the radiative transfer.

In the case of interest in which the absorption site is deep inside the medium, the photon distribution is isotropic. The photon propagator is simplified to $N_{\text{eff}}(r, t) \equiv N_{\text{eff}}(|\mathbf{r}_2 - \mathbf{r}_1|, t)$, which is obtained by averaging $N(\mathbf{r}_2, t | \mathbf{r}_1, \mathbf{s})$ over the propagation direction \mathbf{s} of light over the 4π solid angle. In the frequency domain this effective propagator is approximately given by

$$N_{\text{eff}}(r, \omega) = \begin{cases} \frac{1}{4\pi r^2 c} \exp\left(-\frac{1}{3} \kappa^2 l_t r\right) \\ + \frac{\exp(-\kappa l_t)}{4\pi D r \kappa l_t} \sinh(\kappa r), & r < l_t, \\ \frac{\exp(-\kappa r)}{4\pi D r \kappa l_t} \sinh(\kappa l_t), & r \geq l_t \end{cases} \quad (4)$$

where $D \equiv l_t c/3$ and $\kappa \equiv [3(\mu_a - i\omega)/l_t c]^{1/2}$, whose sign is chosen with a nonnegative real part. The two terms in N_{eff} when $r < l_t$ represent ballistic and diffusion contributions, respectively. The ballistic term does not depend on scattering because the photon distribution involved is already isotropic. Only diffusion contributes to N_{eff} when $r > l_t$. The self-propagator for an absorption sphere deep inside the medium is given by

$$\begin{aligned} \bar{N}_{\text{self}}(\omega; R) &= \frac{1}{V^2} \int_V \int_V N_{\text{eff}}(|\mathbf{r}_2 - \mathbf{r}_1|, \omega) d^3 \mathbf{r}_2 d^3 \mathbf{r}_1 \\ &= \frac{1}{V} \int_0^{2R} N_{\text{eff}}(r, \omega) \gamma_0(r) 4\pi r^2 dr, \end{aligned} \quad (5)$$

where $\gamma_0(r) = 1 - (3r/4R) + (1/16)(r/R)^3$ is the characteristic function for a uniform sphere.⁹ An absorption site of an arbitrary shape can be treated the same way. The exact self-propagator must be computed by a numerical quadrature. A good approximation of $\bar{N}_{\text{self}}(\omega; R)$ is

$$\bar{N}_{\text{self}}(\omega; R) = \frac{l_t}{Vc} \times \begin{cases} \left(\frac{3}{4} \xi + \xi^3 \right) - \xi^3 \kappa l_t + \mathcal{O}(\kappa^2), & \xi \leq 1/2 \\ \left(\frac{6}{5} \xi^2 + \frac{1}{2} - \frac{3}{16} \xi^{-1} + \frac{3}{320} \xi^{-3} \right) \\ - \xi^3 \kappa l_t + \mathcal{O}(\kappa^2), & \xi > 1/2 \end{cases} \quad (6)$$

by use of relation (4), where $\xi \equiv R/l_t$ when $|\kappa|R \ll 1$. The exact and approximate versions of dimensionless self-propagator $\bar{N}_{\text{self}} V l_t^{-1} c$ when $\kappa = 0$ are plotted as solid and dashed curves, respectively, in Fig. 1(a). Dimensionless self-propagator $\bar{N}_{\text{self}} V l_t^{-1} c$ depends solely on two dimensionless quantities κl_t of the background and R/l_t of the absorbing sphere.

It is worthwhile to point out that the self-propagator in time $\bar{N}_{\text{self}}(t; R)$, the inverse Fourier transform of

Eq. (5), includes the contribution from the ballistic motion of the photon when the photon passes through the site. This ballistic contribution manifests itself as the linear decay of $N_{\text{self}}(t; R)V$ in the form of $\gamma_0(ct)$ near the origin of the time, followed by a transition to diffusion [Fig. 1(b)].

The NCF is obtained by plugging Eq. (5) or (6) into Eq. (3). In particular, we have

$$\text{NCF} \approx \begin{cases} \left[1 + \frac{9}{16\pi} q \left(\xi^{-2} + \frac{4}{3} \right) \right]^{-1}, & \xi \leq 1/2 \\ \left[1 + \frac{9}{10\pi} q \left(\xi^{-1} + \frac{5}{12} \xi^{-3} \right) \right. \\ \left. - \frac{5}{32} \xi^{-4} + \frac{1}{128} \xi^{-6} \right]^{-1}, & \xi > 1/2 \end{cases} \quad (7)$$

where $q \equiv V \delta \mu_a(\bar{\mathbf{r}})/l_t^2 c$ is the dimensionless strength of the absorber when $|\kappa|R \ll 1$. For an absorber of fixed $q > 0$, the effectiveness of absorbing light is diminished (the NCF decreases) when its size is reduced. This can be understood from the fact that the photon spends less time per volume inside the absorber of a smaller dimension because of the ballistic motion of the photon after each scattering event. The photon leaves a small site ($R < l_t$) in an almost straight line. The diffusion behavior for an individual photon is observed only after a large number of scattering and on a scale larger than l_t .

Figure 2 shows plots of the NCF versus absorber size for typical absorbers of excess absorption $\delta \mu_a l_t/c$ equal to 0.01 and 0.05. The nonlinear correction factor generally decreases with the size of the absorber whose excess absorption is fixed. With the increase of the background absorption and the modulation frequency, the nonlinear correction becomes less accentuated. The phase delay is larger for higher modulation frequencies and less background absorption.

Monte Carlo simulations¹⁰ are performed for cw light propagating in a uniform nonabsorbing and isotropic scattering slab. The thickness of the slab is $L = 80l_t$. A spherical absorber of radius R is located at the center $(0, 0, L/2)$ of the slab. The excess absorption of the absorber is $\delta \mu_a l_t/c = 0.01$. The absorber has the same scattering property as the background. The details of the Monte Carlo computation were provided in a previous publication.¹¹ The correlated sampling method

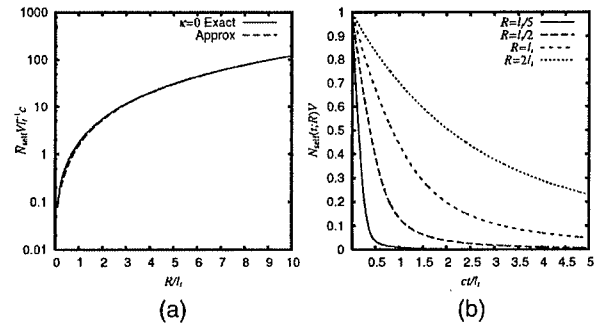


Fig. 1. (a) Self-propagator $\bar{N}_{\text{self}}(\omega; R) V l_t^{-1} c$ and its approximation form when $\kappa = 0$. (b) Self-propagator for spheres of various radii in the time domain inside a nonabsorbing medium.

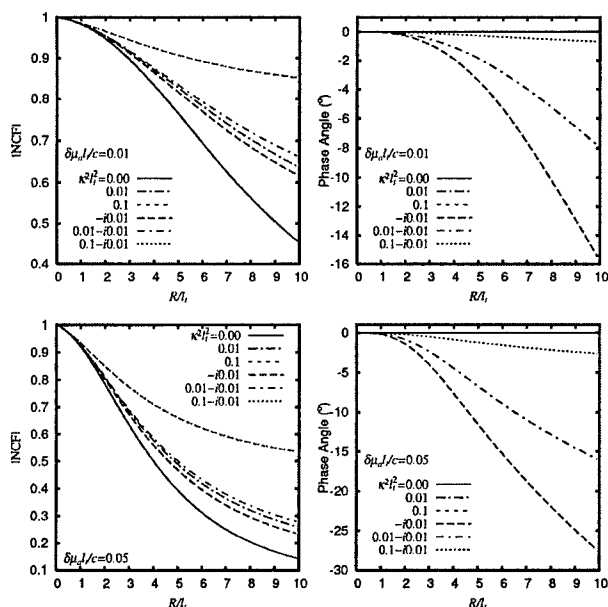


Fig. 2. NCF (magnitude and phase angle) versus the size of absorbers whose excess absorption $\delta\mu_a l_t/c$ equals 0.01 and 0.05. Note that $\kappa^2 l_t^2 = 3(\mu_a - i\omega)l_t/c$ for the background medium.

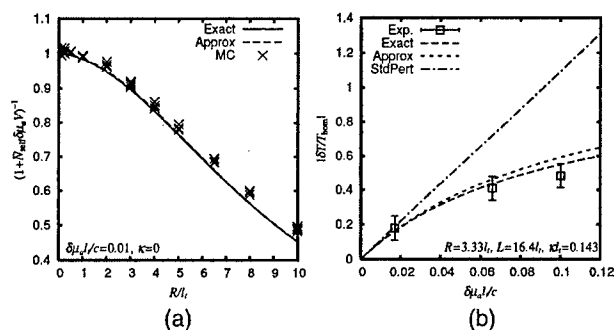


Fig. 3. (a) Theoretical nonlinear correction factors from numerical quadrature (Exact), the approximate form of relation (7) (Approx), and Monte Carlo simulations (MC). Results from four independent Monte Carlo simulations are shown for each radius. The standard linear perturbation approach corresponds to horizontal line NCF = 1 (not shown in the figure). (b) Percentage change of the cw transmittance from the experimental data given in Fig. 9 of Ref. 5 compared with the theoretical predictions made by the standard linear perturbation approach (StdPert) and those including NCF (Exact and Approx).

is used in each simulation to reduce variance.¹² A single simulation is used to compute the change in light transmittance due to the presence of the absorption site and the corresponding NCF. Figure 3(a) shows the NCFs obtained from numerical quadrature, the approximate form of relation (7), and Monte Carlo simulations. The agreement between our theoretical NCF and that from Monte Carlo simulations is excellent. The slight difference between them at large radii is accounted for by the fact that the sphere can no longer

be regarded as small compared with the dimensions of the slab.

Figure 3(b) shows the percentage change of the cw transmittance estimated from the experimental data given in Fig. 9 of Ref. 5. The relevant parameters of the experiment are summarized in the inset. The theoretical predictions from the linear perturbation approach with and without the nonlinear correction are also shown in Fig. 3(b), assuming a collimated point source and a point detector in a confocal setup. Our theoretical prediction with nonlinear correction provides a significant improvement over linear perturbation and agrees much better with the experimental result.

The typical value of the absorption coefficient of human tissues in the near infrared indicates that $\mu_a l_t/c \sim 0.01-0.05$.^{13,14} This fact should put our results on NCFs in this range (Figs. 2 and 3) into perspective. The nonlinear correction becomes more important for an inhomogeneity of a larger size and with greater contrast in absorption with respect to the background. The value of the NCF decreases from ~ 0.75 to ~ 0.5 for an absorption site of radius $5l_t$ with excess absorption $\delta\mu_a l_t/c$ increasing from 0.01 to 0.05. The standard linear perturbation approach in optical imaging should be augmented to include this nonlinear correction.

This work was supported in part by NASA and the U.S. Army. M. Xu acknowledges support from the U.S. Department of the Army (grant DAMD17-02-1-0516). The authors are indebted to the anonymous referees who helped improve this Letter. M. Xu's e-mail address is minxu@sci.ccnycun.edu.

References

1. A. Yodh and B. Chance, *Phys. Today* **48**(3), 38 (1995).
2. S. R. Arridge, *Inverse Probl.* **15**, R41 (1999).
3. A. H. Gandjbakhche, V. Chernomordik, J. C. Hebden, and R. Nossal, *Appl. Opt.* **37**, 1973 (1998).
4. W. Cai, S. K. Gayen, M. Xu, M. Zavallos, M. Alrubaiee, M. Lax, and R. R. Alfano, *Appl. Opt.* **38**, 4237 (1999).
5. S. Carraresi, T. S. M. Shatir, F. Martelli, and G. Zaccanti, *Appl. Opt.* **40**, 4622 (2001).
6. J. W. Negele and H. Orland, *Quantum Many-Particle Systems* (Westview, Boulder, Colo., 1998).
7. M. Xu, W. Cai, M. Lax, and R. R. Alfano, *Opt. Lett.* **26**, 1066 (2001).
8. W. Cai, M. Lax, and R. R. Alfano, *Phys. Rev. E* **61**, 3871 (2000).
9. A. Guinier, G. Fournet, C. B. Walker, and K. L. Yudowitch, *Small-Angle Scattering of X-Rays* (Wiley, New York, 1955).
10. M. Testorf, U. Osterberg, B. Pogue, and K. Paulsen, *Appl. Opt.* **38**, 236 (1999).
11. M. Xu, W. Cai, M. Lax, and R. R. Alfano, *Phys. Rev. E* **65**, 066609 (2002).
12. H. Rief, *J. Comput. Phys.* **111**, 33 (1994).
13. V. G. Peters, D. R. Wyman, M. S. Patterson, and G. L. Frank, *Phys. Med. Biol.* **35**, 1317 (1990).
14. W. F. Cheong, S. Prahl, and A. J. Welch, *IEEE J. Quantum Electron.* **26**, 2166 (1990).

In situ determination of refractive index and size of *Bacillus* spores by light transmission

A. Katz, Alexandra Alimova, M. Xu, Paul Gottlieb, Elizabeth Rudolph, J. C. Steiner, and R. R. Alfano

Department of Physics, The City College of New York, New York, New York 10031

Received October 29, 2004

Light-extinction measurements in the wavelength range of 400 to 1000 nm are performed *in situ* on *Bacillus subtilis* endospores during heat-shock-induced activation. Simultaneous information on particle size and refractive indices during activation is calculated from the transmission spectra by use of the Gaussian ray approximation of anomalous diffraction theory. During activation the refractive index of the core decreases from 1.51 to 1.39, and the size increases from 0.38 to 0.6 μm . © 2005 Optical Society of America

OCIS codes: 000.1430, 290.5820.

Light scattering has long been investigated as a tool for identifying bacteria size and shape,¹⁻⁴ and quasi-elastic light scattering has been used to study endospore (ES) structure.^{5,6} The Gaussian ray approximation (GRA) of anomalous diffraction theory has been used to determine the size and shape of different species of bacteria from light transmission.^{3,7} Bacterial cell size typically varies from the submicrometer level to several micrometers; thus their scattering properties in the visible are strongly dependent on wavelength, size, shape, and refractive index. The bacteria genera *Bacillus* and *Clostridium* can differentiate to form an ES, a dormant cell type, in response to hostile environments and can revert to vegetative cells by germination when conditions become more receptive. The structural changes occurring during germination are important to biologists⁵ and in bioagent detection. In the past, fluorescence was shown to be an effective technique to detect ESs *in situ*.⁸ Combining light scattering, extinction, and fluorescence might offer an ideal tool to determine the type of agent present.

In this Letter light extinction is used *in situ* to monitor *Bacillus subtilis* ES activation and to simultaneously retrieve the refractive index and size of the ES during this process. The optical techniques and methods described allow for the real-time visualization of the ES activation process and the initial stage of bacterial differentiation. The results may have important significance in bioagent identification systems and modeling applications.

ESs are significantly denser than and their refractive index is greater than that of vegetative cells. ESs consist of a high-density, dehydrated core surrounded by a lower-density spore coat composed of cross-linked polypeptides. Germination begins with activation, during which the coat is shed and the core hydrates with a subsequent decrease in density and refractive index and an increase in size.

From the recent statistical interpretation of anomalous diffraction theory^{9,10} light extinction by soft particles is mainly determined by the mean and mean-squared size of the particles in the GRA. The scattering cross section can be approximated by

$$C_s = \pi r^2 \left[\frac{4n^2\pi^2}{\lambda^2} (m-1)^2 (\mu^2 - \sigma^2) - \frac{4n^4\pi^4}{3\lambda^4} (m-1)^4 (\mu^4 + 3\sigma^4 + 6\mu^2\sigma^2) \right], \quad (1)$$

keeping only the leading two terms in the GRA [Eq. (10) in Ref. 9]. Here λ is the wavelength, n is the refractive index of the background media, m is the relative refractive index of the particle, $\mu = \langle l \rangle$ is the mean light path through the scatterer, and σ is given by $\sigma^2 = \langle l^2 \rangle - \langle l \rangle^2$. The first term on the right-hand side of Eq. (1) is the scattering cross section in the intermediate case limit.^{11,12} The second term is a correction introduced by the GRA when the condition $(2\pi r/\lambda)|m-1| < 1$ is not met. In the absence of absorption, optical extinction K is given by

$$K = C_s NL = \pi r^2 \left(\frac{4n^2\pi^2}{\lambda^2} \alpha r^2 - \frac{16n^4\pi^4}{\lambda^4} \frac{\beta r^4}{12} \right) NL, \quad (2)$$

where N is the concentration and L is the path length. For uniform spheres, α and β are given by

$$\alpha \approx 2(m-1)^2, \quad \beta \approx \frac{460}{81}(m-1)^4. \quad (3)$$

For soft particles with a size smaller than or comparable with λ the first term in Eq. (2) is sufficient to describe K , which is linear in λ^{-2} . For particles with a larger size or refractive index the second term in Eq. (2) must be included to accurately describe K .

In the experiment *B. subtilis* ESs (strain NCTC 3610) were isolated from their cellular debris,¹³ heat activated,¹⁴ and placed in a germination medium.¹⁵ The germination medium had a minimal carbon source and limited amino acid content to restrict cell growth and prevent reversal of activation.

Transmission was measured from 400 to 1000 nm, a region in which the bacteria have little absorption, and losses are due to scattering. The concentration was 1.03×10^8 ESs/ml in a 1-cm quartz cuvette. The

transmission spectra were measured with a halogen light source (HL2000, Ocean Optics, Dunedin, Florida) and compact spectrometer (HR2000, Ocean Optics), both coupled to optical fibers. The spectra were acquired at 1-min intervals for the first 3.5 h after heat shock and at 30-min intervals between 3.5 and 20 h. Each spectra was integrated for 5 s.

A least-squares fit to a function of the form

$$K = C_2\lambda^{-2} + C_4\lambda^{-4} \quad (4)$$

was applied to each transmission spectrum. Figure 1 shows K plotted as a function of λ^{-2} before heat shock and at representative times after heat shock: $t=1, 30, 60, 120$, and 360 min. The respective least-squares fits are also plotted in Fig. 1. Coefficients C_2 and C_4 are plotted at all time intervals in Fig. 2. As seen in Fig. 1, the spectrum from the spores immediately after heat shock is nearly identical to that of the spores before heat shock, indicating that the response of the spores to heating is not instantaneous. It can also be observed in Figs. 1 and 2 that the largest reduction in scattering occurs in the first 2 h, primarily caused by a dramatic decrease in the refractive index as the ESs shed their coat and hydrate the core. From 2 to 3 h the rate of reduction in refractive index slowed while the radius continued to increase. The scattering cross section remained relatively constant from 3 to 8 h, indicating that the refractive index and spore size were not changing significantly. After 8 h, K decreased slowly as the ESs decayed, releasing their contents into solution.

With a uniform spherical model for the ESs, which neglected the contribution of the coat, the radius and index were calculated from C_2 and C_4 with Eq. (2) and expressions (3). It was observed that the radius (plotted in Fig. 3) remained relatively constant in the first 30 min after heat shock. The ES radius was also calculated with only C_2 and making the assumption that the refractive index was equal to that of vegetative cells, 1.39 (Refs. 3 and 16; also plotted in Fig. 3). The radius, calculated by both methods is in agreement with $t > 3$ h, confirming that by 3 h the ESs have lost their coat and the index is close to that of vegetative cells. For $t < 3$ h the radius calculated by

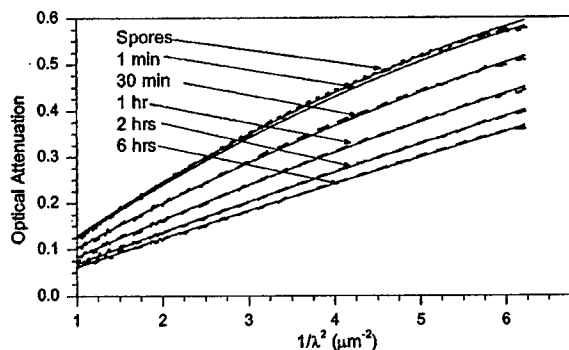


Fig. 1. Light extinction as a function of wavelength plotted for spores before heat shock and at $t=1$ min, 30 min, 1 h, 2 h, and 6 h after heat shock (dashed curves). The least-squares fit to $K=C_2\lambda^{-2}+C_4\lambda^{-4}$ is shown for each spectrum (solid curves).

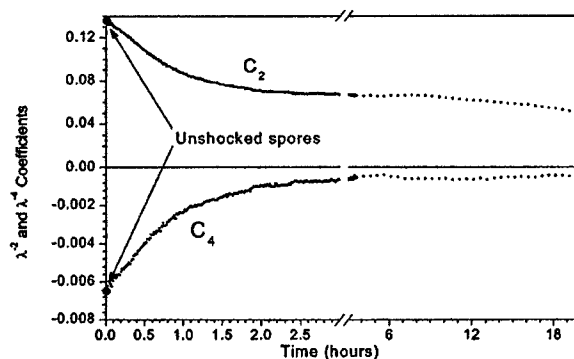


Fig. 2. Least-squares fit coefficients C_2 and C_4 plotted as a function of time.

use of a fixed index of 1.39 is substantially larger than the radius calculated from C_2 and C_4 and incorrectly predicts that the radius is decreasing over time. This lack of agreement demonstrates that the ES refractive index during the early time period is greater than 1.39. The ES radius, calculated from C_2 and C_4 , is $0.35 \mu\text{m}$ for the unshocked spores and $0.34 \mu\text{m}$ at 1 min after heat shock. The radius gradually increases to a maximum of $\sim 0.6 \mu\text{m}$ after 6 h. In a nutrient-rich medium the ESs would continue to germinate and grow, eventually reaching the size of vegetative cells. The refraction index, calculated from Eq. (2) and expressions (3) and plotted in Fig. 4, is 1.55 for both the unshocked spores and at 1 min after heat shock. The index decreases steadily in the first 3 h, after which it remains constant at 1.39, showing that by this time the core has hydrated and become closer to vegetative cells in density and composition.

A better model for the spore structure that takes into account the spore coat is two concentric nonabsorbing spheres consisting of a thin outer shell—the spore coat—that slowly dissolves and an inner sphere—the spore core—that changes in index and size. The ratio of spore coat thickness to cell radius is designated ϵ . The initial spore coat thickness is taken to be 70 nm ,¹⁷ and, for an approximate initial radius of 400 nm , ϵ is initially set to 0.175. Since the calculated spore radius (see Fig. 3) was unchanged during the first 30 min, our model assumes that the spore coat also remains unchanged during this time. This model assumes that from $t=0.5$ to $t=3$ h the coat thickness uniformly decreases from its initial value to zero. Microscopy confirmed that the spore coat completely dissolved within 3 h of heat shock.

In the GRA for concentric spheres the geometric ray inside the particle may bisect both the core and the coat, with relative refractive indices m_i and m_o , respectively. The modified geometric path, $l'=l_i(m_i-1)+l_o(m_o-1)$, is given by

$$l' = 2(m_o - 1)(r_o^2 - h^2)^{1/2} + 2(m_i - m_o)(r_i^2 - h^2)^{1/2}, \quad h < r_i$$

$$= 2(m_o - 1)(r_o^2 - h^2)^{1/2}, \quad h > r_i, \quad (5)$$

with the distribution function for h given by $p(h) = (2h/r_o^2)$ and normalized to unity. Evaluating $\langle l' \rangle$ and

$\langle I^2 \rangle$ with Eq. (5) and keeping only the first-order terms in ε allows α and β to be approximated by

$$\alpha \approx 2(m_i - 1)^2 - 8(m_i - 1)(m_i - m_o)\varepsilon + \dots,$$

$$\beta \approx \frac{460}{81}(m_i - 1)^4 - \frac{544}{27}(m_i - m_o)[(m_i - 1)^3 - 2(m_i - m_o)^3]\varepsilon + \dots, \quad (6)$$

where m_o is taken to be 1.39. The radii and refractive indices were recalculated with this model and are also plotted in Figs. 3 and 4, respectively. The recalculated spore radius is $0.37 \mu\text{m}$ before heat shock. For the first 30 min after heat shock the radius remains essentially unchanged at $0.38 \mu\text{m}$ and then slowly increases. The refractive index is 1.515 for the unshocked spores, which is in agreement with the value of 1.52 reported by Tuminello *et al.*⁴ After heat shock the index drops linearly to 1.39 over a 2-h period.

Confocal microscopy finds an ellipsoidal shape for the ESs before heat shock with a long axis of $1.25 \mu\text{m}$ and short axes of $0.75 \mu\text{m}$, equivalent in light extinction to a sphere of radius $0.43 \mu\text{m}$, which is in agreement with our concentric sphere model.

In conclusion, the GRA has been used to measure refractive-index and size changes in ESs during heat-shock activation from light-extinction measurements. Within 2 h of the start of activation the refractive index decreased from 1.51 to 1.39. The radius began to increase after the first half hour from 0.38 to $0.6 \mu\text{m}$ at 4 h. This work demonstrates that light extinction can monitor *in situ* both the refractive index and the size of ESs, may potentially be part of an optical bi-agent detection scheme, and can be used for modeling applications.

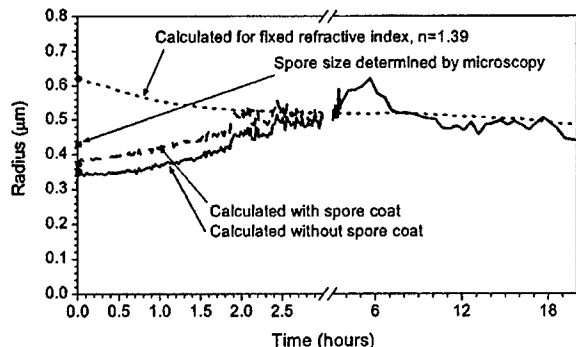


Fig. 3. ES radius plotted as a function of time after heat shock. The radius was calculated by three methods: (1) from C_2 and C_4 assuming a uniform sphere (i.e., without a spore coat), (2) a uniform sphere with $n=1.39$, and (3) two concentric spheres with the outer sphere (spore coat) dissolving as described in the text.

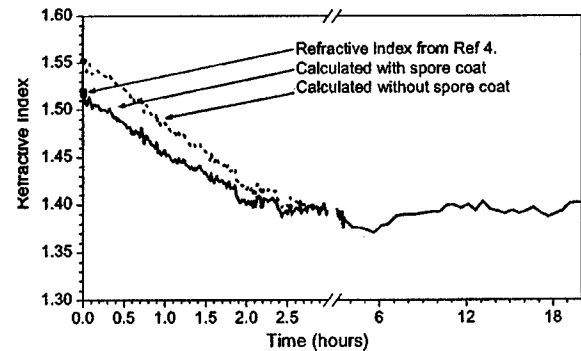


Fig. 4. ES refractive index calculated for uniform spheres (no coat) and two concentric spheres with the outer sphere (spore coat) dissolving as described in the text.

This work was supported in part by a NASA University Research Center; the New York State Office of Science, Technology and Academic Research; Northrop Grumman Corp; the Charles E. Culpepper Biomedical Pilot Initiative Grant; and the U.S. Department of the Army (grant DAMD17-02-1-0516). A. Katz's e-mail address is akatz@ccny.cuny.edu.

References

1. A. L. Koch and E. Ehrenfeld, *Biochim. Biophys. Acta* **165**, 262 (1968).
2. P. J. Wyatt, *Nature* **221**, 1257 (1969).
3. A. Katz, A. Alimova, M. Xu, E. Rudolph, M. Shah, H. E. Savage, R. Rosen, S. A. McCormick, and R. R. Alfano, *IEEE J. Sel. Top. Quantum Electron.* **9**, 277 (2003).
4. P. S. Tuminello, E. T. Arakawa, B. N. Khare, J. M. Wrobel, M. R. Querry, and M. E. Milham, *Appl. Opt.* **36**, 2818 (1997).
5. S. E. Harding and P. Johnson, *Biochem. J.* **220**, 117 (1984).
6. A. D. Molina-Garcia, S. E. Harding, L. de Pieri, N. Jan, and W. M. Wailes, *Biochem. J.* **263**, 883 (1989).
7. A. Katz, A. Alimova, M. Xu, H. E. Savage, M. Shah, R. B. Rosen, and R. R. Alfano, *Proc. SPIE* **4965**, 73 (2003).
8. A. Alimova, A. Katz, H. E. Savage, M. Shah, G. Minko, D. V. Will, R. B. Rosen, S. A. McCormick, and R. R. Alfano, *Appl. Opt.* **42**, 4080 (2003).
9. M. Xu, M. Lax, and R. R. Alfano, *Opt. Lett.* **28**, 179 (2003).
10. M. Xu, *Appl. Opt.* **42**, 6710 (2003).
11. P. Chylek and J. Li, *Opt. Commun.* **117**, 389 (1995).
12. H. C. van de Hulst, *Light Scattering by Small Particles* (Dover, New York, 1981).
13. D. Dubnau, *Methods Enzymol.* **21**, 430 (1971).
14. S. J. Foster and K. Johnstone, in *Regulation of Prokaryotic Development. Structural and Functional Analysis of Bacterial Sporulation and Germination*, I. Smith, R. A. Slepecky, and P. Setlow, eds. (American Society for Microbiology, Washington, D.C., 1989), p. 89.
15. B. Setlow, E. Melly, and P. Setlow, *J. Bacteriol.* **183**, 4894 (2001).
16. M. Jonasz, G. Fournier, and D. Stramski, *Appl. Opt.* **36**, 4214 (1997).
17. A. Driks, *Microbiol. Mol. Biol. Rev.* **63**, 1 (1999).

Fractal Mechanisms of light scattering in biological tissue and cells

M. Xu and R. R. Alfano

Institute for Ultrafast Spectroscopy and Lasers,

New York State Center of Advanced Technology for Photonic Applications,

and Department of Physics,

The City College and Graduate Center of City University of New York,

*New York, NY 10031**

We use fractal continuous random media to model visible and near infrared light scattering by biological tissue and cell suspensions. The power law of the reduced scattering coefficient, the anisotropy factor of scattering, and the phase function are derived. The fractal fluctuation of the dielectric permittivity, dependent on the fractal dimension D_f and the cutoff correlation length l_{\max} , is shown to determine the characteristics of light scattering. Good agreement with experimental results are reported. Implications on spectroscopic tissue diagnosis are discussed.

© 2005 Optical Society of America

OCIS codes: 170.3660, 170.4580, 170.6510, 170.1530, 290.0290

*Electronic address: minxu@sci.ccny.cuny.edu

The interaction of light with tissue and cells is the underlying mechanism for optical biomedical technology used in optical imaging and spectroscopy for detection of pathology changes. The optical properties of tissue are determined by chromophores, microstructures and local refractive index variations. Microstructures in biological tissue range from organelles $0.2\text{--}0.5\mu\text{m}$ or smaller, mitochondria $1\text{--}4\mu\text{m}$ in length and $0.3\text{--}0.7\mu\text{m}$ in diameter, nuclei $3\text{--}10\mu\text{m}$ in diameter, to mammalian cells $10\text{--}30\mu\text{m}$ in diameter. The refractive index variation is about $0.04\text{--}0.10$ for biological tissue with a background refractive index $n_0 = 1.35$.¹ Recently, the nature of light scattering in biological tissue has been actively studied.¹⁻⁶ As many biological tissues have fractal-like organization and are statistically self-similar,^{2,7-9} a discrete particle model of scattering centers in tissue^{1,4} was proposed to model light scattering by tissue. The discrete particle model assumes that the refractive-index variations caused by underlying microscopic structures can be treated as spherical particles with sizes distributed according to a powerlaw:

$$\eta(a) = \eta_0 a^{3-D_f} \quad (1)$$

where $\eta(a)$ is the volume fraction of spherical particles of radius $0 \leq a \leq a_{\text{max}}$ with a maximum radius a_{max} , η_0 is a constant, and D_f is the fractal dimension. On a microscopic scale the constituents of tissue have no clear boundaries and merge into a quasi-continuum structure. Discrete particles may not be appropriate to describe tissue inhomogeneities. As the refractive index variation in biological tissue is weak, tissue is better modeled as continuous random media where light scattering is not due to the discontinuities in refractive index but rather weak random fluctuations of the dielectric permittivity.⁵

In this Letter, we propose to use fractal continuous random media to model light scattering by biological tissue and cells. The correlation function $R(r)$ of the random fluctuations of the dielectric permittivity depends on the fractal dimension D_f and the cutoff correlation length l_{max} . Analytical expressions are derived for the power law of the reduced scattering coefficient, the

anisotropy factor of scattering, and the phase function. By examining the existing experimental results, the fractal fluctuation of the dielectric permittivity is shown to determine visible and near infrared light scattering by biological tissue and cell suspensions. The connection of the proposed model to the discrete particle model and implications on spectroscopic tissue diagnosis will also be discussed.

Assuming tissue is statistically space homogeneous and isotropic, the correlation function of the dielectric permittivity can be written as $R(r) = \langle \delta\epsilon(\mathbf{r}')\delta\epsilon(\mathbf{r}' + \mathbf{r}) \rangle$ where $\delta\epsilon$ is the fluctuation of the dielectric permittivity from the background value. $R(r)$ is proportional to the correlation function of the fluctuation of the refractive index $R_n(r)$ and $\delta\epsilon(r) = 2n_0^2(m - 1)$ where m is the relative refractive index at position r when the fluctuation of the refractive index is weak. Light scattering by the continuous random medium is determined by the power spectrum \hat{R} of the random fluctuations of the dielectric permittivity. The amplitude scattering matrix¹⁰ of the weakly fluctuating continuous random medium at the scattering angle θ is given by

$$S(\theta) \begin{pmatrix} \cos \theta & 0 \\ 0 & 1 \end{pmatrix} = k^3 \sqrt{\frac{\pi}{2} \hat{R}(2k \sin \frac{\theta}{2})} \begin{pmatrix} \cos \theta & 0 \\ 0 & 1 \end{pmatrix} \quad (2)$$

where $k \equiv 2\pi n_0/\lambda$ is the wave number and λ is the wavelength of light in vacuum. A simple exponential correlation function was considered by Moscoso et. al.⁵ for modeling tissue light scattering. It, however, did not describe essential features of light scattering by tissue such as the power law of the reduced scattering coefficient.

The correlation function of the random fluctuations of the dielectric permittivity, in the fractal continuous medium model, is assumed to be an average of exponential functions weighted by a power law distribution Eq. (1) for the correlation length l :

$$R(r) = \epsilon^2 \int_0^{l_{\max}} \exp(-\frac{r}{l}) \eta(l) dl = \epsilon^2 \eta_0 l_{\max}^{4-D_f} E_{5-D_f}(\frac{r}{l_{\max}}), \quad (3)$$

where $\varepsilon^2 = 4n_0^4(m-1)^2$, l_{\max} is the cutoff correlation length, and $E_n(z) \equiv \int_0^1 \exp(-z/t) t^{n-2} dt$.

The correlation function at the origin is $R(0) = \varepsilon^2 T_v$ where T_v is the total volume fraction of scattering centers ($T_v \simeq 0.3$ in soft tissue). The correlation function decays exponentially as $R(r) = \varepsilon^2 \eta_0 l_{\max}^{4-D_f} \left(\frac{r}{l_{\max}}\right)^{-1} \exp\left(-\frac{r}{l_{\max}}\right)$ at a large separation $r \gg l_{\max}$. The power spectrum is given by

$$\begin{aligned} \hat{R}(k) &= \int_0^{l_{\max}} \frac{\varepsilon^2 l^3}{\pi^2 (1 + k^2 l^2)^2} \eta(l) dl \\ &= \frac{1}{7-D_f} \pi^{-2} \varepsilon^2 \eta_0 l_{\max}^{7-D_f} {}_2F_1\left(2, \frac{7-D_f}{2}, \frac{9-D_f}{2}, -k^2 l_{\max}^2\right) \end{aligned} \quad (4)$$

where ${}_2F_1$ is the Hypergeometric function.

The amplitude scattering function $S(\theta)$ in Eq. (2) can now be written as

$$|S(\theta)|^2 = k^6 \frac{\pi}{2} \hat{R}(2k \sin \frac{\theta}{2}) = \int_0^{l_{\max}} \frac{\varepsilon^2 k^6 l^3}{2\pi [1 + 2(1-\mu)k^2 l^2]^2} \eta(l) dl \quad (5)$$

where $\mu \equiv \cos \theta$. From Eq. (5), the anisotropy factor (mean cosine of the scattering angle) can be found:

$$g = \int d\Omega \frac{(1+\mu^2)\mu |S(\theta)|^2}{2k^2} / \int d\Omega \frac{(1+\mu^2) |S(\theta)|^2}{2k^2}. \quad (6)$$

The unnormalized phase function is given by:

$$\begin{aligned} p(\theta) &= \frac{(1+\mu^2) |S(\theta)|^2}{2k^2} \\ &\simeq \frac{\frac{5-D_f}{2} \pi}{\sin\left(\frac{5-D_f}{2} \pi\right)} \frac{1+\mu^2}{2} [2(1-\mu)]^{-\frac{7-D_f}{2}} \\ &\propto (1+\mu^2)(1-\mu)^{-\frac{7-D_f}{2}}. \end{aligned} \quad (7)$$

The reduced scattering coefficient, defined as $\mu_s(1-g)$, is given by

$$\begin{aligned} \mu'_s &= \int d\Omega \frac{(1+\mu^2)(1-\mu) |S(\theta)|^2}{2k^2} \\ &= \frac{1}{2} \varepsilon^2 \eta_0 k^{D_f-3} \int_0^{kl_{\max}} dx \left\{ \frac{1}{2} x^{2-D_f} \ln(4x^2 + 1) \right\} \end{aligned}$$

$$\begin{aligned}
& - \frac{3 + 8x^2}{16(1 + 4x^2)} x^{-2-D_f} \left[4x^2(2x^2 + 1) - (4x^2 + 1) \ln(4x^2 + 1) \right] \Bigg\} \\
& \simeq \varepsilon^2 \eta_0 \alpha \lambda^{3-D_f}
\end{aligned} \tag{8}$$

where

$$\alpha \equiv (2\pi n_0)^{D_f-3} \frac{(11 - 4D_f + D_f^2)}{(D_f + 1)(D_f - 1)(D_f - 3)} \frac{\frac{5-D_f}{2}\pi}{2^{5-D_f} \sin\left(\frac{5-D_f}{2}\pi\right)} \tag{9}$$

is a constant dependent only on D_f . We have assumed $kl_{\max} \gg 1$ in our derivations of Eqs. (7) and (8).

The values of g in the fractal continuous medium model versus the cutoff size parameter kl_{\max} for various D_f are displayed in Fig. 1(a). g is larger with the increase of l_{\max} and the decrease of D_f . Light scattering Eq. (5) can be regarded to be a weighted sum from components of different correlation lengths where the peak contribution occurs at $kl^* = kl_{\max}$ when $D_f < 4$ and kl^* may be different from kl_{\max} when $D_f > 4$. The value of kl^* when $D_f > 4$ is displayed in Fig. 1(b). The power law of μ'_s Eq. (8) is obtained thanks to the cutoff at large correlation lengths as g approaches unity for components of increasing correlation lengths. By fitting experimental wavelength dependence of μ'_s to Eq. (8), one can determine both the fractal dimension D_f and the parameter $\varepsilon^2 \eta_0$.

Comparisons of the fractal continuous medium model for biological tissue and cells to experimental results are in order. We first fit the theoretical power spectrum Eq. (4) to the power spectrum of index variations in mouse liver tissue reported by Schmitt et. al.² [see Fig. 2(a)]. The fitting is excellent and yields $l_{\max} = 2.3\mu\text{m}$ and $D_f = 4.0$ for mouse liver tissue. A single exponential correlation function⁵ will not fit. We do not know any results on the wavelength dependence of the reduced scattering coefficient for mouse liver tissue. The wavelength dependence of the reduced scattering coefficient of rat liver tissue was reported by Parsa et. al.¹¹ The reduced scattering coefficients within the range 600 to 1400nm are displayed in Fig. 2(b) and fitted well to a power

law $\lambda^{-0.94}$. The fractal dimension of rat liver tissue is hence $D_f = 3.94$. The cutoff correlation length is found to be $l_{\max} = 1.5\mu\text{m}$ from $g = 0.94$ of the rat liver tissue at 800nm. Evidently, both the fractal dimension and the cutoff correlation length extracted from the power spectrum of the refractive index variations of mouse liver tissue agree reasonably well with those extracted from the light scattering data for rat liver tissue. This gives a strong support to the fractal continuous medium model for light scattering by tissue.

Fig. (3) displays the phase function for suspensions of rat embryo fibroblast cells (M1) and mitochondria, respectively, reported by Mourant et. al.³ and the fitting to the theoretical phase function (7). The fractal dimension is found to be $D_f = 3.86$ and 4.58 for M1 cells and mitochondria, respectively. The value of the fractal dimension for M1 cells was 4 ± 0.07 using the reported wavelength dependence $\mu'_s \propto \lambda^{-1.0 \pm 0.07}$ over the wavelength range 500 – 800nm. The agreement between the two values of D_f for M1 cells from fitting either the phase function or the powerlaw of μ'_s is good. The g -factor for M1 cells was reported to be 0.98 and the maximum correlation length can be estimated to be $l_{\max} \sim 3.2\mu\text{m}$. The g -factor for mitochondria can be computed from the phase function to be 0.81 and the maximum correlation length is then estimated to be $l_{\max} \sim 0.6\mu\text{m}$. The component contributing most to light scattering has size parameter $kl^* = kl_{\max} \simeq 40$ and $kl^* \simeq 1$ in M1 cells and mitochondria, respectively. M1 cells have much larger scattering centers and much smaller fractal dimension than mitochondria. The larger scattering centers in M1 cells are due to the nucleus.

These comparisons show that the fractal continuous medium model describes well light scattering from both biological tissue and cell suspensions. Cell suspension can be regarded as composition of many mini-continuous media of random fluctuating dielectric permittivity due to individual cells. The powerlaw of the reduced scattering coefficient originates from the underlying fractal fluctuation of the refractive index of the medium.

Light scattering in the fractal continuous medium model is caused by weak random fluctuations of the dielectric permittivity. This model, however, bears a close connection with the discrete particle model. We can approximate the amplitude scattering matrix of the spherical particles in the discrete particle model by¹²

$$|S(\theta)|^2 = \frac{2|m-1|^2 x^6}{[1 + 2(1 - \cos \theta)x^2]^2} \quad (10)$$

where $x \equiv ka$ is the size parameter of the particle as the particles are soft ($|m-1| \ll 1$). Ignoring the effect due to correlated scattering based on the fact that correlated scattering among particles of size much less than a wavelength is most significant while their contribution to scattering is minimal¹³, the discrete particle model assuming a particle size distribution of the powerlaw (1) reaches the same amplitude scattering function (5) as in the fractal continuous medium model. This illustrates the correlation length l in the fractal continuous medium model may be intuitively linked to the radius of “fictional” scattering centers present within tissue.

The power in the powerlaw of $\mu'_s \propto \lambda^{-b}$ is usually called the scattering power. The scattering power in the fractal continuous medium model relates to the fractal dimension of the underlying fluctuation of the refractive index ($b = D_f - 3$) and should be distinguished from that due to Mie particles of narrow size distribution.³ The scattering power has been recognized to be an important parameter in discriminating normal and cancerous tissue.¹⁴⁻¹⁶ Both the fractal dimension D_f and the parameter $\varepsilon^2 \eta_0$ can be estimated from fitting the wavelength dependence of μ'_s to Eq. (8) in the fractal continuous medium model. The value of D_f reveals the relative weight of small scattering centers vs large scattering centers. The value of $\varepsilon^2 \eta_0$ represents the overall density of scattering centers which is proportional to the radiographic density of tissue of predictive value for cancer risk.¹⁷ The maximum correlation length l_{\max} can be estimated from the anisotropy factor. The access to all these parameters will yield much more valuable information about the structure and the physiological state of tissue than using the scattering power alone.

In conclusion, we have shown that light scattering properties of biological tissue and cell suspensions can be well represented by a fractal continuous random medium model where light scattering is due to weak random fluctuations of the dielectric permittivity. The fractal dimension D_f and the cutoff correlation length l_{\max} characterizes the essential features of light scattering by biological tissue and cell suspensions, including the wavelength dependence of the reduced scattering coefficient, the phase function, and the anisotropy factor. The fractal continuous random medium model should facilitate the analysis of light scattering spectroscopy for tissue diagnosis and provide valuable insight to light scattering mechanisms by tissue and cells.

This work is supported in part by NASA. M. X. thanks the support by the Department of Army (Grant# DAMD17-02-1-0516).

References

1. J. M. Schmitt and G. Kumar, Appl. Opt. **37**, 2788 (May 1998).
2. J. M. Schmitt and G. Kumar, Opt. Lett. **21**, 1310 (1996).
3. J. R. Mourant, J. P. Freyer, A. H. Hielscher, A. A. Eick, D. Shen and T. M. Johnson, Appl. Opt. **37**, 3586 (Jun. 1998).
4. R. K. Wang, J. Mod. Opt. **47**, 103 (2000).
5. M. Moscoso, J. B. Keller and G. Papanicolaou, J. Opt. Soc. Am. A **18**, 948 (Apr. 2001).
6. V. Backman, V. Gopal, M. Kalashnikov, K. Badizadegan, R. Gurjar, A. Wax, I. Georgakoudi, M. Mueller, C. W. Boone, R. R. Dasari and M. S. Feld, IEEE J. Selected Topics in Quantum Electron. **7**, 887 (2001).
7. Y. Gazit, D. A. Berk, M. Leunig, L. T. Baxter and R. K. Jain, Phys. Rev. Lett. **75**, 2428 (1995).
8. A. J. Einstein, H.-S. Wu and J. Gil, Phys. Rev. Lett. **80**, 397 (1998).
9. T. Vicsek, *Fluctuation and scaling in biology*, (Oxford University Press, New York) (2001).

10. H. C. van de Hulst, *Light scattering by small particles*, (Dover, New York) (1981).
11. P. Parsa, S. L. Jacques and N. S. Nishioka, *Appl. Opt.* **28**, 2325 (Jun. 1989).
12. V. S. Remizovich, *Sov. Phys. JETP* **60**, 290 (1984).
13. V. Twersky, *J. Opt. Soc. Am.* **65**, 524 (1975).
14. N. Ghosh, S. K. Mohanty, S. K. Majumder and P. K. Gupta, *Appl. Opt.* **40**, 176 (Jan. 2001).
15. A. E. Cerussi, A. J. Berger, F. Bevilacqua, N. Shah, D. Jakubowski, J. Butter, R. F. Holcombe and B. J. Tromberg, *Academic Radiology* **8**, 211 (2001).
16. A. Pifferi, J. Swartling, E. Chikoidze, A. Torricelli, P. Taroni, A. Bassi, S. Andersson-Engels and R. Cubeddu, *J. Biomed. Opt.* **9**, 1143 (2004).
17. K. Blyschak, M. Simick, R. Jong and L. Lilge, *Med. Phys.* **31**, 1398 (2004).

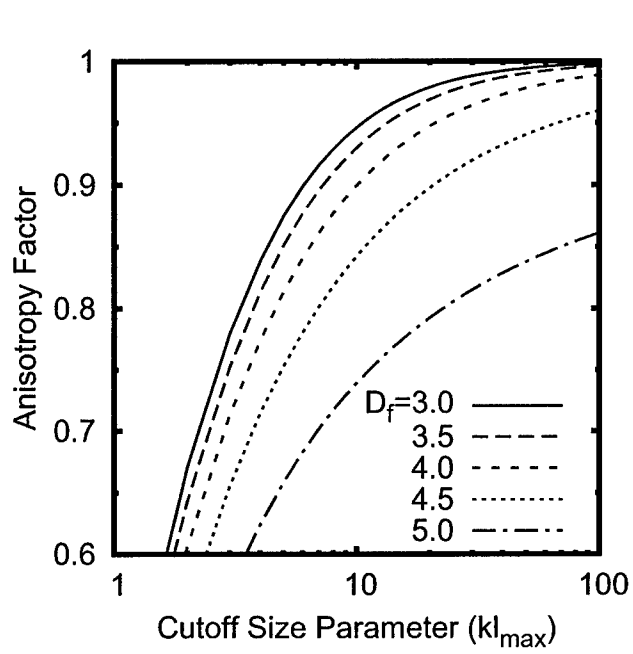
List of Figures

Fig. 1 (a) The anisotropy factor of the fractal continuous random medium versus the cutoff size parameter kl_{\max} . (b) Size parameter kl^* of the component contributing most to light scattering when $D_f > 4$.

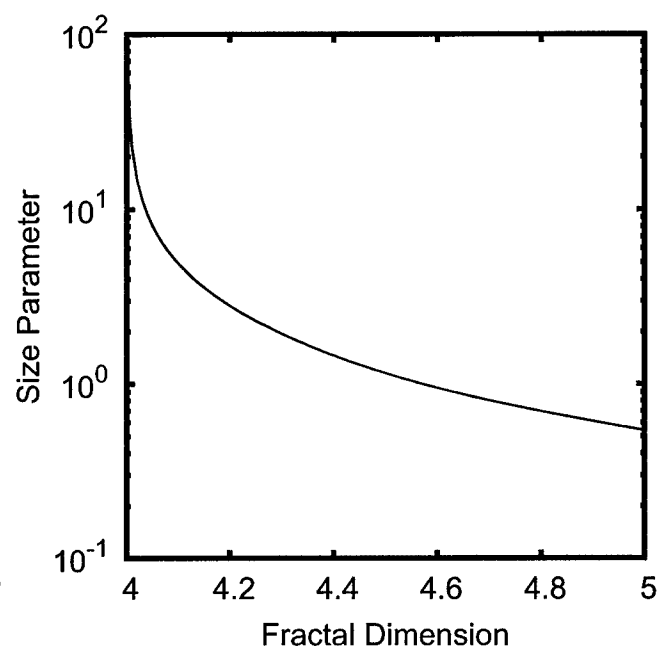
Fig. 2 (a) Power spectrum of refractive index variations in mouse liver tissue fitted to the theoretical power spectrum Eq. (4). Symbols represent data reported by² and the dash line is the theoretical fit. Fitting yields $D_f = 4.0$ and $l_{\max} = 2.3\mu\text{m}$. (b) The wavelength dependence of the reduced scattering coefficient of rat liver tissue fitted to the powerlaw λ^{3-D_f} . The symbols represent data reported by¹¹ and the solid line show the fitted curve. Fitting yields $D_f = 3.94$ and $l_{\max} = 1.5\mu\text{m}$.

Fig. 3 Phase function of suspensions of rat embryo fibroblast cells (M1) and mitochondria fitted to the theoretical phase function Eq. (7). Symbols are data reported by³ and the solid lines are theoretical curves. Fitting yields $D_f = 3.86$ and 4.58 for M1 cells and mitochondria respectively.

Figures



(a)



(b)

Fig. 1. M. Xu et. al.

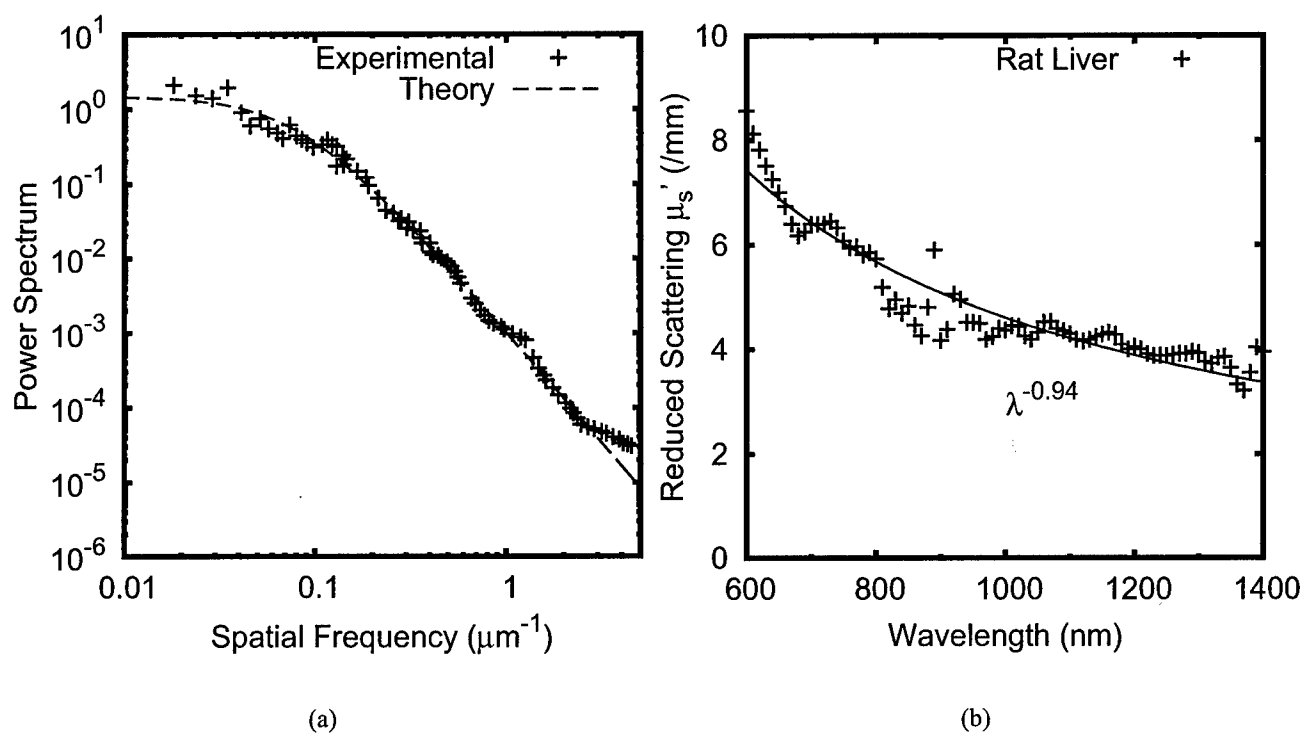


Fig. 2. M. Xu et. al.

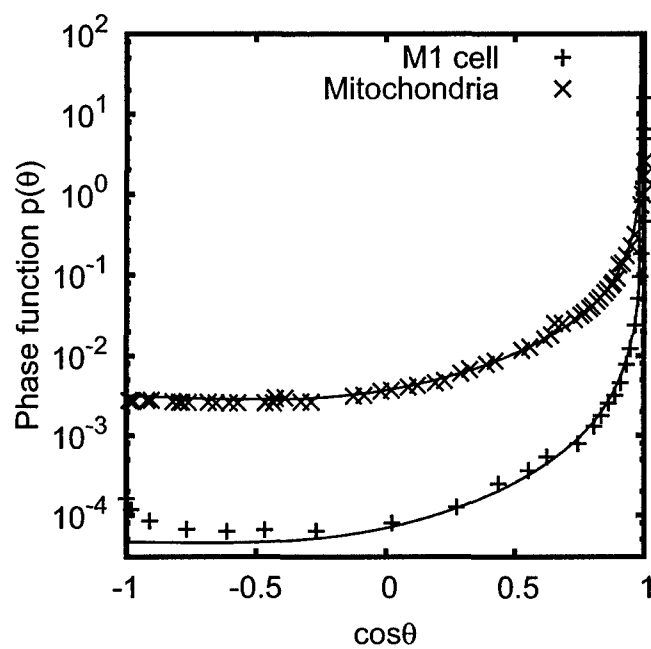


Fig. 3. M. Xu et. al.